Università degli studi di Napoli "Federico II"
Dipartimento di Ingegneria Chimica

Tesi di Dottorato in Ingegneria Chimica (XX Ciclo)

Diagnostic for the characterization of nanometric structures in high temperature reactive systems

2004-2007

Mario Commodo

Comitato Scientifico

Prof. Antonio D'Alessio - Relatore
Università degli studi di Napoli "Federico II" - Dipartimento di Ingegneria Chimica

Prof. Andrea D'Anna
Università degli studi di Napoli "Federico II" - Dipartimento di Ingegneria Chimica

Prof. Aldo Coghe
Politecnico di Milano – Dipartimento di Energetica

ABSTRACT

It is now well know that the fraction of particulate mater in the ambient air defined as ultrafine particles can be considered the most critical for adverse human health effects because of their chemical composition and the ability of these particles to penetrate deeply into the respiratory tract. Moreover combustion has been recognised as the major source of harmful fine and ultrafine particles.

The aim of the present thesis work is to investigate carbonaceous nanoparticles formation by combustion processes. An experimental procedure based on the use of the fifth harmonic of a Nd:YAG laser at 213 nm as exiting source and on an accurate signals acquisition has been realized. In-situ spectral optical measurements based on a combination of: Laser Induced Fluorescence (LIF), Laser Induced Incandescence (LII), Light Extinction (Kext) and Laser Light Scattering (Qvv) techniques have allowed to follow particles formation and their evolution directly in combustion environments with high spatial and temporal resolution. Laminar premixed and laminar and turbulent diffusion flames have been investigated burning ethylene, methane and benzene as fuels. Optical results are then compared with Particle Size Distribution Function (PSDF) obtained by Scanning Mobility Particles Sizer (SMPS) measurements in same flame conditions. An experimental investigation of the particulate emissions from commercial burners for home appliances fueled with natural gas has been also included.

The experimental evidences, in according to literature in laminar premixed conditions, allow to conclude that two classes of nanoparticles are formed in flame: Nanoparticles of Organic Carbon (NOC) with sizes smaller than three nanometers and "primary" soot particles with sizes larger than ten nanometers that lead to the formation of soot aggregates. Moreover, the thesis work shows that these combustion-generated nanoparticles strongly depend on the type of fuel, type of combustion system and eventual exhaust treatment systems.

CONTENTS

ABBREVIATIONS

LIF	Laser Induced Fluorescence
LII	Laser Induced Incandescence
NOC	Nanoparticle of Organic Carbon
PAH	Polycyclic Aromatic Hydrocarbon
PSDF	Particles size distributions function
SMPS	Scanning Mobility Particles Sizer
RSFR	Resonantly Stabilized Free Radical
HACA	Hydrogen-abstraction/acetylene-addiction mechanism
LLS	Laser Light Scattering
TEM	Transmission Electron Microscopy
DMA	Differential Mobility Analysis
AFM	Atomic Force Microscopy
SR	Sphericity Ratio
PM	Particulate Matter
HAB	Height Above the Burner
TPD	Thermocouple Particle Densitometry
DNS	Direct Numerical Simulations
RANS	Reynolds Averaged Navier–Stokes computations
LES	Large-Eddy Simulations
dp	Particle diameter
N	Number density of particles aggregates
np	The average number of primary particles per aggregate.
K_{abs}	Absorption coefficient
λ	Wavelength
Kn	Knudsen number
f	Euken factor
ΔH_v	Heat of vaporization
ρ_s	Density of soot in solid phase
ρ_v	Density of soot in vapor
Ts	Surface temperature of the particle
R	Universal gas constant
σ_{SB}	Stefan Boltzmann constant

ε	Soot emissivity
TR-LII	Time Resolved-Laser Induced Incandescence
LIE	Laser Induced Emission
PLIF	Planar Laser Induced Fluorescence
CCD	Charge-Coupled Device camera
S_F	Fluorescence signal
B	Einstein absorption coefficient divided by the speed of light
I_L	Laser spectral power density per unit area, divided by the laser bandwidth
Γ	Linewidth integral reflecting the overlap between laser and absorption line bandwidths
τ_L	Laser pulse length
N	(In page 45) The number of molecules in the ground electronic state
f_B	Boltzmann fraction, the portion of those molecules in the particular electronic-vibrational-rotational levels being excited by the laser
Φ	Fluorescent quantum efficiency
F_{fl}	Fraction of fluorescence collected within the detector bandwidth.
Ω	Solid angle
ϵ	(In page 45) transmission efficiency
η	Photoelectron efficiencies
Kext	Extinction coefficient
f_V	Particles volume fraction
S_{pp}	Scattered light
ΔV	Scattering volume
η_{opt}	Efficiency factor of the optical and electronic components comprising the detection system
K_{pp}	Energy scattered per unit time and per unit volume into a unit solid angle direction θ
τ_λ	Attenuation factor of the scattering when it travels between the scattering volume and the detector
Cpp	Scattering cross section
d_{63}	Average diameter of the particles
Zp	Particle electrical mobility
CPC	Condensation Particle Counter
FWHM	Full Width at Half Maximum

INTRODUCTION

In the last thirty years a great attention has been devoted to the understanding of the formation of by-products from combustion systems as result of the crescent world-wide interest to the reduction of pollutions and in parallel to the need of a more efficient utilization of fossil fuels. Many research groups, therefore, have intensified their efforts in the direction of a better understanding of the kinetic mechanisms of formation of Polycyclic Aromatic Hydrocarbons (PAH) and soot particles, analyzing the physical variables influencing such combustion by-products and developing techniques and experimental procedures able to detect and characterize chemically and physically these species.

Soot formation in combustion is a very complex problem that involves chemical and physical aspects, thousands of chemical reactions with hundreds of chemical species and various unsolved experimental problems.

On the other hand many progresses have been made in these years toward the understanding of the formation of the first aromatic ring (benzene), the growth to form heavy PAH, the inception of the first particle nuclei and finally to their growth and coagulation forming mature soot particles.

Moreover in the last years another class of particles has been found in combustion, both in sooting and non-sooting conditions: Nanoparticles of Organic Carbon (NOC) which have typical dimension of $2 - 3$ nanometers and intermediate properties between PAH molecules and soot particles.

In order to answer to the question about the relative importance of these particles class as soot precursors or as pollutions emitted from combustion processes many efforts have been done but the problem is not completely solved yet due to the wide range of variables involved. It is objective of many ongoing researches.

In both cases it is obvious to evidence the great interest and importance to follow and characterized the evolution of these two classes of particles.

Therefore, the subject of the present PhD thesis is the study of these two classes of combustion generated particles and the development of diagnostic tools able to measure and characterizer both NOC and soot particles.

The thesis is structured in six mainly chapters and conclusions and references.

In the first part of the thesis are reported the state of the art and the relevant literature on the current understanding of the problem of soot formation in combustion. The main mechanisms of PAH and soot formation have been described. Particular attention has been put to describe the properties and differences of NOC with respect to soot. Finally the effects of atmospheric aerosols on air quality and human health are discussed.

In the second chapter the main objectives of the thesis are resumed followed by a description of the used laboratory combustion systems: laminar premixed flames, laminar diffusion flames and turbulent diffusion flames. Moreover most of time of the thesis work has been used to develop the optical diagnostics techniques, in this chapter, therefore, will be described the used optical and spectroscopic techniques: Laser Induced Incandescence (LII), Laser Induced Fluorescence (LIF), Light Extinction and Elastic Light Scattering. Particles size distributions functions (PSDF) by differential mobility analysis measurements in some flame conditions are also performed and compared with the optical results, therefore, a short paragraph to illustrate the Scanning Mobility Particles Sizer (SMPS) instrumentation is also included into the chapter. Moreover, there is not way to correctly and completely characterize a flame and comparing experimental results with modeling data without to know the temperature profile in the flame. Temperature measurements and their correction are, therefore, illustrated. In conclusion this section included the description of the different experimental set-up performed for the different measurements.

Chapters three, four and five report the results obtained for the three cited laboratory combustion systems respectively.

Two fuels are prevalently tested and compared during this thesis: Ethylene and Methane even if Benzene was also studied but only in laminar premixed conditions.

On the basis of the acquired information consequently and parallel the experimental study of these three laboratory combustion systems measurements have been also performed in real combustor for home heating. Details of burners configurations, experimental measurements, index of measured pollutions emissions are included in the chapter six.

Finally a list of conclusion, final remarks and possible ongoing and future works are compiled and reported in section seven.

CHAPTER 1

PARTICLES GENERATED BY COMBUSTION PROCESSES

Combustion processes used in transportations, home appliances and power generation are considered as major sources of airborne species involved in atmosphere pollution especially in those zones of the earth with high population and industrialization density.

If under ideal conditions, corresponding to the stoichiometric composition of the burned mixture, the combustion processes of hydrocarbons lead to the formation of carbon dioxide and water, in non ideal conditions, such as those encountered in practical combustion systems, other undesired species, such as PAH, organic carbon nanoparticles and soot, are formed and therefore emitted in relation to the combustion conditions.

The improvement of the combustion processes in terms of locally deviances from the ideality, present in all practical systems: diesel and gasoline engines, gas turbines, burners for domestic or industrial boilers, therefore, have enough importance on the reduction of combustion by-products that involves the efforts of all combustion community.

Moreover, it is obvious that the generation by combustion of these airborne species is a very complicated process that necessitates of detailed understanding of the chemical and physical processes responsible for their formation.

Based on the current understanding the conversion from hydrocarbon fuel molecules, generally containing only few carbons atoms to agglomerate of soot particles passes through several fundamental steps that can so resume as reported in a review article on chemical reaction pathways by Richter and Howard [1]:

- *Formation of molecular precursors of soot*: The formation of the first aromatic ring, benzene, and the growth process to form larger and larger PAH seems to involve both the contributions of C_2, C_3 or other small units, among which acetylene has received much attention. Moreover

the relative contribution of the different types of growth reactions seems to depend strongly on the fuel structure: aromatic or aliphatic.

- *Nucleation or inception of particles from heavy PAH molecules*: In this process mass is converted from molecular to particulate systems with the formation of large aromatic cluster or very small nascent organic carbon particles with molecular mass of approximately few thousands of atomic mass units and mean diameters of about $1 - 3$ nm.

- *Mass growth of particles by addition of gas phase molecules*: After the formation of the nascent molecular particles their mass is increased by addition of gas phase species such as acetylene and PAH molecules or radicals. These reactions probably need the presence of radical sites on the particles surface, particularly in cases of stable reactants such as acetylene or stable PAH. This process of course does not affect the number of particles but only their volume fraction.

- *Coagulation via reactive particle-particle collisions*: The other possibility of particle growth happens by coagulation via particles collision. This process significantly increases particles size and decreases particle number concentration without changing the total mass of particles present.

- *Carbonization of particulate material*: At higher residence times, in the post-oxidization zone of the flames, the polyaromatic material undergoes a dehydrogenation process and alignment of polyaromatic layers, converting the initially amorphous soot material to a progressively more graphitic carbon material.

- *Oxidation*: As effect of the oxidation reactions the mass of these carbonaceous species decrease through the formation of CO and CO_2. Oxidation can occurs simultaneously or subsequently to the formation step depending on the local flame conditions. Moreover the main oxidation reactants are OH, O and O_2, the largest contributor in general being OH under fuel-rich conditions and O_2 under fuel-lean conditions.

Under these fundamental steps variables such as: temperature, pressure and fuel composition have non negligible effects on both qualitative and quantitative aspects in terms of combustion generated aerosols.

1.1 POLYCYCLIC AROMATIC HYDROCARBONS FORMATION IN COMBUSTION

The key to understanding the process of PAH generation involves as start point the formation of the first aromatic ring. Significant advances have been made on this fundamental step in our knowledge of both the reactions sequences and the species involved.

Similar to the general scheme suggested by Homann and Wagner [2] and Crittenden and Long [3], Bockhorn et al. [4] in the 1983, suggested a reaction sequence beginning with diacetylene and C_2H forming a branched hydrocarbon radical followed by acetylene attack and ring closure leading to a phenylacetylene radical. This mechanism was supported by experimental results obtained studying flat premixed low pressure flames of propane, acetylene or benzene.

Some years later Frenklach and Warnatz [5] made a decisive step towards a quantitative understanding of benzene formation by comparing concentration profiles predicted with a detailed kinetic model against experimental profiles of Bockhorn et al. [4] measured in the low pressure sooting acetylene flame above mentioned. The determination of net rates allowed assessment of the contribution of different benzene formation pathways included in the model. Conclusions from net rate analysis are of course dependent on the kinetics parameters used, and subsequent revisions of poorly known rate constants may have a significant impact on the computed contributions of the affected reaction pathways. Frenklach and Warnatz included four pathways leading to the first aromatic ring, all of them based on the cyclization of unsaturated aliphatic radicals: $n-C_6H_5 \rightarrow$ phenyl; $i-C_8H_5 \rightarrow C_6H_4C_2H$; $n-C_8H_5 \rightarrow C_6H_4C_2H$; $n-C_6H_7 \rightarrow$ benzene + H.

Similar conclusions were reached by Colket [6] studying the pyrolysis of acetylene and vinylacetylene in a shock tube.

A systematic screening of benzene formation pathways followed by the determination of the corresponding rate constants was performed by Westmoreland et al. [7] based on the concept of

chemical activation and using a Quantum Rice–Ramsperger–Kassel (QRRK) approach. In this work aromatics were formed "directly" from the reactants without observable intermediates.

Westmoreland et al. [7] identified the reactions of n-C_4H_5 and n-C_4H_3 with C_2H_2 as major pathway for benzene formation.

In an experimental and modeling study Bastin et al. [8] tested the formation of the first aromatic ring in a sooting acetylene–O_2–Ar premixed low-pressure flame through the reactions C_4H_5 + $C_2H_2 \rightarrow$ benzene + H and C_4H_3 + $C_2H_2 \rightarrow$ phenyl. Model predictions were compared against experimental profiles of stable and radical species measured by molecular beam mass spectrometry. At least satisfactory results were obtained for benzene and the species involved in its formation.

The formation mechanism of the first aromatic ring in the fuel-rich premixed acetylene flames studied by Bastin et al. [8] was later re-examined by Miller and Melius [9]. Flame structures were obtained by mass spectrometry after microprobe sampling, optical measurements allowed the determination of CH, OH and hydrogen-atom concentration.

Based on their carefully tested kinetic model, Miller and Melius [9] evaluated different pathways leading to the formation of the first aromatic ring. From the comparison of different model predictions with the experimental benzene profile showed that the contributions of the reactions n-C_4H_3 + $C_2H_2 \leftrightarrow C_6H_5$ and n-C_4H_5 + $C_2H_2 \leftrightarrow C_6H_6$ + H are not sufficient to explain the formation of benzene, even in the case of an unrealistic increase of the corresponding rate constants by a factor of 10. The n-C_4H_3 and n-C_4H_5 species are thermodynamically less stable than the corresponding isomers and reactions allowing isomerization for both C_4H_3 and C_4H_5 are included in the model. The effect of possible uncertainties in the heats of formation affecting the equilibria was tested by increasing the ΔH_f^0 of i-C_4H_3 by about 10 kcal mol^{-1}, favorable for the relative concentration of n-C_4H_3. Only a slight, clearly insufficient, increase of benzene formation was observed. Therefore thermodynamic uncertainties seem unlikely to be the reason for the under-prediction of benzene. Miller and Melius [9] discuss also the work of Bastin et al.

[8] and point out that these authors did not distinguish between the isomers of C_4H_3 and C_4H_5 and therefore they would implicitly include the reactions i-C_4H_3 + C_2H_2 $\leftrightarrow$ C_6H_5 and i-C_4H_5 + C_2H_2 $\leftrightarrow$ C_6H_6 + H in their mechanism. Effectively, the inclusion of these two reactions leads to a predicted benzene concentration profile with a peak value and location close to the experimental profile measured by Bastin et al. [8]. Nevertheless, this agreement can be considered as artificial because, as discussed by Miller and Melius, i-C_4H_3 and i-C_4H_5 are stabilized by delocalization of the free electron and therefore form only very weak bonds with stable molecules such as acetylene. The necessity of rearrangements including hydrogen shifts seems to be consistent with cyclization of i-C_4H_3 and i-C_4H_5 addition complexes either not occurring or having much lower rate constants than do similar reactions involving n-C_4H_3 and n-C_4H_5 which have a free electron at a terminal carbon atom without the possibility of delocalization.

Miller and Melius [9] also comment on the Frenklach and Warnatz [5] modeling of the sooting low-pressure acetylene flame investigated by Bockhorn and co-workers [4]. They attribute the agreement between predicted and experimental benzene profile to the absence of suitable isomerization reactions between the C_4H_3 and C_4H_5 isomers and to the use of unreasonably high rate constants.

The overall conclusion from the structural and thermodynamic considerations of Miller and Melius [9] is that one or more additional pathways are necessary in order to explain the formation of the first aromatic ring. Miller and Melius [9] discuss in some detail the possible contribution of the reactions C_3H_3 + C_3H_3 $\leftrightarrow$ C_6H_5 + H and C_3H_3 $\leftrightarrow$ C_3H_2 + C_6H_5. The comparison of model predictions for C_3H_3 and C_3H_2 with experimental data shows very good agreement for C_3H_3 but a significant over-prediction for C_3H_2. Therefore, based on this finding, the authors conclude that the recombination of two C_3H_3 molecules represents a more attractive source of benzene in acetylene flames. Based on experimental results, Stein et al. [10] also concluded that only the C3 +C3 route correctly describes the onset of experimentally observed

benzene formation and that the maximum rate for this pathway in significantly greater than for the others.

Concluding two main mechanisms seems to lead to the formation of the first aromatic ring: $C_2 + C_4$ and $C_3 + C_3$. However, despite the high number of works a generally accepted consensus about the dominant benzene formation pathway does not seem to have been reached.

Miller and Melius also emphasized the potential importance of Resonantly Stabilized Free Radicals (RSFR) in forming aromatics and PAH in flames.

Other compounds, in fact, can have relevance as precursors in PAH formations without passing through benzene as intermediate.

The formation of naphthalene, a compound with two aromatic rings, via the reaction of two cyclopentadienyl radicals was firstly included by Dean [11] in a kinetic model describing the methane pyrolysis.

Subsequently, based on combined experimental and kinetic modeling studies of PAH formation in methane and ethylene flames, Marinov et al. [12] and Castaldi et al. [13] jointly concluded that acetylene addition processes cannot account for the PAH levels observed in experimental flames. As a result of this work, they also proposed that in aliphatic hydrocarbon flames, the larger aromatics originate from resonance stabilized cyclopentadienyl radicals.

On the other hand the identification of acetylene as key reactant of growth process leading to larger and larger PAH up to soot particles was firstly intuited by Jensen [14] in the 1974 and subsequently by Bockhorn et al. [4] and by Frenklach et al. [15] using a similar growth sequence namely: hydrogen-abstraction/acetylene-addiction (HACA) mechanism.

The early modeling work of Frenklach et al. [15] is the decisive step toward the use of detailed kinetic model as tools for the development of a realistic understanding of PAH and soot formation. Frenklach and co-workers extended and refined their picture of PAH and soot formation in the subsequent years.

In particular the results obtained by Wang and Frenklach [16] support the important hypothesis in PAH growth that reactions of multi-ring aromatic species are in principle similar to those of benzene and phenyl.

However, D'Anna and Violi [17] comparing numerical results against experimental data obtained in slightly sooting laminar premixed ethylene–oxygen flames concluded that HACA mechanism is not sufficient to explain the PAH concentrations observed experimentally. The kinetic model developed by D'Anna and Violi takes into account PAH containing up to three rings and three different sub-mechanisms are tested: (a) reactions involving H-abstraction/C_2H_2-addition to aromatic radicals; (b) the reaction of species containing five-membered rings leading to naphthalene and phenanthrene, i.e. the cyclopentadienyl pathway; and (c) by combination of benzyl and propargyl radicals. Comparison of the net formation rates showed a dominant role of the cyclopentadienyl and the propargyl pathways.

Figure 1.1 shows the fundamental steps of PAH formation as described above.
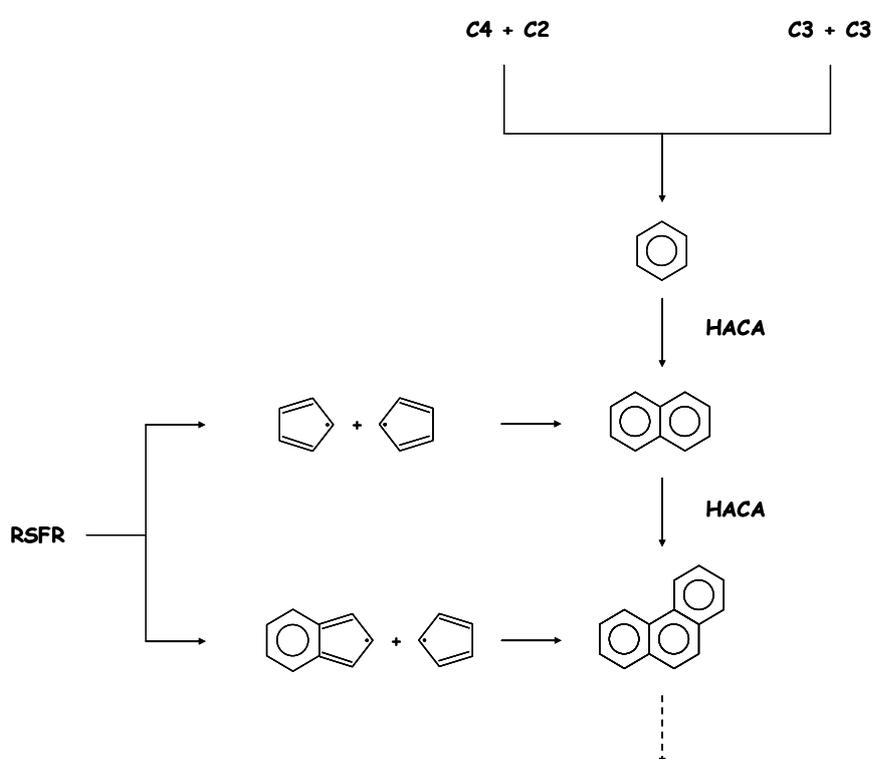
Fig. 1.1   Reaction pathways diagram of the fundamental steps in PAH formation.

1.2 NANOPARTICLES OF ORGANIC CARBON (NOC)

Particle inception, the transition from gas-phase compounds to nascent molecular particles, is probably the least understood step in the process of particulate formation at high temperature. It represents a dramatic change in the chemical and physical properties of the carbon-containing species which occurs in very short time-scales making the process difficult to follow. The number, the sizes and the chemical properties of the nascent particles strongly affect the amount and the size distribution of particulates emitted from combustion processes. Characterization of these molecular particles and of their transformation in different flame conditions is crucial to understanding the mechanism of particulate formation.

Nascent molecular particles were first detected by Howard et al. [18, 19] studying the early stages of soot formation in rich acetylene/oxygen flames at low pressure using molecular beam sampling followed by electron microscopy and mass spectrometric analysis of the ionized high molecular mass species. As result of these early work the authors showed that particles with mean size of 1.5 nm and about 2000 a.m.u. are formed in the soot inception region of the flame. Moreover experimental data showed also a concentration peak of these species just before the appearance of the first soot nuclei. Howard et al. [18, 19] concluded, therefore, attributing the role of soot precursors to these compounds.

Soot inception, the formation of nascent molecular particles in flame, has also been, extensively, studied by in-situ optical diagnostic from D'Alessio and co-workers mostly in the years between 1990 - 2000. Light extinction, Laser Light Scattering (LLS) and Laser Induced Fluorescence (LIF) have been showed as powerful techniques suitable for the characterization of the transition from the aromatic gas phase compounds to the formation of soot particles.

D'Alessio et al. [20], coupling in-situ optical techniques with direct sampling of hydrocarbons in lightly sooting and in sooting premixed ethylene/oxygen flames showed the formation in the flames of particles with typical average diameter approximately of 2 nm (2500 a.m.u), Nanoparticles of Organic Carbon (NOC), which do not absorb in the visible and fluoresce in the

18

ultraviolet could be considered soot precursors on the basis of their decreasing concentration profile in correspondence of soot inception. Authors also described soot inception process characterized by the progressive aromatization of these transparent particles, as shown by the progressive shift toward the visible of absorption and fluorescence. The internal rearrangement of a partially aromatic - polymeric structure, more than a progressive formation of very large PAH structures, was proposed as the mechanism of soot inception.

After this fundamental work D'Alessio and co-workers extended and refined their picture of soot inception defining this class of compounds, NOC, as a second class of combustion formed particles differently from soot not only in terms of average size but also in terms of chemical and physical properties.

D'Alessio et al. [21, 22], studying laminar premixed methane/oxygen flames across the soot threshold limit, individuated that NOC were detectable also in flames below the soot formation limit. It is obvious that this result has strong repercussions in terms of a new concept of pollutants from combustion systems. In others word the authors pointed out on the possible role of NOC, in same combustion configurations, as pollutants and not only as soot precursors.

However in a recent work, Thierley et al. [23] studying experimentally these nanometer-sized particles by photo-ionisation mass spectrometry and scanning mobility particle sizer (SMPS) in laminar premixed ethylene flames above and below the critical sooting threshold, concluded that neither method were able to detect an appreciable number of particles bellows the sooting threshold in flames similar to those studied earlier by D'Alessio and co-workers using ultraviolet light absorption and scattering measurements. This result was in particular suggest on the absence of particles coagulation decreasing the dilution ratio in the on-line sampling probe system in these flames conditions.

However the size – dependence of the nanoparticles coagulation efficiency [24] and the experimental uncertainties relative to the SMPS technique, in particular for this very small particles, does not allow to exclude that the origin of the ultraviolet absorption and fluorescence

in non-sooting flame conditions is probably due to these transparent high molecular mass compounds.

In addition, the experimental results obtained in the works of D'Alessio et al. [20 – 22] and in other further publications [25 – 27] suggested that there is an initial fast polymerization process building bricks of which are aromatic compounds with few condensed rings (no more than 2-3 rings). The authors concluded that soot inception is primarily controlled by the internal arrangement of these polymers of aromatics leading to structures with more condensed aromatic rings and more compact three dimensional shape thus forming the first soot nuclei.

The optical results obtained from D'Alessio and co-workers were in very good agreement with those obtained from Dobbins and Subramaniasivam [28] by particles thermophoretic sampling in diffusion flames, burning ethane, methane and acetylene. They found by electron microscopy analysis the presence of small polydisperse singlet particles which were more transparent than soot particles and with typical size around 3 nm. However a different chemical interpretation of these structures was given. Soot precursors were supposed in the work of Dobbins and Subramaniasivam [28] to be very large PAH while different was the interpretation of D'Alessio et al. [25] which, based on their optical data, concluded that these particles are composed by structures which have non more than two or three aromatic rings connected by aliphatic bonds.

Similar results was also obtained by Vander Wal [29] performing both optical (LIF and LII measurements) and TEM analysis in a normal and inverse diffusion flame. Both techniques revealed a so-called "dark region" between the PAH and soot-containing regions that the author attributed to nascent molecular particles.

All these results are, then, confirmed more recently by using Differential Mobility Analysis (DMA) [23, 30 - 32] and Atomic Force Microscopy (AFM) [24, 33].

Independently Sgrò et al. [30] and Zhao et al. [31] used DMA technique to measure the particles size distributions functions (PSDFs) in flames to follow the evolution of the particles formed in combustion. PSDF images showed that at low residence times just downstream the flames front

the first formed particles have a diameter of about 3 nm while at longer time the PSDFs became

bimodal with a first mode that remains unchanged and shows a pick at 3 nm and a second mode

characteristic of primary soot particles with mean diameter of about 10 − 20 nm.
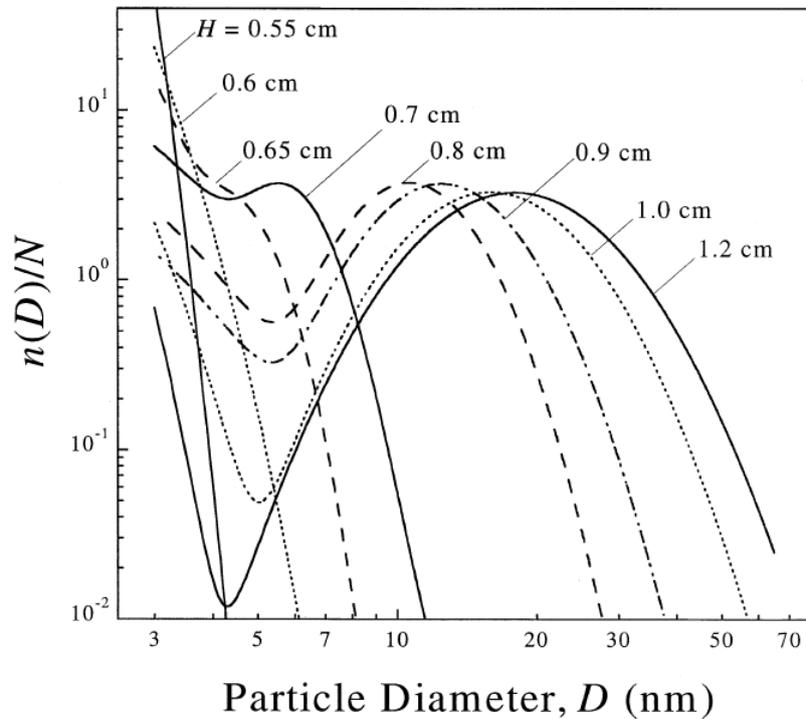
Fig. 1.2 PSDFs measured at different height above the burner in a laminar
premixed ethylene-argon-oxygen flame (Zhao et al. [31]).

Barone et al. [33], instead, measured PSDFs in flames using AFM technique. Particles were

collected on mica substrates by thermophoretic deposition and then analysed by AFM. The

results of Barone et al. [33] were in according with those obtained by Sgrò et al. [30] and Zhao et

al. [31] using DMA measurements on the presence of a bimodal PSDF indicative of the two cited

classis of combustion formed particles: NOC and soot.

Moreover, AFM measurements, as shown by Barone et al. [33] can also been used to obtain a

three dimensional topological characterization of the particles, fig. 1.3. The analysis of these

images produced the important result on the different Sphericity Ratio (SR=Particles

Height/Diameter) that characterize the two particles classes: 0.02 − 0.05 for NOC and 0.2 − 0.5

for soot particles.

C/O=0,56   C/O=0,77   C/O=0,92

Non - sooting   **Slight - sooting**   **Sooting**
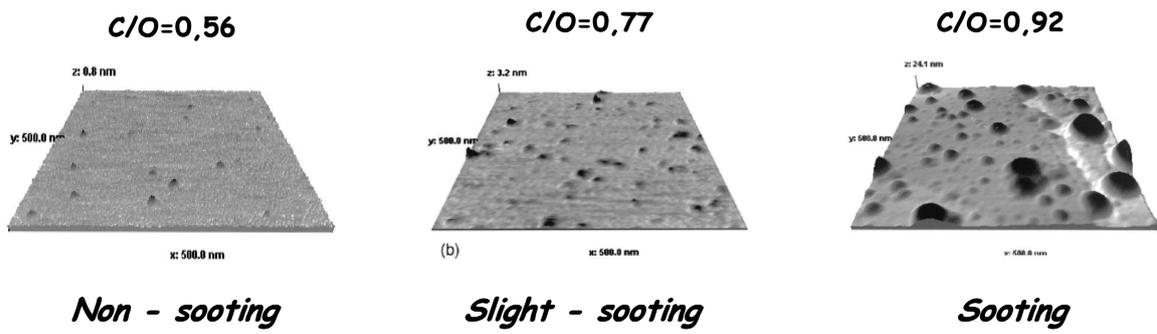
Fig. 1.3   3D AFM images for three different laminar premixed ethylene flames conditions from: Barone et al. [33].

1.3 SOOT FORMATION, GROWTH AND OXIDATION

As showed by Dobbins and Subramaniasivam [28] and by Vander Wal [29] by transmission electron microscopy analysis (TEM) of thermophoretic sampled material, soot is normally composed by aggregates of hundred or thousand of primary particles with mean size of 10 – 30 nm that form structures 0.1 μm up to10 μm. (Fig. 1.4)
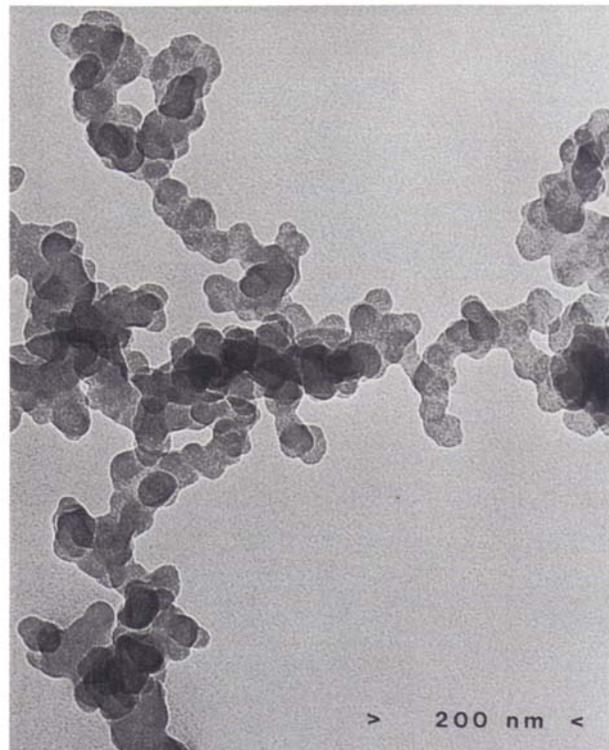
Fig. 1.4   TEM image of a typical soot aggregate by Dobbins and Subramaniasivam [28].

Theoretically, after the early numerical modeling work in PAH and soot formation based on the HACA mechanism, Frenklach and Wang extended and refined the model description of soot nucleation and growth applying it to laminar premixed acetylene and ethylene flames under different pressures [34] for which experimental data where available. The computational model used for the prediction of soot formation consisted of three logical parts: (I) initial PAH formation, which includes a detailed chemical description of fuel pyrolysis and oxidation, formation of the first aromatic ring, and its subsequent growth to a prescribed size; (II) planar

PAH growth, comprised of replicating-type growth of PAH beyond the prescribed size; and (III) spherical particle formation and growth of the resulting particles. In step (III), PAH formed in (II) may coagulate forming larger compounds which can grow by surface reactions. Nucleation describes the growth of planar PAH via the HACA sequence beginning with one-ring species and preceding up to an infinite size using the technique of chemical lumping. The aromatic Ai, containing i fused rings, formed in the nucleation process are then allowed to coagulate, that is, all the Ai collide with each other forming dimers; the dimers in turn, collide with Ai forming trimers or with other dimers forming tetramers; and so on. PAH beginning with the dimers were assumed to be soot particles and it was allowed to add and lose mass by surface reactions. The chemical mechanism adopted for this heterogeneous process is based on the H-abstraction/C2H2-addition reaction sequence and rate constants were estimated based on analogous gas phase reactions of one-ring aromatics: benzene and phenyl.

Differently from Frenklach and Wang, the PAH and soot formation in combustion was also described by D'Anna and Violi [17] coupled the HACA pathway with the use of resonantly stabilised free radicals (RSFR mechanism) as described above. D'Anna and Violi [17] obtained good agreement with experimental data in laminar premixed flames of both aliphatic and aromatic fuels. Moreover the kinetic scheme includes growth of species by fuel pyrolysis, particulate formation, growth, aggregation and oxidation. PAH formation includes reaction pathways leading to the formation of nanometric-sized particles and their coagulation to larger soot particles. A discrete-sectional approach [35] is used for the gas-to-particle process; the ensemble of compounds with molecular mass higher than the largest aromatic compound in the gas-phase is divided into classes of different molecular mass and all reactions are treated in the manner of gas phase chemistry using compound properties such as mass and the numbers of carbon and hydrogen atoms averaged within each section. Particle size distributions are obtained by solution of the transport equation for each section. A brief summary of the scheme is given here.

Gas Phase

The gas-phase formation and growth of aromatic compounds bridges the main oxidation chemistry and particulate formation. The gas-phase kinetic mechanism to model hydrocarbon oxidation and pyrolysis is built onto the GRI mechanism for C1 and C2 species and Miller and Melius suggestions for benzene formation [9]. The formation of naphthalene, the first compound in the PAH series, is modeled through two routes: the first, usually known as the HACA mechanism [34] is also used here to model the formation of multi-ring structures such as phenanthrene, pyrene and higher order PAHs up to coronene. The second is the combination of resonantly stabilized radicals. Two different reaction sequences are included for the formation of naphthalene: the combination of two cyclopentadienyl radicals and the combination of benzyl and propargyl radicals. The cyclopentadienyl and indenyl radical combination is also used for the modeling of phenanthrene.

Details of the reaction pathways and the choice of the reaction constant used are reported in previous papers [17] where the complete kinetic scheme for the gas-phase is listed. There are 70 species in the gas phase and about 380 gas-phase reactions.

Growth of aromatics and particle inception

Acetylene and aromatics, from benzene to coronene, are the building blocks for the growth process which lead to the formation of high-molecular-mass, molecular particles. The mechanism consists of the sequential addition of either acetylene or aromatic molecules to aromatic radicals. Classes of compounds termed sections, each covering a mass range are utilized. Sections are characterized by their average molecular mass and by their number of carbon and hydrogen atoms. The chemical reactions are treated in the same way as for gas phase chemistry. The aromatic growth and oxidation mechanism is schematized as follows:

$$Rx1 \quad A_i => R_i + H$$
$$Rx2 \quad A_i + H => R_i + H_2$$
$$Rx3 \quad A_i + OH => R_i + H_2O$$

$$Rx4 \quad R_i + H_2 => A_i + H$$
$$Rx5 \quad R_i + H_2O => A_i + OH$$
$$Rx6 \quad R_i + C_2H_2 => A_k + H$$
$$Rx7 \quad R_i + A_j => A_{i+j} + H$$
$$Rx8 \quad R_i + R_j => A_{i+j}$$
$$Rx9 \quad R_i + H => A_i$$
$$Rx10 \quad A_i + OH => A_k + HCO$$
$$Rx11 \quad R_i + O_2 => A_k + 2CO$$
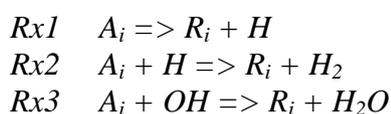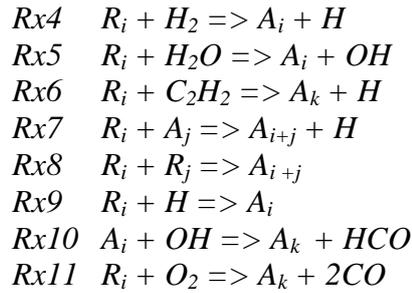
Here Ai is an aromatic compound having a molecular mass corresponding to the ith class of compounds and Ri is its radical. The rate constants are determined by using the Arrhenius formulation multiplied by a size dependent factor and a collision efficiency set to unity, except for the coagulation reactions [35].

Coagulation

The aromatics growth process can occur by formation of molecular clusters from collision of molecular compounds. The interaction energy is due to van der Waals forces. Small molecular mass aromatics may exhibit low interaction energy and as molecular mass increases interaction energy increases and the coagulation efficiency becomes more effective. The model of D'Alessio et al. [24], for premixed flame coagulation, is applied. For particles around 1 nm diameter the coagulation efficiency is about 1E–4 increasing to unity for particles around 10 nm diameter (Fig. 1.5).
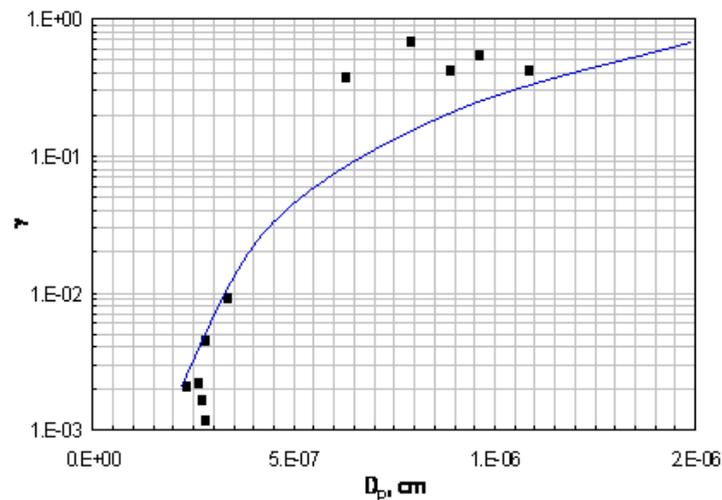
Fig. 1.4 Size depending coagulation efficiency [24].

In summary the complete scheme is made up of the gas-phase and particle phase schemes detailed previously [17-35] and added to the GRI mechanism [9].

There are 26 sections each containing the compound and its radical, starting with C12 and increasing by a constant factor of two. The diameter range is 1 nm – 200 nm. The largest sizes are to ensure that the series does not artificially truncate the solution. Reactions are balanced on carbon number; a sectional reaction generally results in two product classes proportioned to satisfy carbon element balance, but hydrogen element is not strictly balanced. The particle phase sectional combinations generate about 1850 reactions.

1.4 HUMAN HEALTH AND ENVIRONMENTAL ASPECTS

The increase of instrumental capability in measuring smaller and smaller particles has been accompanied to the revelation of new potential adverse human health and environments effects related to fine and ultrafine particles in ambient air.

Furthermore these compounds are prevalently generated by combustion sources and are typically characterized by a complex mixture of different particles type: elemental and organic carbon, metals, and inorganic compounds such as sulfates. On the other hand particles composition varied noticeably if different particles size ranges are taken in consideration. Sardar et al. [36] sampled for a period of 3 years size-fractionated ambient particulate matter with diameter below 10 μm (PM_{10}) founded that the ultrafine particle mode mostly consisted of organic carbon, with higher wintertime levels at the source sites due to increased organic vapour condensation from vehicles at lower temperatures. The organic carbon that dominates the ultrafine aerosols is comprised of primary aerosol that is emitted directly from combustion sources and of secondary aerosol that is produced by atmospheric processing of carbon compounds.

Adverse health effects of combustion-generated fine and ultrafine particles are well resumed in terms of current understanding and knowledge in recent papers by Kennedy [37], by Donaldson et al. [38] and by Oberdoster et al. [39]. The authors report a significant literature that demonstrates the link between exposure to these compounds in the atmosphere and adverse health effects. Fine and ultrafine particles, in fact, are able to penetrate much deeper into the lung. Therefore, when inhaled by people, the particles can be taken-up by cells in the lung and eventually penetrate into the circulatory system and lodge in organs such as the liver and heart.

Moreover nanoparticles generated during combustion constitute a cause of concern also for their direct or indirect, as cloud-condensation-nuclei, effects on radiative transfer in the atmosphere as showed by Jacobson [40] and by Novakov and Penner [41].

CHAPTER 2

COMBUSTION SYSTEMS AND EXPERIMENTAL TECHNIQUES

In this section a brief description of three combustion systems used and the fundamental of the physical principles to the base of the diagnostic techniques employed during the thesis will be given.

2.1 OBJECTIVES

The objectives of the PhD thesis are focused on the experimental characterization of total particulate produced from combustion processes. To this purpose in-situ optical diagnostics: laser induced fluorescence, laser induced incandescence, light extinction and elastic light scattering are extensively employed in numerous combustion configurations with the aim to produce a complete, qualitative and quantitative, description of the kinetic evolution of the particulate in combustion.

Moreover it is well know that the techniques normally used for particle measurements in flames can be divided into two categories: *ex-situ* and *in-situ*. To this purpose optical techniques are used for *in-situ* particle characterization (size and volume fraction). Their advantages over the *ex-situ* techniques include non-intrusion in the flame and real time analysis. However, the main drawback of the optical techniques is that they need to exactly know the refractive index of the particles to reproduce the data correctly [43].

Particular efforts in this thesis have been focused on particles inception, the formation of the first particles nuclei (NOC) and to follow their evolution in different flame conditions. The current state of the knowledge on these species, in fact, came from numerical and experimental works

using laminar premixed flames [17 – 27] while only a little number of data are available in more complex system like laminar diffusion flames [28, 42] and practically ones in turbulent diffusion flames, that moreover constitute systems more similar to real combustion appliances.

2.2 LABORATORY COMBUSTION REACTORS

2.2.1 LAMINAR PREMIXED FLAMES

In a laminar premixed flame fuel and oxidant are mixed before the flame front, where they react together. This system represents the easy combustion apparatus allowing to follow the combustion process, temperature and species concentration, as function of only one variable: the Height Above the Burner (HAB) or equally as function of the residence times in flame if the flame velocity profile is known.

During this thesis work some experiments were performed on atmospheric pressure laminar flat premixed flames using a commercial McKenna burner (6 cm diameter), with a stainless steel plate, located at a height of 25 mm above the burner. In the order: ethylene/air, methane/oxygen and benzene/air flames have been investigated mostly by optical techniques changing the C/O ratio, from the stoichiometric value up to sooting flame conditions, and for different heights above the burner, from the flame front up to the post-oxidation zone.

2.2.2 LAMINAR DIFFUSION FLAMES

In diffusion flames, often called non-premixed flames, fuel and oxygen meet to form a combustible mixture, and once ignition has taken place, burning starts immediately upon creation of such mixture. In this case, the flame appears at the border between the fuel and oxygen zones [44]. Combustion products created by the flame spread to both side, and fuel and oxygen have to diffuse against those streams in order to mix and react. It is common knowledge that this mechanism is on the basis of many, domestic and industrial, appliances or simply on the basis of a candle combustion.

For this reasons, laminar diffusion flames, have been the subject of many investigations. The configurations of major interest are three and are reported in figure 2.1.

Configuration (a) in Fig. 2.1 is characteristic of the most common studied diffusion flame, a normal co-flow laminar diffusion flame. In this case fuel flows through an internal tube while the oxidant passes through an external annular region with the aim to stabilize the fuel jet.

Using the same configuration but inverting the relative positions of fuel and oxygen we obtain an "inverse co-flow laminar diffusion flame", Fig. 2.1 (b). Soot and PAH form on the outside of the inverse diffusion flame in the fuel stream, so they do not pass through the high-temperature reaction zone [45]. Therefore, the study of inverse diffusion flames may yield information about soot inception and growth and the formation of soot precursors, such as PAH.
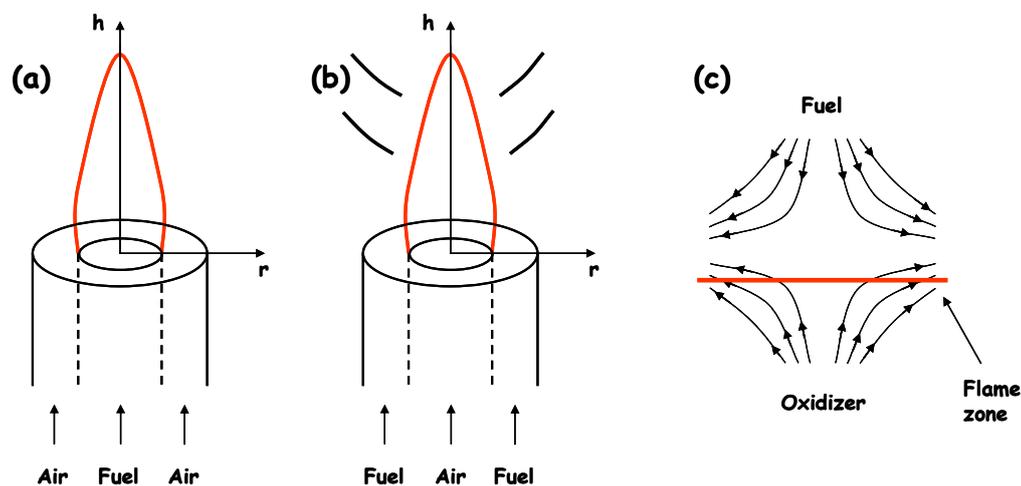
Fig. 2.1   Normal co-flow laminar diffusion flame (a), inverse co-flow laminar diffusion flame (b) and opposed or counter-flow diffusion flame (c).

The third case, Fig. 2.1 (c), is an opposed or counter-flow diffusion flame. The combustion in a similar configuration takes place in a single thin flame zone near the stagnation plane, and around the location of the stoichiometric mixture. Normally, either the fuel or the oxidizer reaches the flame by diffusion from the stagnation plane in a direction counter to the convective flow, and the products of the combustion are convected back towards the stagnation plane [44].

The counter-flow diffusion flame is suitable for most aspects of the investigation of diffusion flame reaction zone structure and properties and in particular for application in the flamelet model of turbulent combustion.

During the thesis an experimental investigation of combustion formed particles in laminar diffusion flames have been attempted for the configuration in fig. 2.1 (a): normal laminar co-flow diffusion flame.

The burner configuration is similar to that used by Santoro et al. [46] for the characterization of ethylene diffusion flames, in terms of soot formation using scattering and extinction measurements, by Shaddix and Smyth [47] and by McEnally et al. [48], for ethylene and methane laminar diffusion flames using, respectively, Laser Induced Incandescence (LII) and Thermocouple Particle Densitometry (TPD).

It consists of a 12 mm diameter uncooled vertical tube for the fuel and a concentric tube (108 mm i.d.) for air. The air-annulus is reduced at the burner lip by a ring (i.d. 55 mm) to stabilize the flame. This increased the air velocity by a factor of 4.8 but it affected only the flame height by a few millimetres. The fuel passage contains screens and 3 mm glass beads to provide a uniform exit flow profile. The air passage also utilizes a series of screens with a section filled with glass beads. Moreover the burner is mounted on a three-dimensional translation stage that allows to characterized the flames vertically and radially with a spatial resolution of 0.5 mm

2.2.3   TURBULENT DIFFUSION FLAMES

Turbulent diffusion flames, Fig. 2.2, are used for wide range of practical combustion systems, such as: gas turbine; diesel engines; oil-, gas-, and pulverized coal-fired boilers and furnaces.

Turbulent combustion processes in gaseous phase is a complex physical phenomena that strongly depends upon: chemistry, diffusion of heat and species, convective motions induced by the turbulent fluid, and thermodynamics.
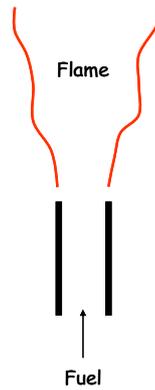
Fig. 2.2 Turbulent jet diffusion flame configuration.

Due to this complexity, many existing turbulent combustion models have been based on a simplified view of chemistry and diffusion processes.

The three main classes of numerical tools usually employed in combustion research [49]: Direct Numerical Simulations (DNS), Reynolds Averaged Navier–Stokes (RANS) computations and Large-Eddy Simulations (LES).

The DNS approach consists in solving exactly all the physical spatial and time-scales embedded in the representative flow equations, without any model for turbulence. This method generally requires prohibitive numerical costs.

RANS equations are restricted to a description of the mean flow field. Mean transport equations are obtained by averaging in time or over ensembles the instantaneous balance equations. This operation yields unclosed quantities, representative of the turbulent fluctuations, that must be modeled [49]. The RANS approach is presently the only one really suited for the simulation of practical configurations, but its accuracy is limited and it cannot be used in a predictive manner, but only to identify major trends.

Large Eddy Simulations can be seen as an intermediate between DNS and RANS. In LES, the largest structures of the flow field are explicitly computed like in DNS whereas the effects of

small-scale structures are modeled. LES simulations are thus, by construction, more expensive than RANS calculations, but faster than corresponding DNS. The balance equations for LES are obtained by filtering spatially the instantaneous balance equations.

LES are already widely used for non-reacting flow simulations but are still at an early stage for turbulent combustion. Note that, for all three numerical modeling approaches, a correct description of the behaviour of turbulence requires three-dimensional (3D) calculations, and therefore high computing times. This constraint can be released for RANS in the presence of statistically homogeneous directions. This ideal case is, however, not often found in industrial configurations.

Furthermore, all modelling works in turbulent jet diffusion flames need to be studied experimentally to provide data such as combustion by-product concentrations. This will assist in the model's development and validation.

During the thesis two burner configuration have been realized to obtain turbulent jet diffusion flames of ethylene and methane, Fig. 2.3.
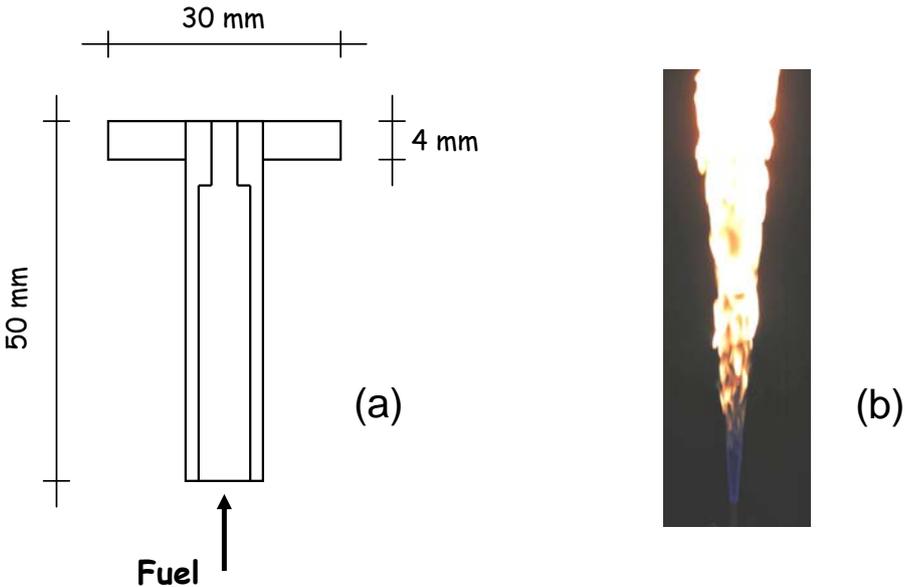
Fig. 2.3 Burner configuration for turbulent jet diffusion flames (a), turbulent jet diffusion flame of ethylene (b).

Two vertical turbulent non-premixed flames burning ethylene and methane have been obtained by flowing respectively methane from a 2.5 mm and ethylene from a 3 mm internal diameter nozzle into ambient air.

2.3 OPTICAL MEASUREMENTS

In this paragraph a short introduction to the used optical techniques, for combustion generated particles characterization, will be given. More in general, in the last years optical and spectroscopic measurements have been shown to be powerful tools for in-situ measurements of combustion by-products such as: OH, CH and other radicals, NOx, PAH, NOC and soot.

Optical diagnostics have the merit to be highly non intrusive and non invasive, if correctly applied, and able to furnish qualitative and quantitative information about the flame structure, species formed and flame pollutant emission.

On the other hand the use of these techniques needs great attention about the exact signals interpretation and about the optical properties of the species investigated.

2.3.1 LASER INDUCED INCANDESCENCE

As well reported in the recently review paper of Schulz et al. [50], and previously by Santoro and Shaddix [51], this technique has proven to be a powerful tool for particle concentration and primary particle size measurements in combustion, both in laboratory flames and in practical combustion devices.

Laser-Induced Incandescence (LII) consists in heating particles, to a temperature well above the flame temperature, by means of laser source and in measuring the correspondent, black body, radiative emission. Moreover, it has been demonstrated that while the intensity of the LII signal, "*Prompt of LII*", is correlated with the volume fraction of the particles in the detection region, the decay rate of the LII signal, "*Time Resolved of LII (TR-LII)*", is mainly a function of the primary particle size.

The first steps towards the development of this technique for soot characterization in flame were carried out by Eckbreth [52] (1977) and Melton [53] (1983).

Subsequently these early, but fundamentals, works, a great number of publications appeared in literature showing the potentialities of the LII as tool for soot characterization in many

combustion systems: laminar premixed flames, laminar and turbulent diffusion flames and practical systems like in engines.

Furthermore, these efforts toward the understanding of the LII technique have been focused on the modeling and theoretically interpretation of the LII signal and on the improvement of the experimental procedures.

On the basis of all the models, developed to describe the heating and cooling mechanisms important for LII detection of soot, there are same simplifications that can be so reassumed [54]:

- As described above soot is mainly composed by spherical particles, called primary particles, with typical diameter in the range 10 – 30 nm, that agglomerate forming structure composed by a few up to thousands primary particles, Dobbins [28]. Normally, in the LII models these aggregates are idealized as composed by particles all of identical diameter, dp, touching at only one point. Therefore the soot volume fraction is simply given by the expression: fv = (π/6) N np dp^3, where N is the number density of aggregates and np is the average number of primary particles per aggregate.

- The second simplification assumes that the LII signal is based on the energy and mass balance between a single soot particle and its surrounding rather than the aggregate.

- The third simplification requires that temperature gradients inside the particles can be neglected.

Starting from the fundamental modelling work of Melton [53] the energy balance for a spherical particle of radius a can so write:

$$K_{abs}(a)\pi a^2 q - \frac{K_a(T-T_0)(4\pi_a^2)}{a(1+GK_n)} + \frac{\Delta H_v}{M}\frac{dm}{dt} - (4\pi a^2)\varepsilon\sigma_{SB}(T^4 - T_0^4) - \frac{4}{3}\pi a^3 \rho_s c_s \frac{dT}{dt} = 0$$

where the five terms represent in the order: the absorption rate of laser energy, the heat transfer by conduction, the vaporization energy of soot, the energy loss by blackbody radiation and the change in internal energy.

However, for the correct interpretation of the incandescence signals, the different terms of the equation needs to carefully modeled.

The absorption coefficient K_{abs} of soot strongly depends on: the absorption wavelength, λ, on the particle diameter, d_i, and on the complex index of refraction of soot, $m = n+ik$. In the Rayleigh regime ($\pi d_i / \lambda << 1$) it is normally written as:

$$Kabs = -\frac{\pi^2}{\lambda}\sum_i \text{Im}\left\{\frac{m_i(\lambda)^2 - 1}{m_i(\lambda)^2 + 2}\right\}N_i d_i^{\ 3}$$

Where the complex index of refraction of soot, $m = n-ik$, is given from literature [55].

The conductivity toward the surrounding gases, must be obtained considering that the size of primary particles is smaller than the mean free path in the surrounding gases and consequently corrected for the factor $\frac{1}{1+GK_n}$, where Kn is the Knudsen number (free molecular path/ d_i) G is a geometric factor and has the expression:

$$G = \frac{8f(\gamma + 1)}{\alpha}$$

where f is the Euken factor and α is an accommodation coefficient.

The energy expended in vaporization of carbon is written in terms of heat of vaporization of carbon, ΔH_v, molecular weight of solid carbon, $M = 12$ g/mol and rate of mass vaporization, dm/dt, obtained solving mass balance:

$$\frac{dm}{dt} = 4\pi\rho_s a^2 \frac{da}{dt} = -4\pi a^2 \rho_v U_v$$

where ρ_s and ρ_v are the density of soot in vapor and solid phase respectively, U_v is the velocity with which the vapor leaves particles normally given by the relation of Langmuir:

$$U_v = \left(\frac{RT_s}{2M_v}\right)^{\frac{1}{2}}$$

in which T_s is the surface temperature of the particle, that for the simplification done is equal to that inner T, R is the universal gas constant and M_v is the molecular weight of carbon in vapor phase.

The energy loss by blackbody radiation, the radiative transfer expression, is simply given by the Stefan-Boltzmann law:

$$Q_b = \left(4\pi a^2\right)\varepsilon\sigma_{SB}\left(T^4 - T_0^4\right)$$

where σ_{SB} is the Stefan Boltzmann constant and ε is the soot emissivity that can be taken equal to the absorption coefficient Kabs.

Solving the mass and energy balances we obtain the time dependant particle size, $a(t)$ and temperature, $T(t)$, for a particular choice of the excitation wavelength, λ_{exc}, flame temperature T_0 and initial particle diameter, a_0.

Finally the LII signal must be calculated taking into consideration the density of primary particles, $N_p = N\, n_p$, and the spectral bandwidth of detection, $\Delta\lambda$, around a central wavelength λ_0:

$$LII(\lambda_0,t) = \frac{C1}{\lambda_0}\left[\exp(-\frac{C2}{\lambda_0 T(t)}-1\right]^{-1} N_p\, 4\pi a^2(t)\varepsilon(t)\Delta\lambda$$

where C1 and C2 are the first and second Planck constant. By integrating the above equations Melton showed that the LII signal at the maximum temperature (dT/dt), also called "prompt LII", is proportional to:

$$\Pr omptLII \propto Npdp^x$$

where dp is the particle diameter and the exponent x is x= 3 + 154 nm/ λ_{det}

This simple finding and the easiness of the experimental set-up promoted the development of the LII technique as the major diagnostic tool for soot detection in practical combustion systems.

Based on the Melton interpretations of the LII signal a great number of models have been developed to describe the heating and the cooling of the particles by solving the energy and mass balance equations for temperature and primary particle size. Differences and comparisons from the models are well reported in the review work of Schulz et al. [50], where a briefly description of the major models, nine in the work of Schulz, and their reference are given.

Experimentally the studies involved in the LII technique have been focused or in reproducing the incandescence signals resolved in time (TR-LII) with the aim to validate the models and consequently to obtain information on the particle's size, or in calibrating the LII signals (Prompt of LII) in order to obtain information on the volume fraction of the soot particles.

Furthermore, the accuracy of the data obtained performing LII measurements is considerably influenced by same experimental parameters:

- *Excitation wavelengths*: as know soot is a broadband absorber and in principle any wavelength in the ultraviolet, visible or IR regions can be used as exiting source to heat the particles for LII measurements. Therefore, the experimental study reported in literature involved different wavelengths in general obtained by the different harmonics of pulsed Nd:YAG lasers that are able to produce high energy pulse in very short times, typically 8 – 16 ns, suitable for LII applications. The fundamental (1064 nm) or the second harmonic (532 nm) are the most often used, while the ultraviolet excitation wavelengths, the third (355 nm) and the fourth harmonic (266 nm) and in general any shorter wavelength have been shown to increase photodissociation instead of particle heating, promoting the generation of more electronically-excited C_2 fragments. Moreover, the interference from the emission of C_2 radicals, as showed by Bengtsson and Alden [56], can be neglected in consideration of the different characteristics time of C_2 emission signals and the LII signals. Furthermore, the authors demonstrated that the influence of C_2 emission on the LII signals "is in any case not a problem since this signal is also proportional to the soot volume fraction". The use of shorter wavelengths respects to the fundamental (1064 nm) of a Nd:YAG laser, promote the fluorescence emission (LIF) of aromatic compounds, as showed by Vander Wal et al. [57]. Nevertheless, working on the LIF – LII signals optimization, the authors concluded observing that "an appropriate choice of the delay between the camera gate and the laser pulse allows the following options: (i) detection of only LII by delaying the camera intensifier gate relative to the laser pulse to discriminate against the fluorescence; (ii) optimization of both LIF and

LII signals by integrating over the maximum of these LIE signals; and (iii) detection of mostly PAH fluorescence by integrating the fluorescence signal only over the initial portion of the laser pulse". The characteristic temporal evolutions of both LIF and LII are reported in Figure 2.4, in addition to the temporal optimization adopted in the present thesis as will reported and described in the next chapter.
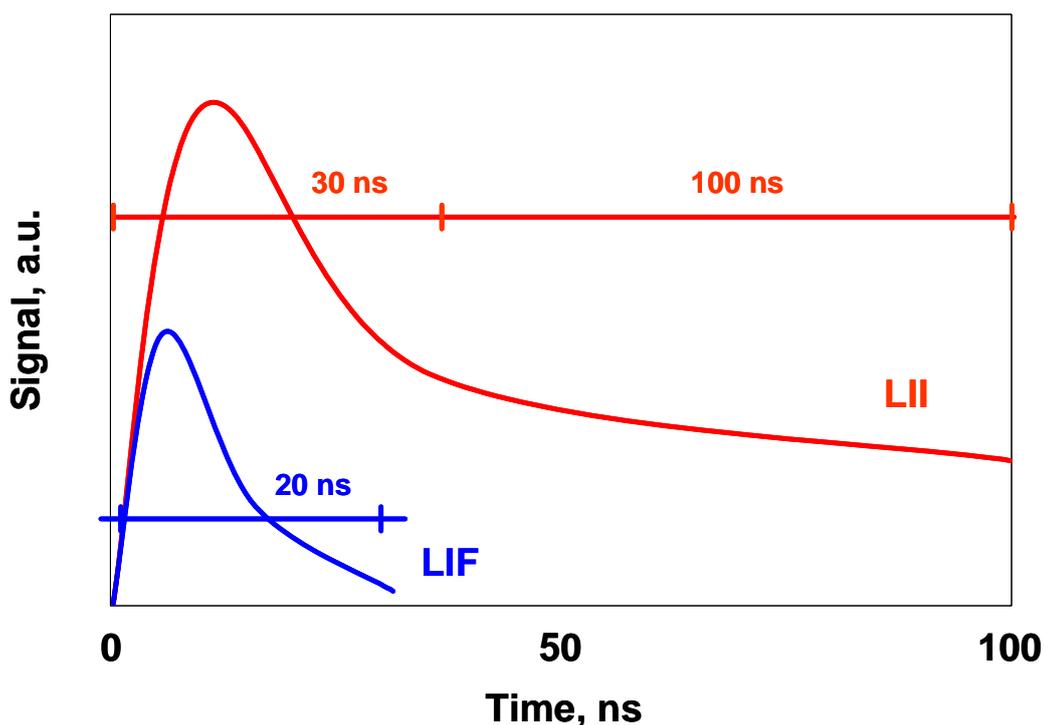
Fig. 2.4 Comparative temporal profiles of LIF (blu line) and LII (red line).

The last point regards the interference due to elastic light scattering, specially in sooting conditions. LII signals are normally detected in the visible spectral region so the light scattered at 532 nm could strongly interfere with the LII signal that needs, therefore, to be delayed as previously described for C_2 and LIF interferences.

- *Detection optimization*: the blackbody radiations, consequently the heating particles by laser, is spectrally very broad so the LII signal detection can be performed in a very wide range of waveleghts. Moreover, is relevant to observe that for measurements made in flames the detection at shorter wavelengths, normally around 400 nm, is preferred to improve the

discrimination of the LII signal against the natural flame light emission due to soot particles radiation at flame temperature, see fig. 2.5. Nevertheless, Vander Wal [58] showed that detection at longer wavelengths minimizes the influence of a variation in particle size and ambient gas temperature.
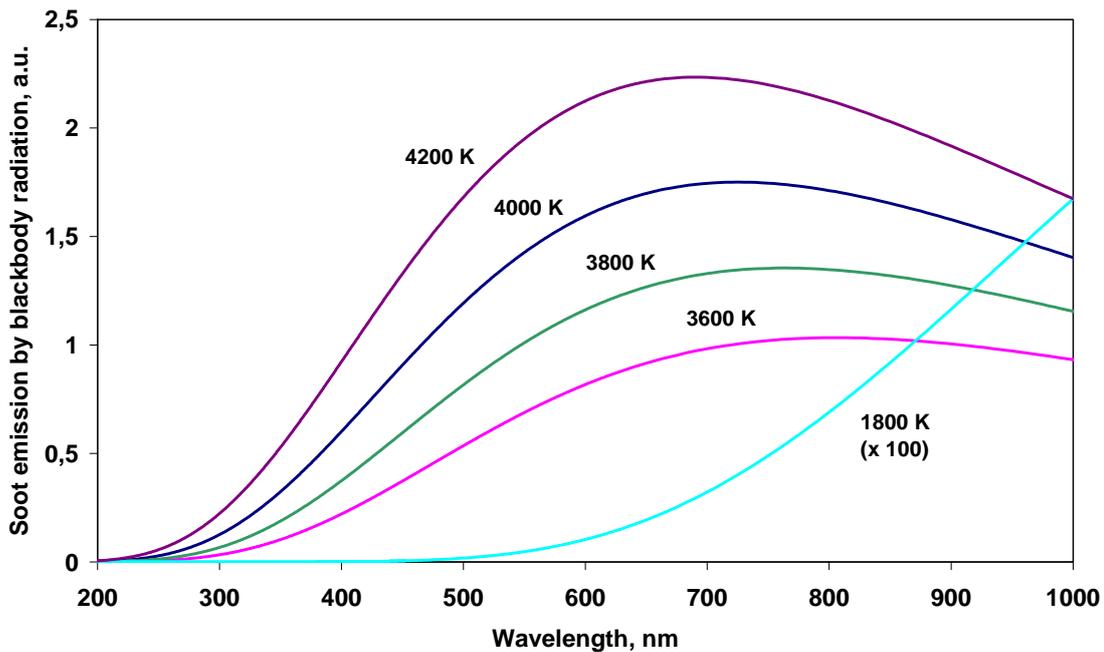
Fig. 2.5 Calculated soot emission by blackbody radiation Planck law for several soot temperatures: for temperature near to that of the vaporization (4000 °K) obtained by laser absorption, and that corresponding to soot equilibrium temperature in flame ($\approx$ 1800 K).

- *Laser fluence and laser beam spatial profile dependence*: the laser fluence, the integrate laser intensity over the duration of the laser pulse, has been showed to have a strong impact on the LII-signal intensities. This dependence of the LII signal on the laser fluence was firstly investigated by Dasch [59]. The author showed that at laser fluence of $\approx$ 0.2 J/cm^2, using the second harmonic of Nd:YAG laser (532 nm), and at $\approx$ 0.4 J/cm^2, using the fundamental (1064 nm), soot particles begin to vaporize. For fluences lower than these vaporization thresholds, the absorbed laser energy is only converted in internal energy of the particles. In these conditions increasing the laser fluence the particle's temperature increase, the LII

44

signals strongly dependent on the values of laser fluence. As the fluence approaches the threshold level, the soot begins to vaporize: a percentage of the absorbed laser energy goes into vaporizing the soot. The LII signal shows a relatively weak dependence on the laser fluence around the vaporization threshold, and the LII signal is often described as exhibiting a "*plateau*" for fluence greater than the threshold. Moreover, the details of the post-threshold LII fluence dependence, as showed in literature [47, 60, 61], are highly dependent on the laser intensity profile. For a Gaussian intensity profile [47], the general form of the dependence, Fig. 2.6 (a), shows the rapid rise of the LII signal as the laser fluence increase until the threshold value of ≈ 0.2 J/cm^2 followed by a "*plateau*" region where the slope of the curve is significantly less than that observed at lover laser fluence values. For a rectangular or "top hat" profile, Fig 2.6 (b), the LII signal achieves a maximum and the asymptotically decreases to a constant value at high fluence. Furthermore, laser fluences within this plateau region have been preferred in soot volume fraction measurements in practical applications with strong laser attenuation or laser power fluctuations.
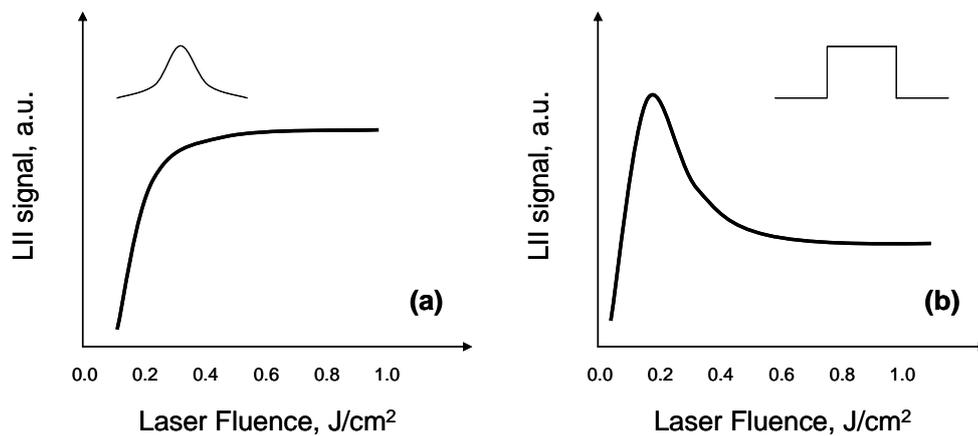
Fig. 2.6 Typical LII dependence vs laser fluence: gaussian laser beam profile (a); rectangular laser beam profile (b).

A last point that needs to be pointed out is the calibration procedure of the LII signal. In fact, even if, as showed previously, the LII signal is proportional to the volume fraction of the soot

particles, no quantitative information can be obtained without a calibration procedure. Moreover, to attempt this procedure and convert the LII signals directly in soot volume fractions information, normally, most authors have been used extinction measurements [51].

2.3.2   LASER INDUCED FLUORESCENCE

Laser-Induced Fluorescence (LIF) spectroscopy is the most common technique for the characterization of flames species, such as radical and molecular pollutant in general. The phenomenon of florescence is the spontaneous emission of radiation from an upper energy level which has been previously exited. A laser source is the most convenient manner to provide excitation. Therefore LIF can be viewed as an absorption, followed after a finite period of time, by a spontaneous emission from the exited state. (Fig. 2.7)
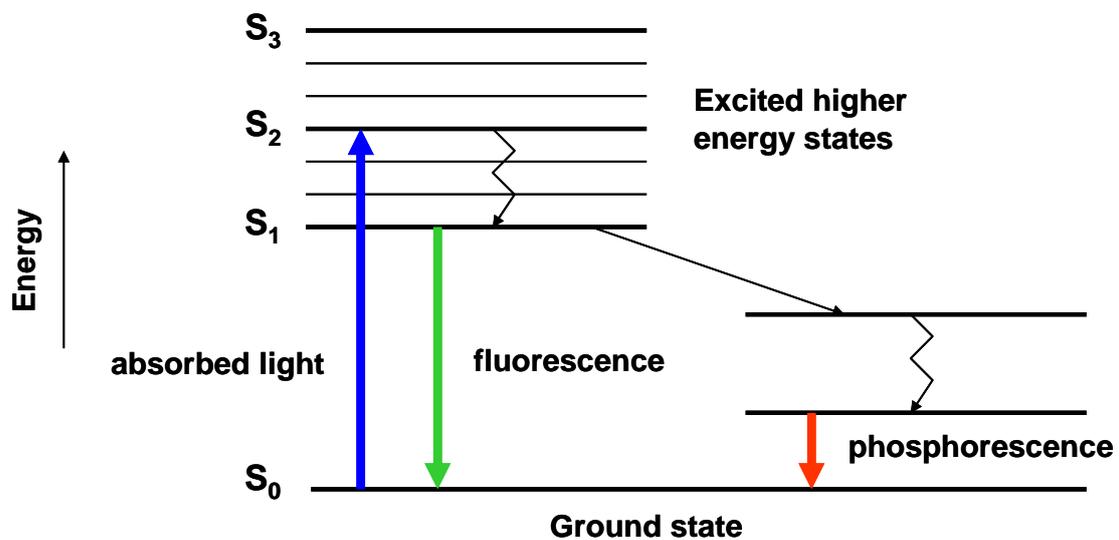
Fig. 2.7   Absorption and emission of light processes. Based on the Jablonski Energy Diagram.

Typically, fluorescence occurs at wavelengths greater than or equal to the laser wavelength. For atoms and diatomic molecules especially, discrete fluorescence transitions may be observed making the technique highly selective.

Moreover, as reported by Brockhinke and Linne [62] LIF has the vantage to being nonintrusive, flexible (several dozen combustion intermediates may be detected), of high sensitivity (down to the ppb range), high spatial resolution, and offering the possibility for time resolved, single pulse measurements.

All these characteristics make LIF the major method for qualitative and quantitative measurements of species, especially small radicals like: OH, CH and NO, in combustion environments.

Furthermore, the technique can be extended to two spatial dimensions by expanding the laser beam into a sheet (using combinations of cylindrical lenses). For these 2-D measurements, Planar Laser Induced Fluorescence (PLIF), the resulting fluorescence is typically recorded by a CCD (charge-coupled device) camera. For point measurements, photomultipler tubes are typically used. However, in most cases natural life-time of the excited state is much longer then typical collision times. Collisions might thus remove a part of the population, "quenching", decreasing the total fluorescence yield. These processes represent the most common cause for measurements uncertainties and have to be taken into account for quantitative measurements.

Most of the LIF measurements are made using a pulsed laser; the increased intensity during the short (typically 3 – 10 ns) laser pulse usually discriminates well against background emission from flame radicals [63]. For a pulsed laser, the fluorescence signal S_F, measured in a LIF experiment in a single laser pulse is given by:

$$S_F = BI_L\Gamma\tau_L Nf_B\Phi F_{fl}\left(\frac{\Omega}{4\pi}\right)\in \eta V$$

Where, B is the Einstein absorption coefficient divided by the speed of light; I_L the laser spectral power density per unit area, divided by the laser bandwidth; Γ a linewidth integral reflecting the

overlap between laser and absorption line bandwidths; τ_L the laser pulse length; N the number of molecules in the ground electronic state; f_B, often termed the Boltzmann fraction, the portion of those molecules in the particular electronic-vibrational-rotational levels being excited by the laser; Φ the fluorescent quantum yield from the excited state, that is, the number of photons emitted per molecule excited and a key quantity affected by collisions and dissociation; F_{fl} the fraction of fluorescence collected within the detector bandwidth. The remain terms are Ω, the solid angle of fluorescence collected by the detector, ϵ and η the transmission and photoelectron efficiencies of the detector system, and V the interaction volume observed [63].

LIF technique can also be used to study PAH and high molecular mass compounds as showed by D'Alessio et al. [20-22] and by Ciajolo et al. [64, 65].
Moreover, recently, Bruno et al [66] employed the technique of time resolved fluorescence anisotropy to combustion products. These measurements allowed to determine the rotational diffusivity of the fluorescing species confirming their particulate nature.

2.3.3 LIGHT EXTINCTION

Monochromatic or spectral light extinction is the most used and common in-situ diagnostic for soot concentration measurements. The extinction coefficient (Kext) is composed by two terms, the absorption coefficient (Kabs) and the scattering coefficient (Kscat):

$$Kext = Kabs + Kscat$$

However, assuming that particles are within the Rayleigh size limit with respect to the incident light source (particle size << wavelength), the extinction coefficient can be approximated to the absorption one and it is given by the followed relation:

$$Kext = Kabs = \frac{6\pi E(m)}{\lambda} f_V$$

Where is the wavelength of the relevant light source, f_V is the particles volume fraction and E(m) is a function of the refractive index of the particles, $m = n - ik$, given by:

$$E(m) = -\mathrm{Im}\left(\frac{m^2 - 1}{m^2 + 2}\right) = \frac{6nk}{\left(n^2 - k^2 + 2\right)^2 + 4n^2 k^2}$$

Furthermore, for polydisperse spheres in the Rayleigh size limit the extinction coefficient may be written as:

$$K_{ext} = K_{abs} = \frac{-\pi^2}{\lambda} \sum_i \mathrm{Im}\left(\frac{m_i^2(\lambda) - 1}{m_i^2(\lambda) + 2}\right) N d_i^3$$

Where N_i (cm^{-3}) is the particle number density, m_i is the refractive index and d_i the particle diameter.

Therefore, known the optical properties of the absorbing species, the particles volume fraction can be obtained, experimentally, by measuring the absorption coefficient using the Lambert – Beer law:

$$\frac{I}{I_0} = e^{-K_{abs}(\lambda)l}$$

Where l is the finite pathlength, the distance that the light travels through the material, I_0 and I are the incident and the transmit intensity of the light.

The use of the Lambert – Beer law allows to easily and directly perform particles volume fraction measurements (soot and NOC) in a uniform flow field (Fig. 2.8 (a)), i.e. f_V constant in all the finite pathlength l, for example in laminar premixed flames [20 – 22, 26].

Different is the case of 2-D flow fields, for example, in axisymmetric laminar and turbulent diffusion flames (Fig. 2.8 (b)). Tomographic techniques are therefore needed for reconstruction of the two-dimensional quantity under investigation. In particular, an Abel inversion can be used to reconstruct a cylindrically symmetric distribution from line-of-sight intensity measurements, Fig. 2.8 (b). This deconvolution is valid only when the measured signal is collected along infinitely thin, perfectly parallel rays [67, 68].

For these flame configurations, single-point measurements, i.e. LII and LIF, are more suitable than the absorption one.

$$\frac{I}{I_0} = e^{-K_{abs}(\lambda)l}$$
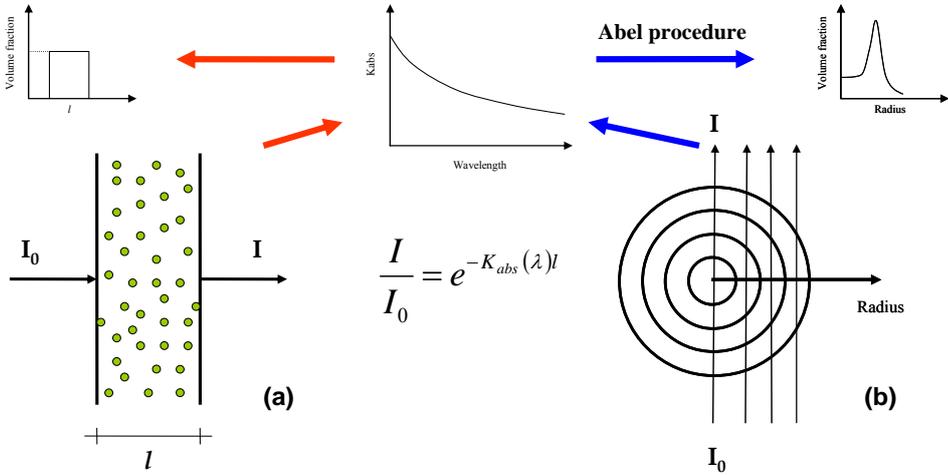
Fig. 2.8 Absorption measurements configuration for a uniform flow field (a), and in a 2-D flow field (b).

2.3.4 ELASTIC LIGHT SCATTERING

Laser light scattering coupled with extinction measurements have been extensively used in combustion environments as tool for particle characterization.

With reference to the Fig. 2.9, when the beam of the laser passes through a cloud of spherical particles, the oscillating electric field, which is perpendicular to the direction of propagation of the wave, causes the electric charges of the particles to be set into forced oscillations with a frequency equal to the frequency of the incident light. These oscillating electric charges constitute sources of electromagnetic radiation, and hence generate what is termed *scattered light* [43].

The measured scattered light S_{pp} is related to the properties of the particles and the parameters of the optical system by the expression [43]:

$$S_{pp} = I_{pp} \Delta\Omega \Delta V K_{pp} \eta_{opt} \tau_{\lambda}$$

where I_{pp} is the incident energy flux, $\Delta\Omega$ the solid angle aperture of the collection optics, ΔV is the scattering volume and η_{opt} accounts for the efficiency of the optical and electronic components comprising the detection system. The subscript p denotes the polarization stat (vertical or horizontal, see fig. 2.9), the first for the incident beam and the second for the scattered beam.
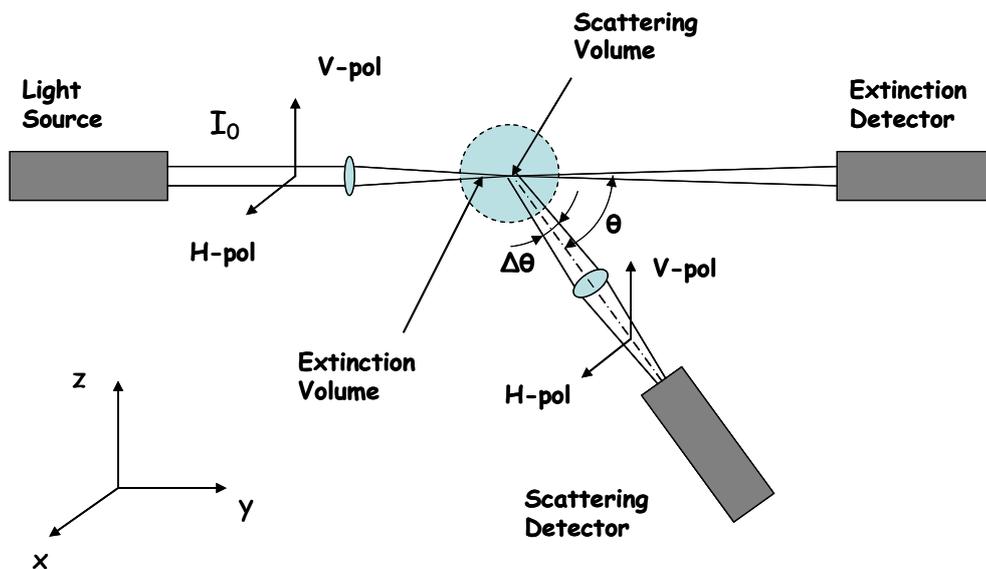
Fig. 2.9 Light scattering and extinction experimental set-up. Adapted from D'Alessio A. [69].

The parameter K_{pp} (cm^{-1}sr^{-1}) denotes a differential scattering coefficient and is defined as the energy scattered per unit time and per unit volume into a unit solid angle direction θ. Finally, τ_λ, is introduced to account for the attenuation of the scattering when it travels between the scattering volume and the detector.

The mean scattering coefficient for a size distribution of particles is given by:

$$K_{pp} = N\overline{C}_{pp}$$

Where N (cm^{-3}) is the particle number density and $\overline{C}_{pp}$ (cm^{2}sr-1) is the mean cross-section for all spheres in the scattering volume given by:

$$\overline{C}_{pp} = \int_{r=0}^{\infty} C_{pp} P(r)dr$$

Where C_{pp} is the differential scattering cross-section for a single homogeneous spherical particle of radius r.

In the Rayleigh size limit, particle diameters much smaller than the incident wavelength, the expression of C_{pp} in the vertical polarization orientation is:

$$C_{VV} = \frac{\pi^4}{4\lambda^4} \sum_i \left| \frac{m_i^2 - 1}{m_i^2 + 2} \right|^2 d_i^6$$

And the horizontal polarization orientation is given by:

$$C_{HH} = C_{VV} \cos^2 \theta$$

Finally, by combining these equations the differential scattering for Rayleigh size polydisperse particles is expressed as:

$$K_{VV} = \frac{\pi^4}{4\lambda^4} \sum_i \left| \frac{m_i^2(\lambda) - 1}{m_i^2(\lambda) + 2} \right|^2 N_i d_i^6$$

Under the assumption of monodisperse system of particles, the mean particle size may be determined by combining the measured scattering and extinction coefficients, obtaining the followed relation:

$$\frac{K_{ext}}{K_{VV}} = \frac{-\lambda^3 \, \mathrm{Im}\left\{ \dfrac{m^2(\lambda) - 1}{m^2(\lambda) + 2} \right\} \sum_i N_i d_i^{\,3}}{\pi^2 \left| \dfrac{m^2(\lambda) - 1}{m^2(\lambda) + 2} \right|^2 \sum_i N_i d_i^{\,6}} = f[m(\lambda), \lambda] \frac{1}{d^3_{\,63}}$$

Where d_{63} is the average diameter of the particles.

2.4 SCANNING MOBILITY PARTICLES SIZER (SMPS)

Optical measurements have been compared in some flames with the Particles Size Distribution Functions (PSDF), obtained by Scanning Mobility Particles Sizer (SMPS).

To perform SMPS measurements, in flame or at the exhaust of combustion systems, a nano differential mobility analyzer TSI Model 3936 has been used. This apparatus is specifically designed to measure particles in the 3–50 nm range. The SMPS system consists of:

- *A diffusion charger (Kr-85 Bipolar);* the aerosol enters a Kr-85 Bipolar Charger (or neutralizer), which exposes the aerosol particles to high concentrations of bipolar ions. The particles and ions undergo frequent collisions due to the random thermal motion of the ions. The particles quickly reach a state of equilibrium, in which the particles carry a bipolar charge distribution [70].

- *A Nano-Differential Mobility Analyzer (NDMA, type TSI 3085);* The charged aerosol passes from the neutralizer into the main portion of the Differential Mobility Analyzer (DMA), shown in Figure 2.10. The DMA contains two concentric metal cylinders. The polydisperse aerosol (qa) and sheath air (qsh) are introduced at the top of the Classifier and flow down the annular space between the cylinders. The aerosol surrounds the inner core of sheath air, and both flows pass down the annulus with no mixing of the two laminar streams. The inner cylinder, the center rod, is maintained at a controlled negative voltage, while the outer cylinder is electrically grounded. This creates an electric field between the two cylinders. The electric field causes positively charged particles to be attracted through the sheath air to the negatively charged center rod. Particles are precipitated along the length of the center rod (see Fig. 2.10). The location of the precipitating particles depends on the particle electrical mobility (Zp), the Classifier flow rate, and the Classifier geometry. Particles with a high electrical mobility are precipitated along the upper portion of the rod; particles with a low electrical mobility are collected on the lower portion of the rod. Particles within a narrow

range of electrical mobility exit with the monodisperse air flow (qm) through a small slit located at the bottom of the center rod [70].

- ***An Ultrafine Condensation Particle Counter (UCPC, type TSI 3025A).*** The mechanism used to grow particles in the CPC is heterogeneous condensation, whereby particle growth is promoted by the presence of condensation nuclei. The CPC uses this mechanism to measure the number concentration of submicrometer aerosol particles [70]. The saturation ratio of the condensing vapor determines the smallest particle size detected by the CPC. The saturation ratio is defined as the actual vapor partial pressure, p, divided by the saturation vapor pressure, ps, at a given temperature. The condensing vapor was butyl alcohol.

Detail on the SMPS, theory and procedures, can be found in the reference [70].
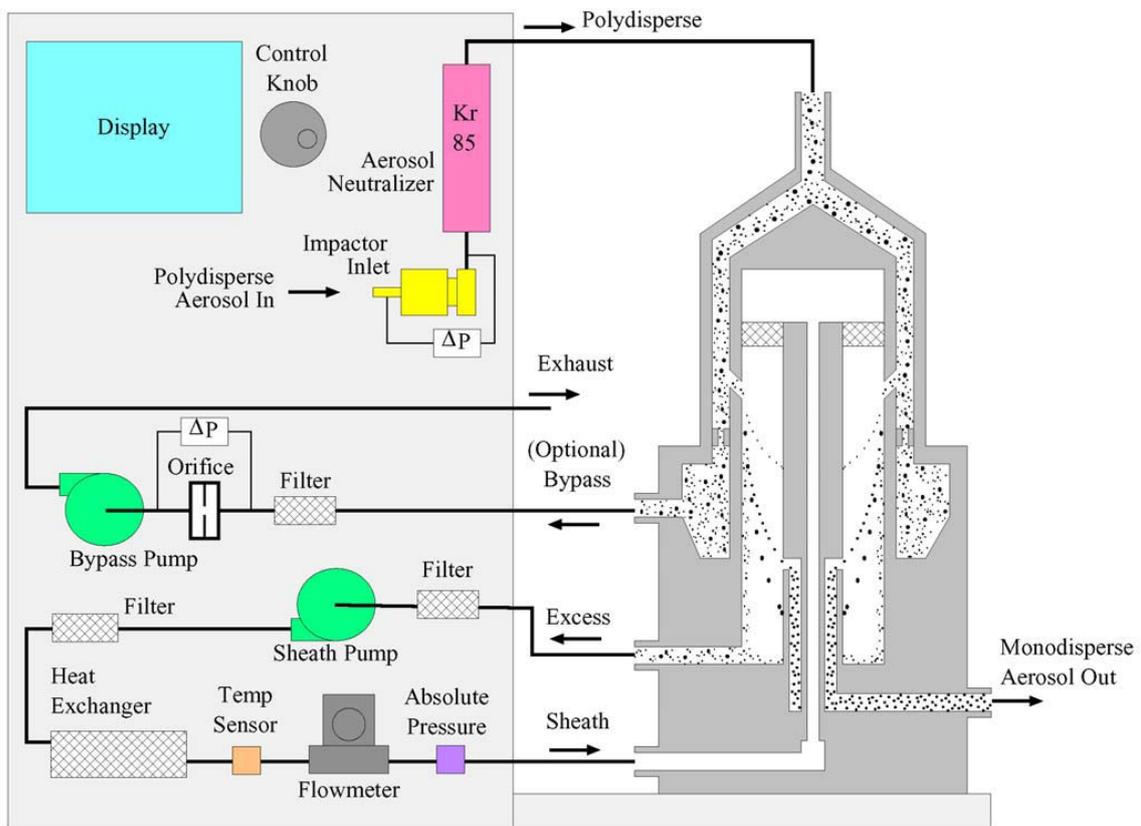
Fig. 2.10 Flow Schematic for the Electrostatic Classifier with Nano DMA [70].

2.5 TEMPERATURE MEASUREMENTS

A complete flame characterization needs the knowledge of the flame temperature profile, because the maximum flame temperature (T_{max}) may be considered as a marker of the position of the flame front.

To perform temperature measurements, thermocouple directly entered within the flame to the desired location are typically used. However, when the thermocouple is inserted into a particles-forming flame, NOC or soot particles deposit on the thermocouple junction determining an increase in both emissivity and diameter of the thermocouple junction, as showed by Rolando et al. [71]. Since these parameters are required to calculate the gas temperature from the indicated junction temperature, particulate deposition can greatly increase the error in the temperature measurement. To minimize such errors, many authors use a procedure, developed by Kent and Wagner [72]: a soot-free thermocouple is rapidly swept into the flame to the desired measurements location and its junction temperature is measured as quick as possible.

Furthermore, temperature, is not the only information that a thermocouple inserted within a flame can provide. Eisner and Rosner [73] in the 1985, and subsequently McEnally et al. [48] developed a method, called Thermocouple Particle Densitometry (TPD), for measuring absolute soot volume fraction in flames following the temporal history of a thermocouple rapidly inserted into a soot-containing flame region, and then optimizing the fit between this temperature-flame history and the one calculated from the principles of thermophoretic mass transfer. McEnally et al. [41] studying methane and ethylene laminar diffusion flames found that soot volume fractions inferred from TPD method was in agreement with those inferred by extinction measurements. However the authors point out the soot volume fractions by mass deposition were larger than extinction results in the lower portion of the ethylene flame, and throughout the methane one, possibly due to deposition of high mass visible light-transparent particles. This was also observed by D'Alessio et al. [20 - 22] studying sooting and non-sooting flames by optical

techniques and subsequently by Rolando et al. [71] who implemented this method to detect both soot and nanoparticles in a ethylene co-flowing diffusion flame.

2.6 EXPERIMENTAL LAY-OUT AND INSTRUMENTS

To perform optical and spectroscopic measurements, all the flames analyzed, laminar premixed flames, laminar an turbulent diffusion flames, have been characterized by ultraviolet laser-induced spectroscopy using the fifth or the fourth harmonic of a pulsed Nd:YAG laser ($\lambda 0 = 213$ nm and $\lambda 0 = 266$ nm) as exciting source. The pulse energy was kept constant and opportunely attenuated to avoid excessive photo-fragmentation or particle vaporization, while the pulse duration was 8 ns (FWHM). The laser beam was focused at the selected position within the flame with a 500 mm focal lens. The collected signal at 90° respect the incident beam was focused onto a 50 μm, or 280 μm, entrance slit of a spectrometer and was detected by a gated ICCD camera. The experimental components and their configuration for optical measurements is schematically reported in fig 2.10.
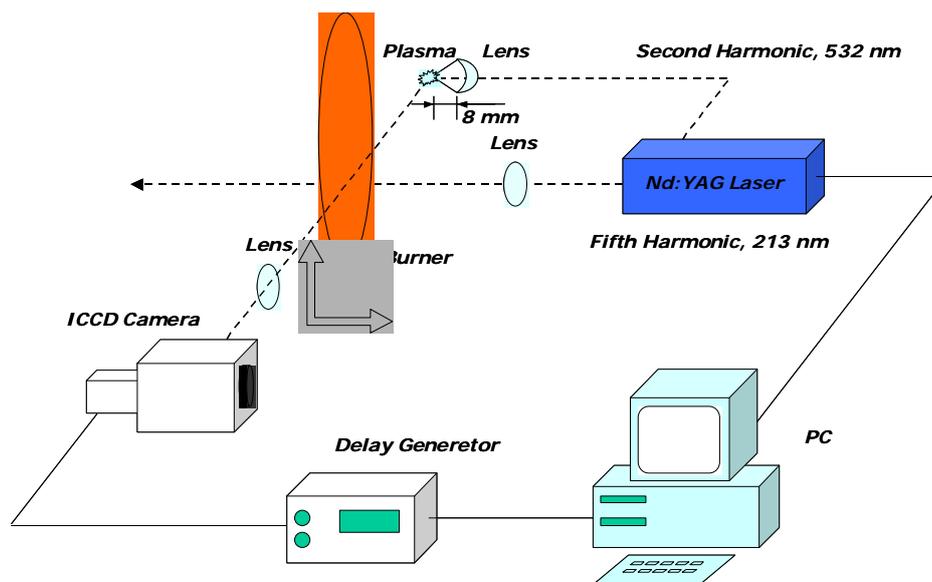
Fig. 2.10 Lay-out of the optical set-up for laser induced spectroscopy and extinction measurements.

A delay generator has been also used for the optimization of the acquisition times relative to the different emitted signals. As reported by Vander Wal et al. [57] the different temporal decay of the emission processes allows to distinguish between LIF and LII signals.

The acquired spectra are corrected for the wavelength-dependent sensitivity of the detection system. Calibrations of laser light scattering and of laser induced emission (LIF and LII) are made on cold ethylene signals. The choice of the fifth, or the fourth harmonics far in the UV is due to previous extinction characterization of the combustion by-products [20-22]. The use, in fact, of these exiting wavelengths allows us to readily excite electronic transitions in a variety of aromatic intermediates resulting in fluorescence (LIF). Also, 213 or 266 nm light is readily absorbed by soot particles producing laser induced incandescence (LII).

UV−visible absorption spectra were determined by using a broadband light source. It was obtained by focusing the second harmonic of the laser (λ=532 nm) into air with a short focal lens, which induces an optical breakdown. The high temperature plasma produces a high intensity light source in the spectral range of 200 − 800 nm with time duration of tens of nanoseconds, suitable for absorption measurements in the UV − visible as reported by Borghese et al. [74]. Spectral extinction measurements have been also performed by using a high-pressure Deuterium lamp that produces a high intensity light source in the spectral range of 200 − 500 nm, suitable for absorption measurements in the UV.

Temperature measurements have been performed with a Pt/Pt-13%Rh thermocouple with a bead diameter of 300 μm using the mentioned rapid insertion procedure to minimize soot deposition on the thermocouple bead. Temperature measurements are corrected for radiation losses.

CHAPTER 3

LAMINAR PREMIXED FLAMES

The first group of measurements have been performed in laminar premixed flames burning: ethylene, methane and benzene. All the flames have been studied changing the equivalent ratio $\Phi = (C/O)/(C/O)_{stoic}$ and the Height Above the Burner (HAB) with the aim to investigate non-sooting, lightly-sooting and sooting flame conditions.

Ethylene flames were firstly investigated in order to develop a new optical diagnostic based on the use of the fifth harmonic of a Nd:YAG laser for laser-induced emission spectroscopy. A calibration procedure has been obtained allowing the use of the technique in any other combustion environment.

Subsequently, methane and benzene flames were studied in order to establish effects on combustion formed particulate due to fuel composition.

3.1 LAMINAR PREMIXED ETHYLENE FLAMES

Laminar premixed ethylene flame have been extensively investigated for different C/O ratios ranging from the stoichiometric value at 0.33 to fully-sooting regimes at 0.92. The cold gas flow velocity was kept constant for all the flames at 10 cm/s. Measurements were performed at different heights above the burner, from 3 mm (just downstream of the flame front) up to 20 mm (in the post-oxidation region). Typical fluorescence and incandescence spectra obtained by using the fifth harmonic (213 nm) will be reported and described. The study of these spectral signals, then, has been made in terms of laser power, emission times signals and wavelengths dependences. Finally comparing LIF and LII signals, opportunely collected, with extinction data a calibration procedure has been obtained, allowing quantitative information, about particles concentrations, in the investigated flames.

3.1.1 LASER INDUCED EMISSION SPECTRUM

Typical LIF and LII spectrum, in the camera-spectrograph wavelengths limit 250 – 550 nm, are reported in Fig. 3.1. The signals are obtained by accumulation of 150 shots in a flame with C/O=0.85 for two different HAB: 4 mm HAB, in the blue-color flame region, Fig. 3.1 (a), and at 10 mm HAB, in the yellow-color flame region.

Figure 3.1 (a) shows a broad signal in the region between 270 and 450 nm with a maximum at about 350 nm, some excited carbon atom emission and hints of C_2 Swan-bands.

The spectral behavior between 270 and 450 nm is typical of fluorescence from aromatic compounds [21] whereas the continuum which extends into the visible is attributable to incandescence of soot particles [57,58].
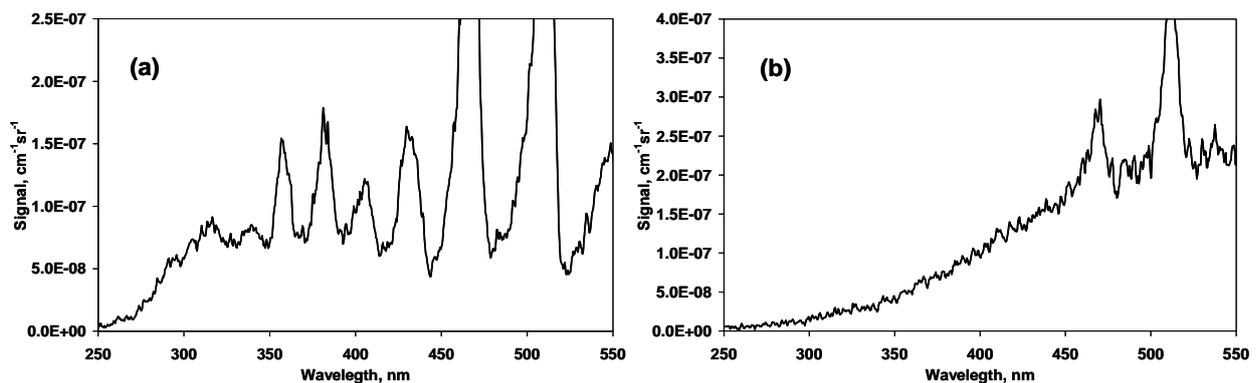
Fig. 3.1 Typical laser induced emission spectra measured in a ethylene/air flame with C/O=0.85 at 4 mm HAB (a) and 10 mm HAB (b).

3.1.2 LASER POWER, TIME AND WAVELEGTH SPECTRUM DEPENDENCE

Since the fifth harmonic (213 nm) of a Nd:YAG laser has been never investigated previously and no data are available in literature, the correct use of the technique required same preliminary investigations, particularly on the laser dependence, acquisition time optimization and wavelengths range of the spectral emission.
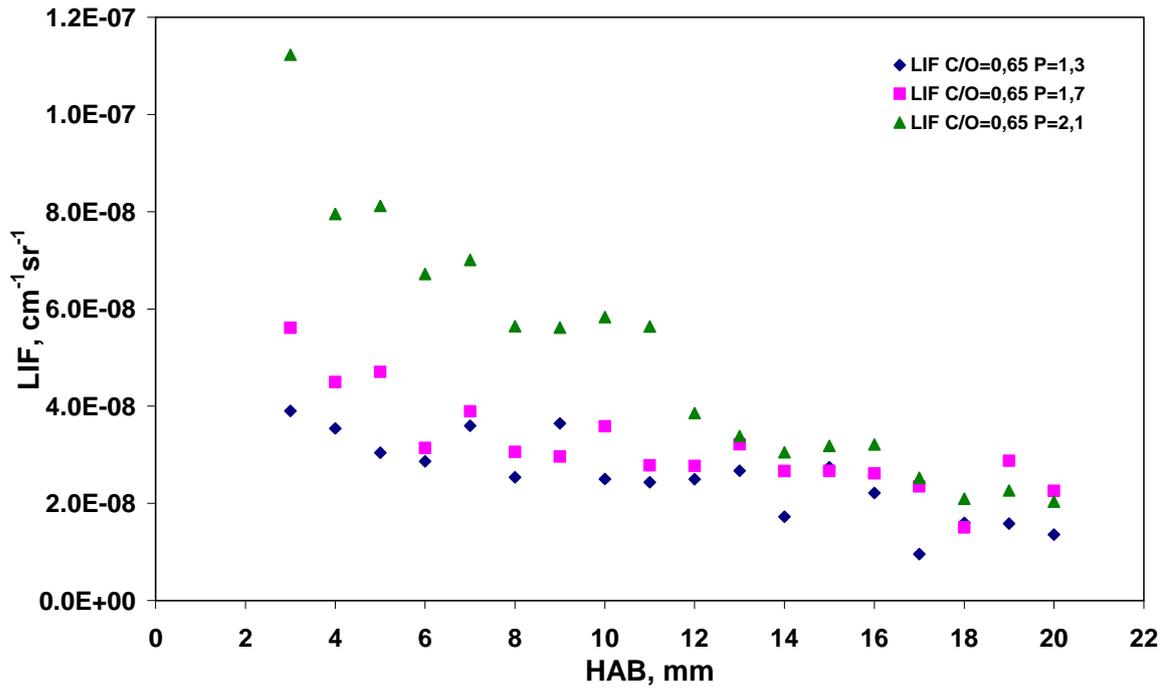
Fig. 3.2 LIF signals as function of HAB for a ethylene/air flame with C/O=0,65 and velocity of cold gas 10cm/s. The different symbol are relative to different laser power.
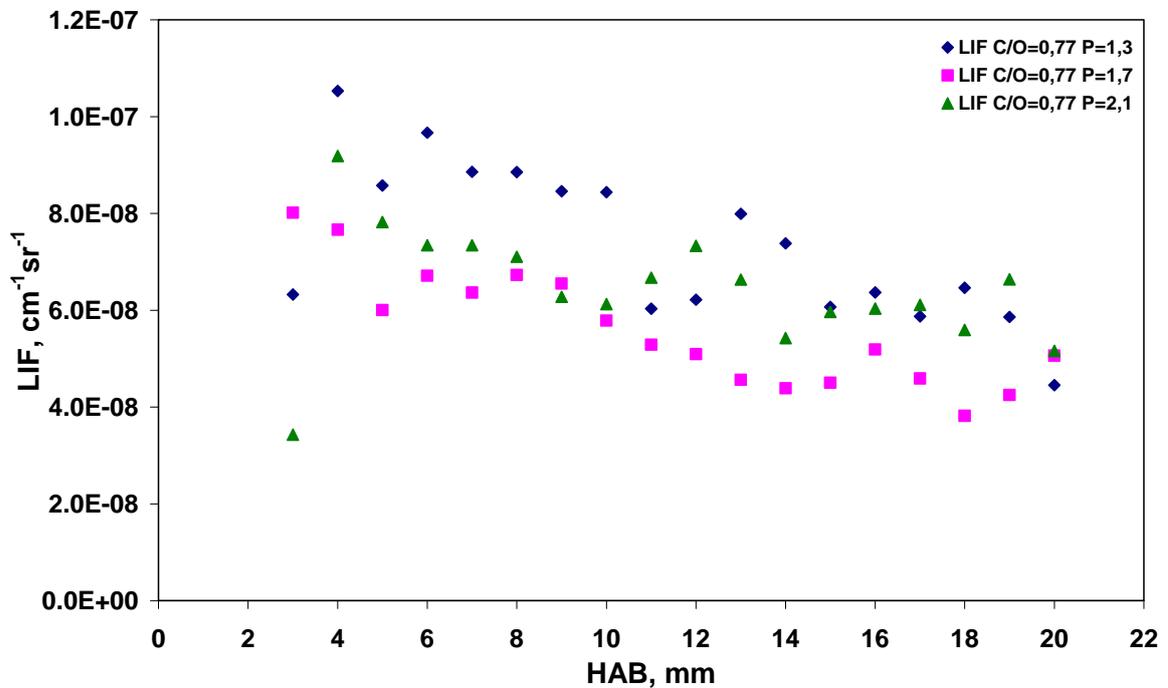
Fig. 3.3 LIF signals as function of HAB for a ethylene/air flame with C/O=0,77 and velocity of cold gas 10cm/s. The different symbol are relative to different laser power.
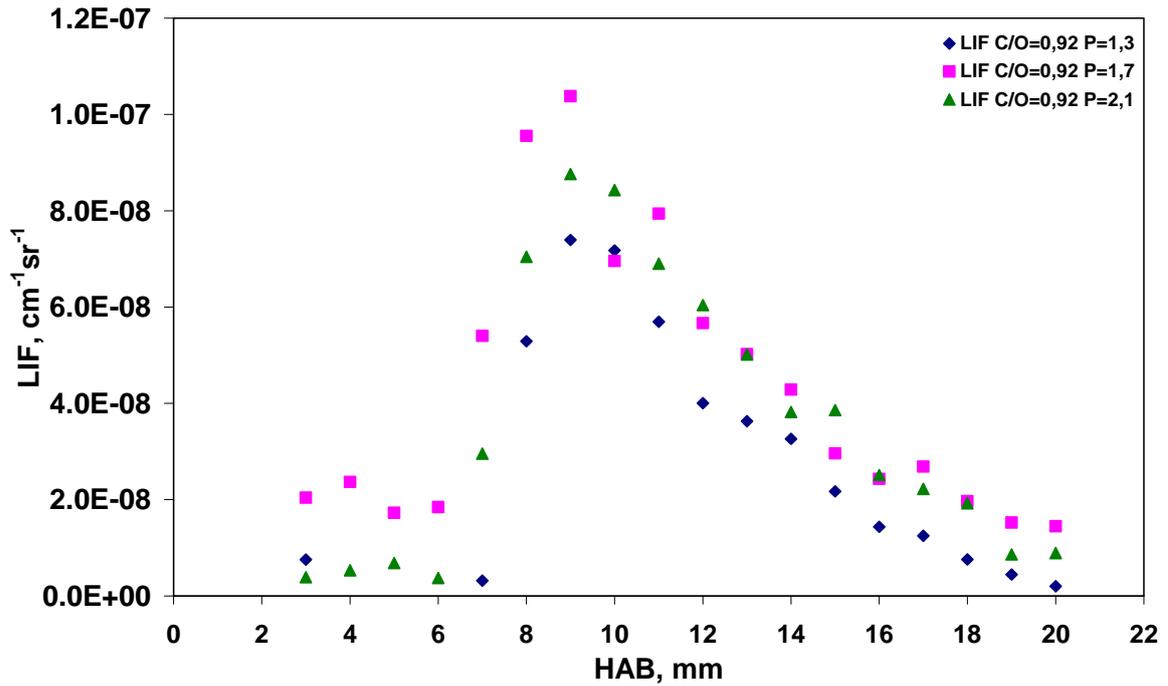
Fig. 3.4 LIF signals as function of HAB for a ethylene/air flame with C/O=0,92 and velocity of cold gas 10cm/s. The different symbol are relative to different laser power.
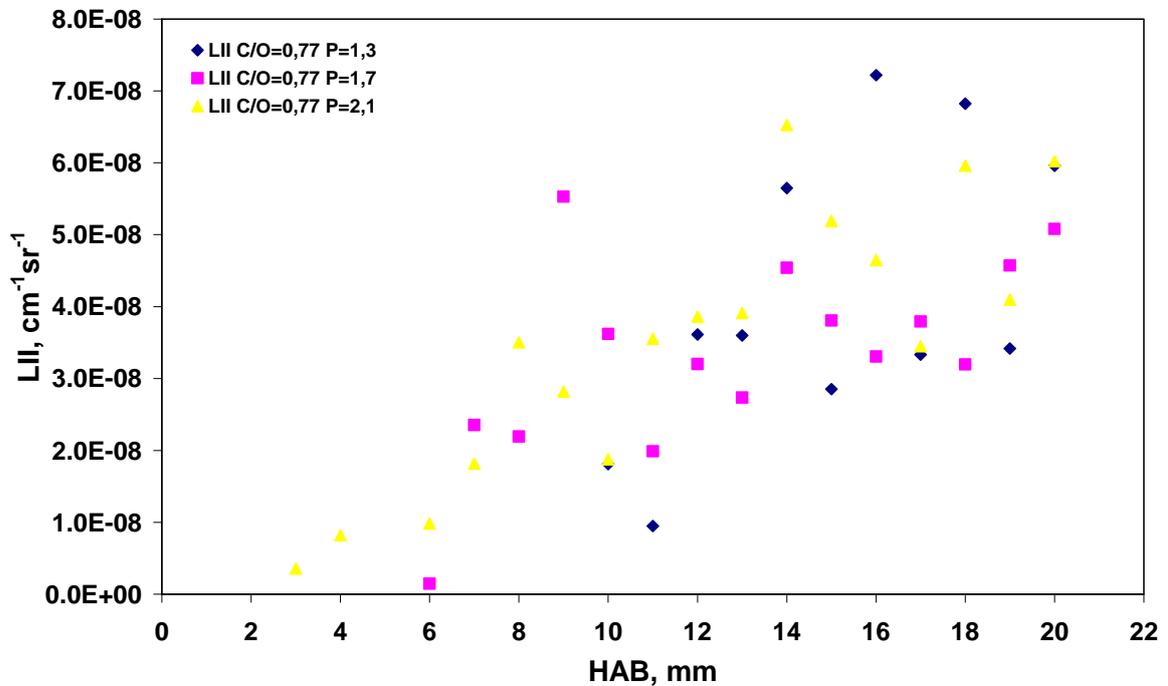
Fig. 3.5 LII signals as function of HAB for a ethylene/air flame with C/O=0,77 and velocity of cold gas 10cm/s. The different symbol are relative to different laser power.
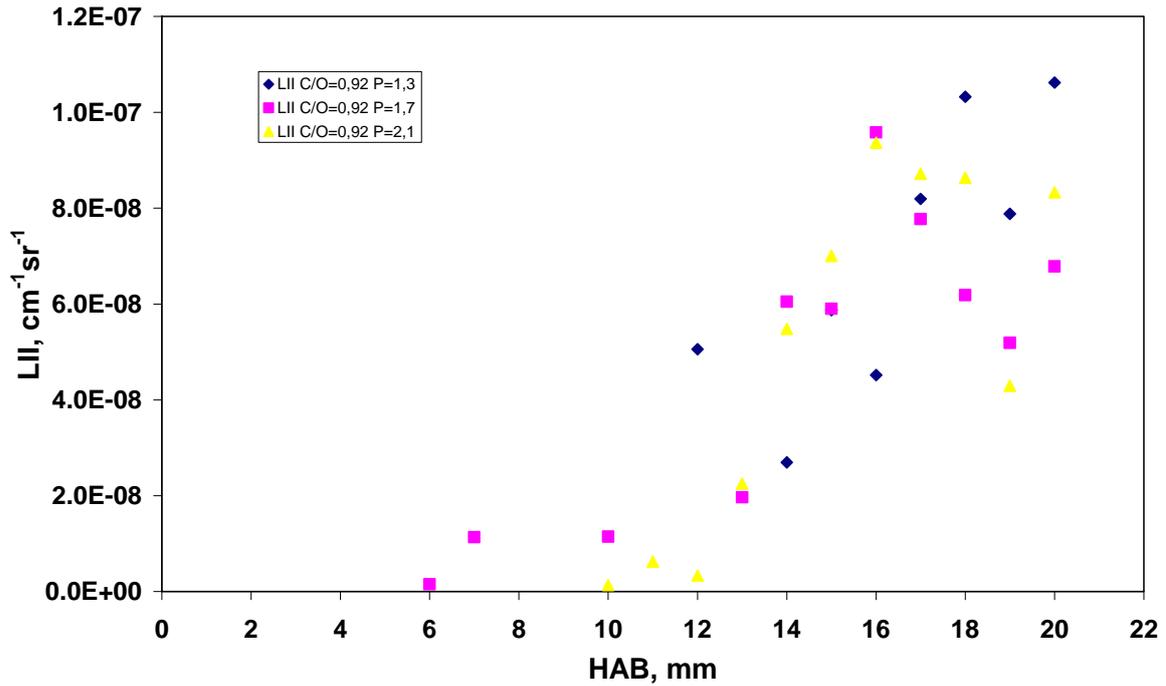
Fig. 3.6 LII signals as function of HAB for a ethylene/air flame with C/O=0,92 and velocity of cold gas 10cm/s. The different symbol are relative to different laser power.

Figures from 3.1 up to 3.6 shown several LIF and LII data collected in premixed ethylene/air flames as function of HAB changing the C/O ratio and the incident laser power.

For all conditions both LIF and LII intensity do not change in the investigated power range being within the typical plateau region. Moreover considering the particle temperature, subsequent the laser heating, reported in Fig. 3.7, which was obtained by fitting the experimental laser induced emission spectra with the Planck's Law equation, can be observed that above 1.5 mJ the particles vaporization temperature of about 4000K is reached and incandescence, as well as the C2 signal due to vaporization, remains constant. This observation justify the choice to operate at of laser power of 1.5 mJ for a correct use of the technique, as previously reported in literature [50, 51]. The influence of the delay acquisition times is reported in Figure 3.8.

Signals are collected fixing the duration of the acquisition at 20 nm and changing the delay time every 2 ns. Figure 3.8 (a) shows a LIF signal (at 300 nm) faster than typical C_2

photofragmentation signal (at 512 nm). Moreover both signals are faster than LII signal characterized from a duration of hundreds of nanoseconds as reported by Vander Wal [57].
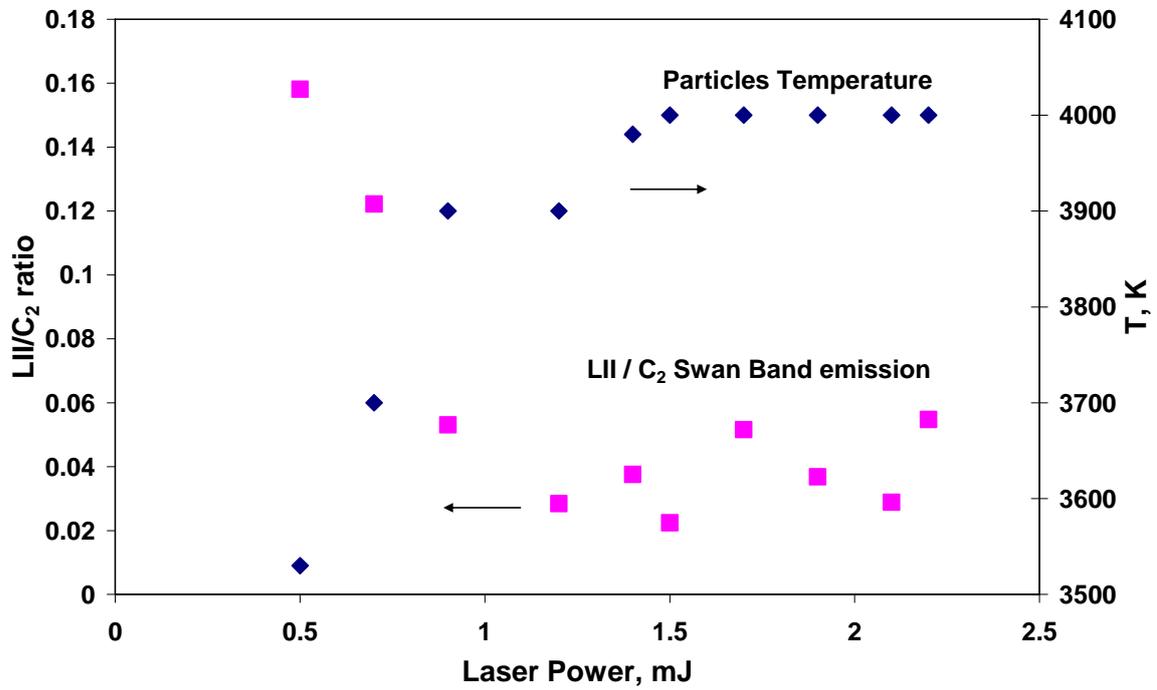
Fig. 3.7 Particles Temperature and LII/C2 ratio as function of the laser power.
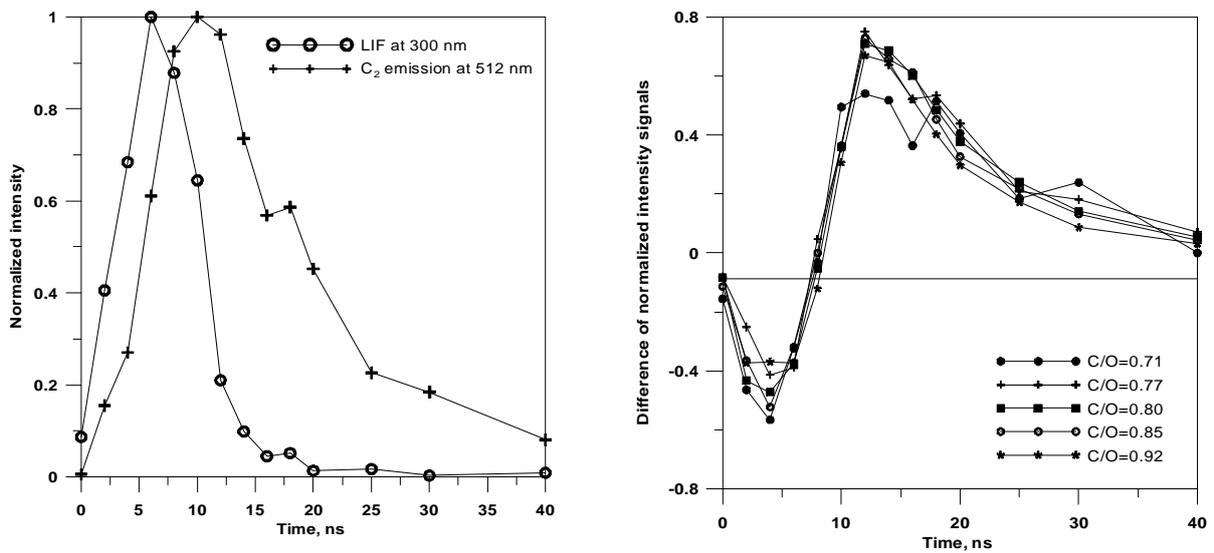
Fig. 3.8 Temporal evolutions for 300 nm e 512 nm at 3.5 mm HAB, C/O= 0.77, (a). Temporal evolution of the difference between normalized peak emission at 512 and normalized peak emission 300 nm for different C/O ratios at 3.5 mm HAB, (b).

The different temporal decay of the emission processes allows us to distinguish between LIF and LII by fixing the delay time at 8 ns after the laser pulse (acquisition duration of 20 ns) and 40 ns (acquisition duration of 100 ns) respectively.

Furthermore, the choice to collect the ultraviolet fluorescence signals at 300 nm is due to the fact that at 300 nm the fluorescence showed very broad and very close to the spectra maximum.

The LII signals, instead, have been collected at 500 nm, in visible spectra region, according to that reported in literature [50, 51].

3.1.3 SIGNALS CALIBRATION

To allow quantitative information about particles concentrations from in-situ optical measurements, LIF and LII collected in the described procedures need to be calibrated. The calibration procedures have been based on the use of extinction measurements that consent to estimate the volume fraction of both NOC and soot particles once the optical properties of the two classis are know [75]. Calibration measurements were performed in a premixed ethylene/air flame with C/O=0.85 and a cold gas velocity of 10 cm/s. LIF and LII signals were then compared with ultraviolet and visible light extinction coefficients measured at the same flame locations.

Figure 3.9 reports the LIF signals collected at 300 nm and the NOC's volume fraction, by ultraviolet extinction measurements, as function of HAB, whereas in Fig. 3.10 are reported the LII signals collected at 500 nm and soot volume fraction, by visible extinction measurements. These correlations allow as to calibrate both LIF and LII in order to obtain separate information on the two particles classis by the followed proportionality:

$$LIF \propto fv_{NOC} \qquad\qquad LII \propto fv_{Soot}$$
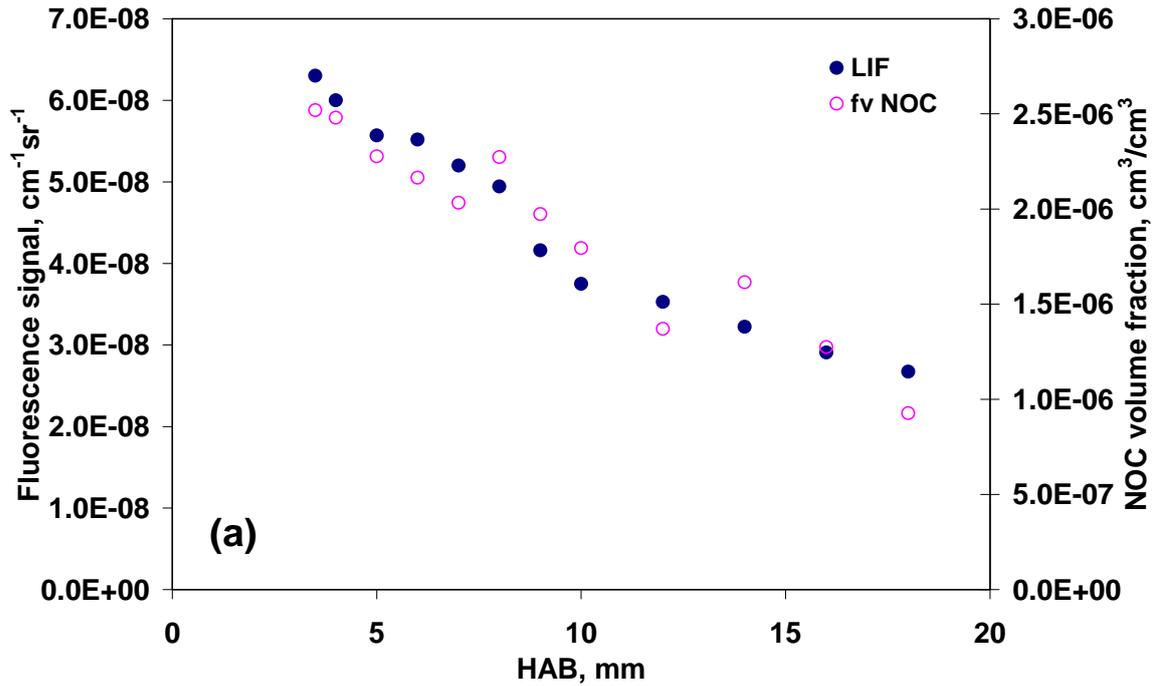
Fig. 3.9 Fluorescence signals and NOC volume fractions as function of HAB; C/O=0.85.
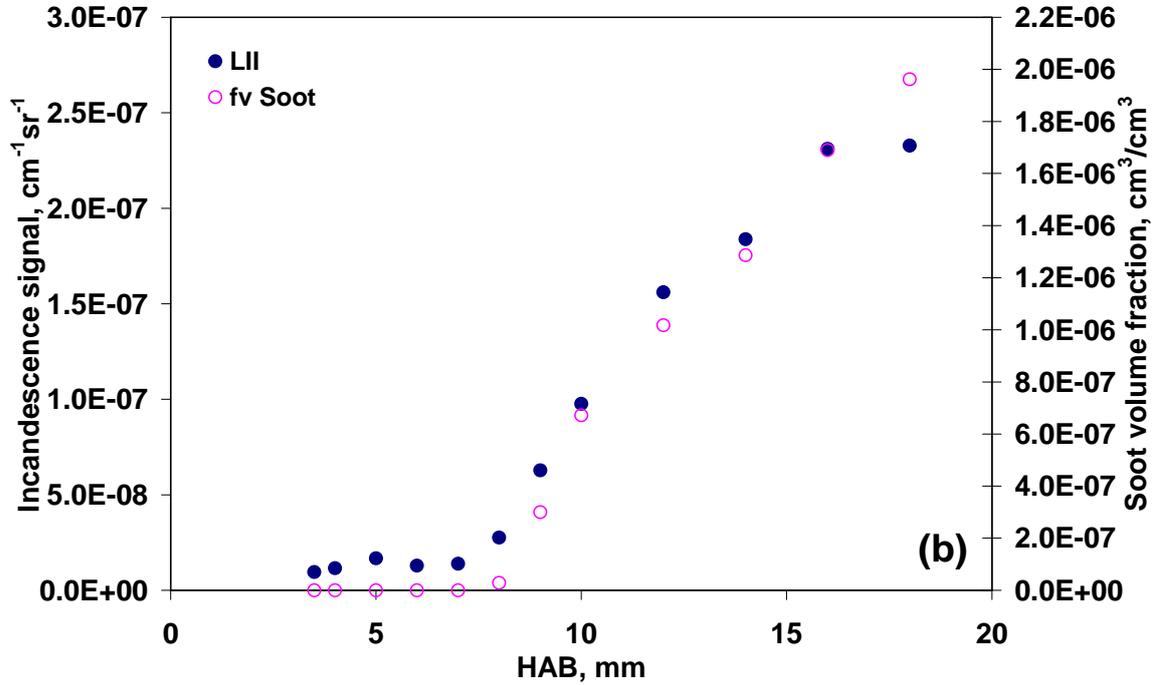
Fig. 3.10 Incandescence signals and soot volume fractions as function of HAB; C/O=0.85.

3.2   LAMINAR PREMIXED METHANE FLAMES

Natural gas is widely used as source of energy for many of our activities and particularly for home appliances, power generation and in transportations. It is, in fact, believed to be a clean fuel which does not produces soot and pollutants. As a consequence it is of great interest to study the combustion of methane, the major component of natural gas, and its by-products in different combustion systems. Therefore, particulate formation by methane combustion has been firstly investigated in laminar premixed conditions. Soot and NOC volume fraction, particles mean diameters have been evaluated for different C/O ratios and for different HAB.

3.2.1   SOOT AND NOC VOLUME FRACTIONS

By using the described calibration procedures, LIF and LII signals can be suitable for volume fraction measurements of NOC and soot particles.

At this purpose in next two figures the volume fractions of both the particles classes, NOC (Fig. 3.11) and soot (Fig. 3.12), are reported, as function of the equivalent ratio. NOC are detectable just above the stoichiometric value and its concentration increases with the equivalent ratio. Soot particles, instead, are practically absent in flames with equivalence ratios ranging from 1 up to 2, for these flames the incandescence signal of soot particles was not detectable. Thereafter, soot volume fraction quickly increases. In Figs. 3.12 and 3.13 the volume fraction of NOC and soot for two flames, $\Phi=1.76$ and $\Phi=2$, are reported as function of the height above the burner, (HAB). Only in correspondence of $\Phi=2$ soot is detectable, and its concentration increases at higher HAB. Moreover by comparison of the concentrations of gas-phase aromatics as predicted by flame modelling at the beginning of the flame it is reasonable to hypothesize that gas-phase aromatics are the only fluorescing species [76]. The PAHs fluorescence cross section has been evaluated in correspondence of the maximum PAHs concentration and has been considered constant above this point being the oxygen concentration negligible and the flame temperature approximately constant. The signal due to molecular particles can be therefore

obtained by subtracting from the measured fluorescence that attributable to PAHs. The fluorescence signal due to particles starts at larger residence times with respect to gas-phase aromatics and reaches a quite constant value at the end of the flame. It precedes the incandescence signal. As expected, the signal is higher for the richer flame.

Methane/oxygen combustion in laminar premixed condition, as expected, needs very fuel-rich condition in order to produce and therefore to emit soot particle, while NOC is formed also in less rich conditions in the premixed flames investigated and with a higher volume fractions respect to the soot particles.
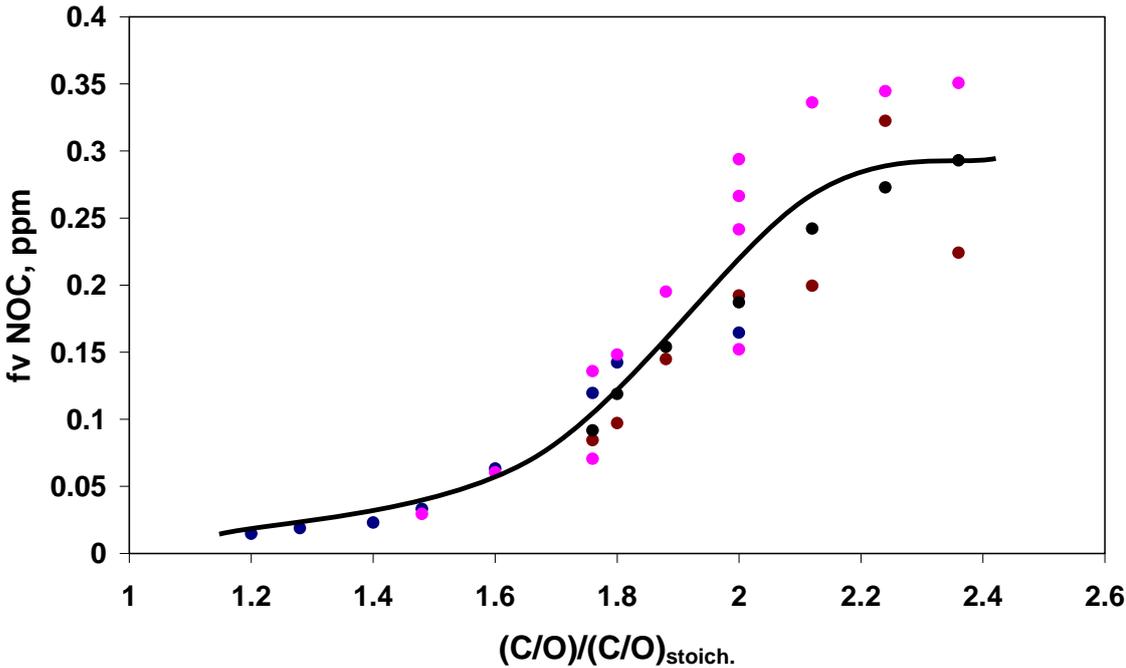
Fig. 3.11 NOC volume fraction at 10 mm HAB in laminar premixed methane/oxygen flames vs. the equivalence ratio: $\Phi = (C/O)/(C/O)_{stoich.}$
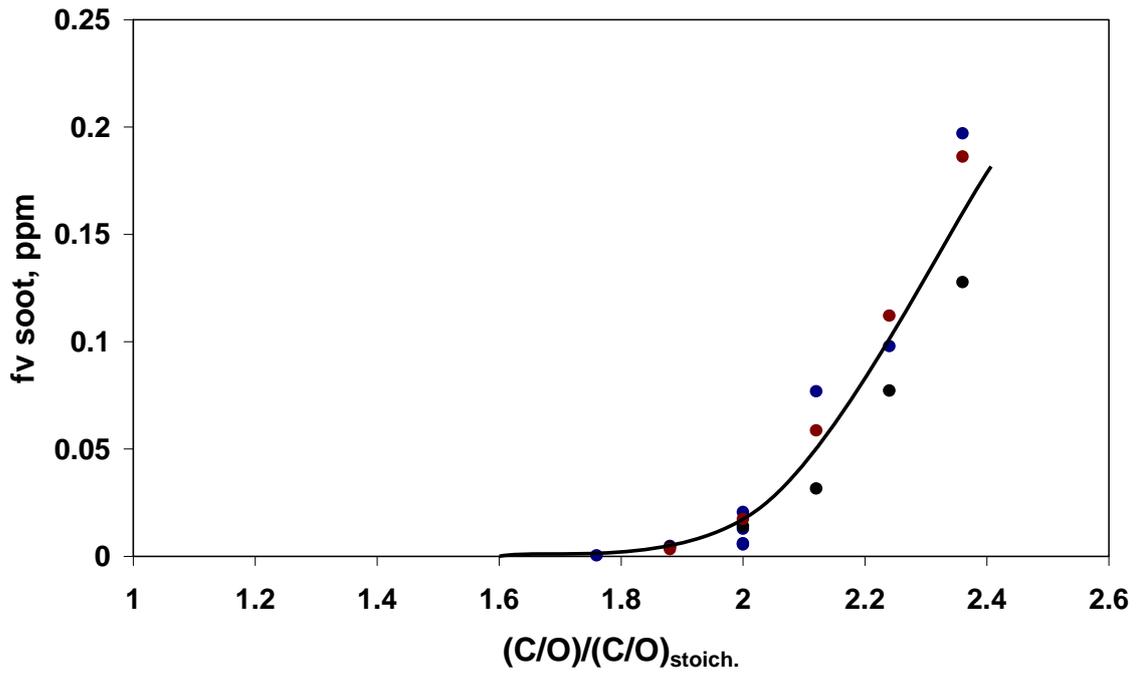
Fig. 3.12 Soot volume fraction at 10 mm HAB in laminar premixed methane/oxygen flames vs. the equivalence ratio: $\Phi=(C/O)/(C/O)_{stoich}$.
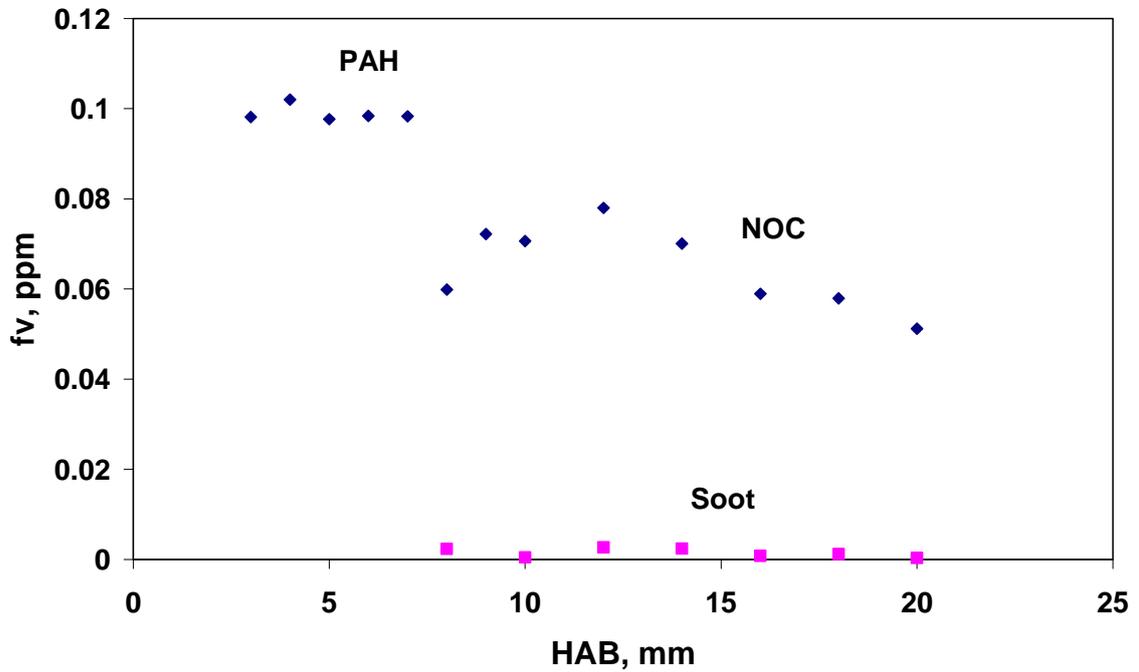
Fig. 3.13 Soot and NOC volume fraction at $\Phi = 1.76$ (C/O=0.44) vs. the HAB.
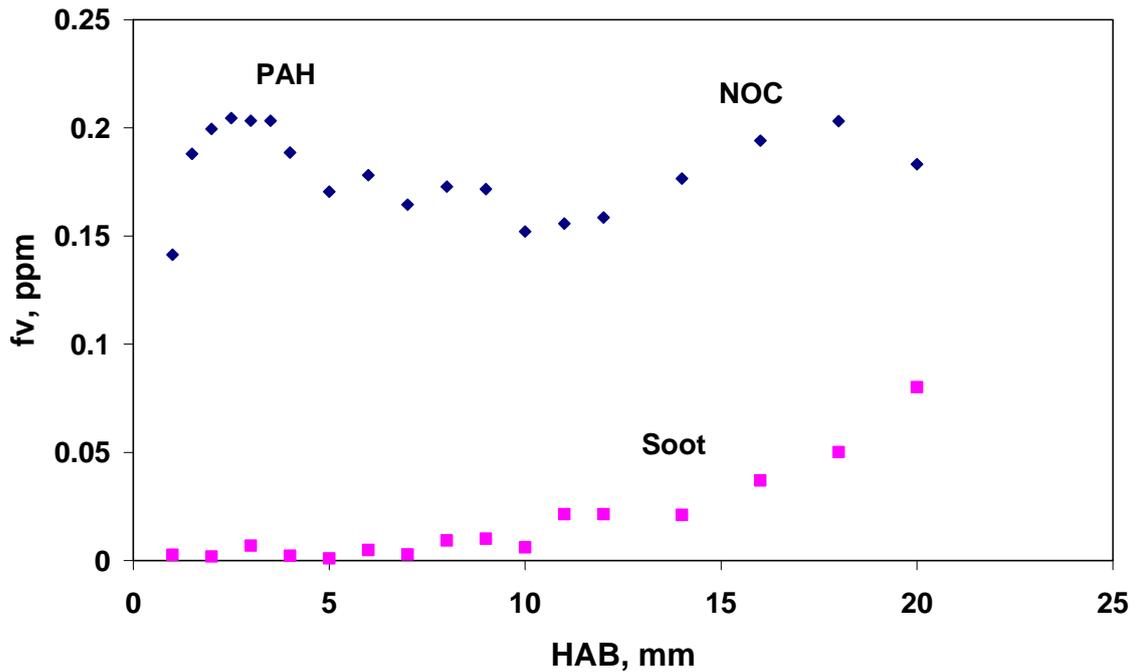
Fig. 3.14 Soot and NOC volume fraction at $\Phi = 2.00$ (C/O=0.50) vs. the HAB.

3.2.2 SOOT AND NOC MEAN DIAMETERS

In order to estimate the mean size of the particles, scattering measurements were performed in the same flame conditions. Figure 3.15 shows, the scattering profile measured by using the fifth harmonic (213 nm), for the flame with $\Phi=2$, at different HAB. On the same figure the estimated gas contribution is reported too. It is possible observe that the Qvv signal measured is larger than the gas one, also in flame zones where soot is absent and only NOC particles are present.

From the scattering coefficients, after subtraction of the gas contribution, and from the particles volume fraction, previously determined, the mean particles diameter, D_{63}, was estimated using the Rayleigh theory. Figure 3.16, shows, the mean particles size which is about 3 nm in a region of the flame where only NOC particles are present, and increases at higher HAB where soot begins to appear.
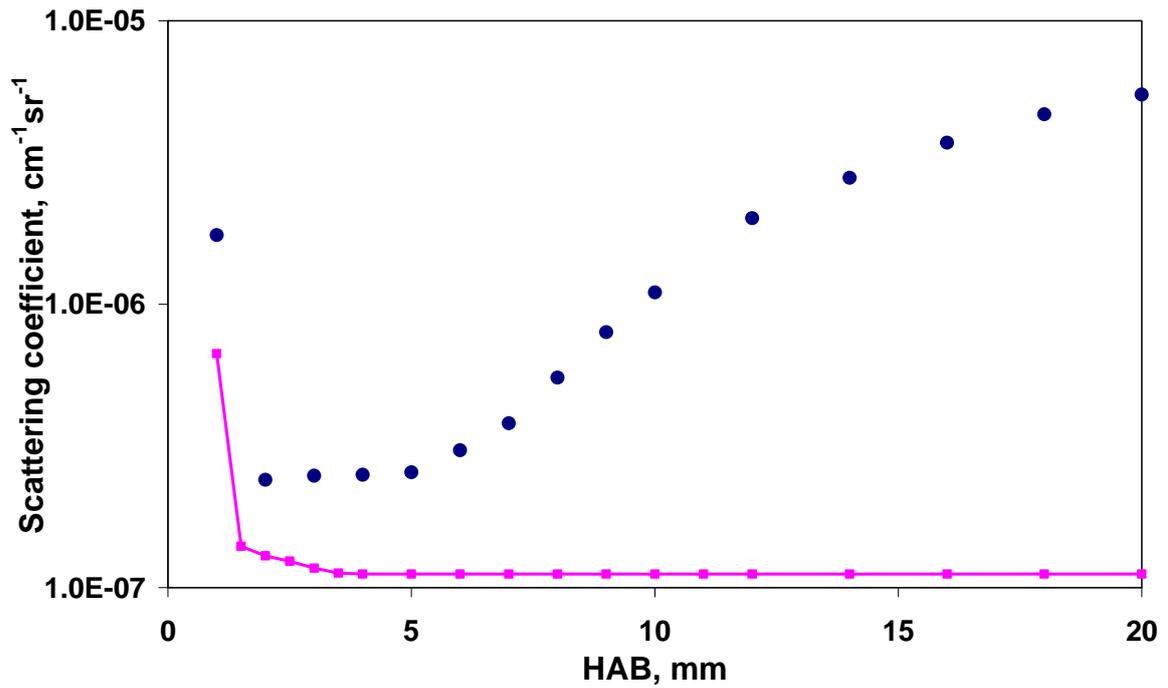
Fig. 3.15 Scattering coefficient measured in the laminar premixed flame with equivalent ratio 2 at different HAB.
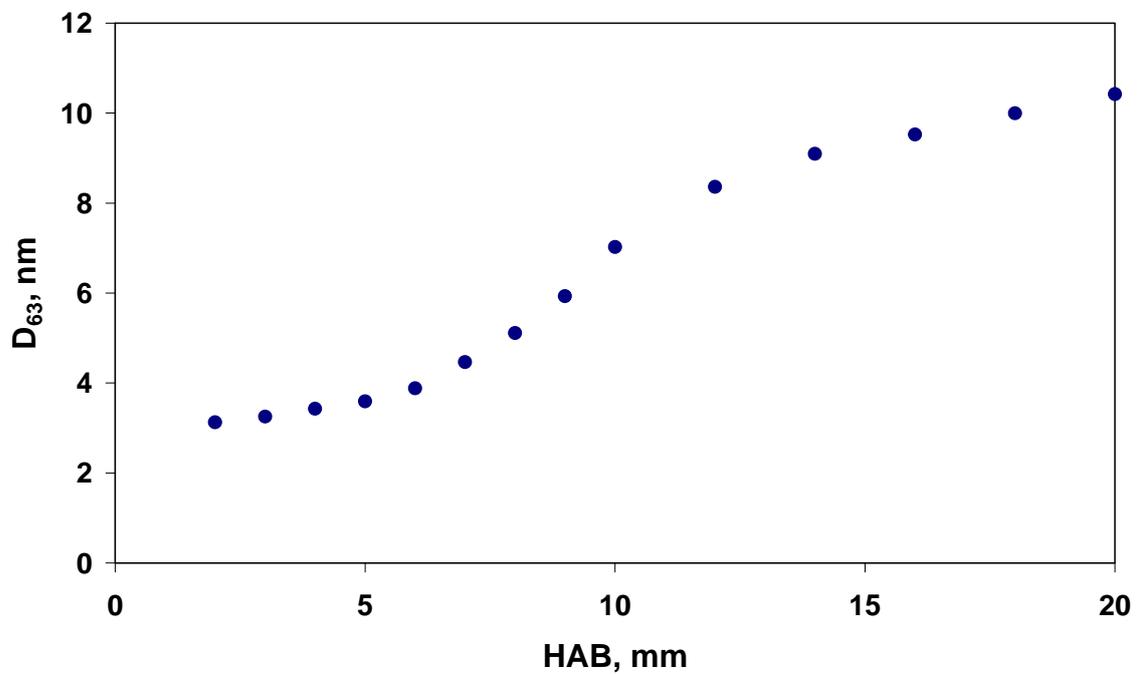
Fig. 3.16 Mean particles diameter estimated by using the Rayleigh theory in the laminar premixed flame with equivalent ratio 2 at different HAB.

3.3 LAMINAR PREMIXED BENZENE FLAMES

As previously observed, in addition to size, the main characteristic that allows distinction between precursor nanoparticles (NOC) and soot is the light absorption property. Soot particles absorb strongly in a large spectral region from the UV to the visible, whereas precursor nanoparticles are transparent to visible light. The transition from these two spectral behaviors seems to be too fast to be followed with the classical optical techniques in atmospheric pressure flames of ethylene. Indeed, Basile et al. [77] did not observe a gradual transformation of the optical properties of nanoparticles towards those of soot except by an abrupt change of the absorption characteristics associated with an increase in the size of the particles. In other words, the coagulation of precursor nanoparticles is associated with their aromatization or viceversa [77]. Aromatic fuel flames seem to follow different behaviors. Minutolo et al. showed that inception of soot particles consists in the progressive aromatization of initially "transparent" structures. Massive growth of soot particles takes place only after the aromatization has largely progressed [78].

The choice of benzene is because aromatic fuels are used in practical combustion systems and are more prone to soot formation than aliphatic fuels. Also for benzene flames the processes of fuel oxidation and pyrolysis overlap. Particle inception occurs in the main oxidation region, in a flame environment completely different to that encountered in the ethylene or methane flames where particles nucleate in the post-oxidation region of the flame [26].

On the basis of these observations, the transformation of precursor nanoparticles to soot may be controlled by different processes than in aliphatic flames and kinetic aspects could be more relevant than physical coagulation of the precursor nanoparticles.

A benzene/air flame with C/O ratio 0.72 at atmospheric pressure is stabilized on a porous bronze McKenna burner (6 mm diameter) with a stainless steel plate located 25 mm above the burner. Primary air is mixed with benzene by means of a two-stage saturator; the second stage is kept at

30°C and the first stage is 3°C higher. Further air is added after the second saturator to give the desired C/O ratio. The benzene-air mixture is fed at a constant cold gas flow velocity of 4.2 cm/s. Measurements are performed at different heights above the burner from 1 to 12 mm, every 0.5 mm.

Spectral absorption and laser induced fluorescence and incandescence measurements have been used to detect combustion-formed aromatic compounds and soot in a slightly sooting atmospheric premixed benzene flame. Light absorption coupled to in-situ light scattering measurements and ex-situ Atomic Force Microscopy also allowed the evaluation of particle sizes.

Atomic Force Measurements have been performed on the material collected on mica substrates by thermophoretic deposition. The sampling system is realized by a special-purpose holder mounted over the piston extension of a double acting pneumatic cylinder, which assures a constant sampling time of about 20 ms. Mica disks, 9.9 mm diameter and about 0.25 mm thickness are used. The easy cleavage and negligible roughness of mica make it an ideal substrate for AFM applications. AFM is based on the attractive or repulsive interaction forces between a tip placed at the extremity of an elastic beam (cantilever) and the surface of the sample. The tip, ideally ending with a single atom, is made of a hard and non-conducting material. Topological three-dimensional images of the deposited particles are obtained with a resolution of about 1–2 nm for x and y axes by scanning the surface of the samples. The resolution on the z axis is much higher, below 1 Å in low-noise conditions. In our measurements, AFM is used in the tapping-mode procedure to minimize unwanted effects of the interactions due to direct contact, basically convolution, plastic deformation, and displacement of the sample by the tip. Details of the experimental procedure can be found in literature by Barone et al. [33].

Extinction and laser induced fluorescence spectra are measured along the axis of the flame. Close to the burner exit, there is strong interference of mono-ring aromatics, benzene molecule and its intermediate oxidized species, with the spectroscopic signatures of combustion-formed compounds. The contribution of mono-ring aromatics to the measured signals is estimated from their concentration by kinetic modelling of the flame [17] and by the extinction and fluorescence spectra measured in the first flame location at 1 mm above the burner where the contribution of mono-ring aromatics to the detected spectra is dominant.

The slightly-sooting benzene flame with C/O=0.72 shows three characteristic flame zones. The first location in the flame (2 mm) is well below the maximum flame temperature (maximum temperature is about 1750 K at 3-4 mm) and is in the main oxidation region. Here, both extinction and fluorescence spectra show the typical signature of mono-ring aromatic molecules. Two absorption bands, the first at 205 nm and the second broader one at 250 nm are characteristics of the extinction spectrum while the scattering at 266 nm and a broadband emission peak at around 290 nm are the most prominent feature in the fluorescence spectrum. After subtracting the contribution of mono-ring aromatics from both extinction and fluorescence, the extinction coefficient does not presents peaks typical of PAHs but it sharply decreases from 200 nm to about 350 nm where it becomes negligible. A broadband emission peak around 310 nm becomes the most prominent feature of the fluorescence spectrum.

Figure 3.17 shows the extinction and fluorescence spectra in excess of mono-ring aromatic contribution measure at different heights above the burner.

The second location examined is across the maximum temperature region of the flame at 5 mm. The extinction spectrum detected in this region exhibits a very rapid fall-off around 200 nm followed by a more gradual decrease at longer wavelengths where extinction is measurable up to 400 nm. The fluorescence spectrum shows two broad emission bands; the first one peaks around 310 nm, and a second broader one around 450 nm. Both spectral behaviors seem to indicate an aromatization process of the compounds formed in the main oxidation region. Indeed the

fluorescence peak in the near UV-visible region of the spectrum has been previously attributed to aromatic functionalities with two-rings formed within the flame while the emission in the visible at 450 nm has been attributed to three or more ring aromatics [22].

The third flame location is in the post-oxidation zone of the flame at 10 mm. The extinction spectrum extends down toward the infrared and exhibits a stronger absorption between 250 and 500 nm, typical of soot particles, whereas in the fluorescence spectrum the peak at 450nm is the most prominent feature.

Monochromatic extinction coefficients measured at 266 nm and 400 nm are reported in Fig.3.18. The extinction coefficient at 266 nm detected in the flame zone below 3 mm is very high and decreases by more than one order of magnitude with increasing height up to about 5 mm.
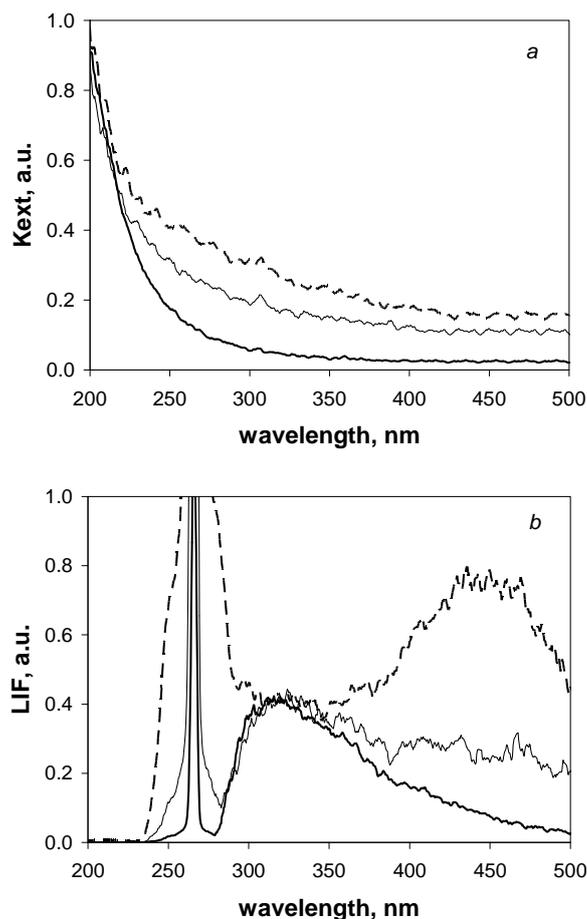
Fig. 3.17 Normalized extinction (a) and fluorescence (b) spectra in excess of mono-ring aromatic contribution measured at 2mm (heavy line), 5mm (light line) and 10mm (dashed line) from the burner in the C/O=0.72 benzene-air flame.

Thereafter it increases by less than a factor of two moving downstream. The rapid decrease of the extinction coefficient at 266 nm in the flame zone has to be attributed to the consumption of benzene. However, starting from 2 mm above the burner extinction in excess of mono-ring aromatics is detected, which rises rapidly up to about 3 mm and then slightly increases.

The extinction coefficient at 400 nm is very low in the flame zone and increases rapidly moving across the maximum temperature zone and then remains almost constant. In the same figure the laser induced incandescence signal measured at 550 nm is reported. Incandescence is due to thermal emission from particles which are heated-up by absorbing laser light and this is typical of mature soot particles [57].
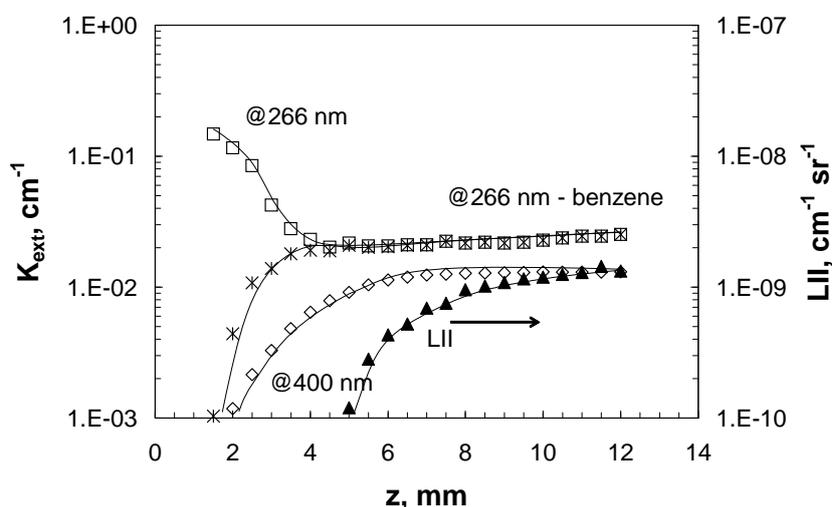
Fig. 3.18 Monochromatic extinction coefficients at 266nm (□) and 400nm (◊) as a function of the flame height in benzene-air flame at C/O=0.72. Also reported the extinction coefficients at 266nm in excess of mono-ring aromatic contribution (*) and the LII signal (▲).

The axial profile of the incandescence signal is delayed relative to absorption at 400 nm indicating that visible absorption at 400 nm is not only due to soot particles but also to other compounds present in the flame before soot formation.

In the flame region where a lack of incandescence is detected, the scattering signal shows values in excess to the gas-phase contribution. The evaluated excess scattering increases sharply at 2 mm and then remains quite constant up to 4 mm. This behavior is shown in Fig.3.19 where the

scattering coefficients measured in the flame are reported together with the estimated contribution of gas-phase compounds and the calculated scattering in excess to gas-phase compounds.

The region between 2 and 4 mm is characterized by species absorbing in the spectral range from the UV to 400 nm; these species precede incandescent particle formation and have a size of about 5 nm.

This size is estimated by scattering and extinction measurements from the optical properties of soot nanoparticles detected in ethylene flames and confirmed by AFM performed at 5 mm in the flame.
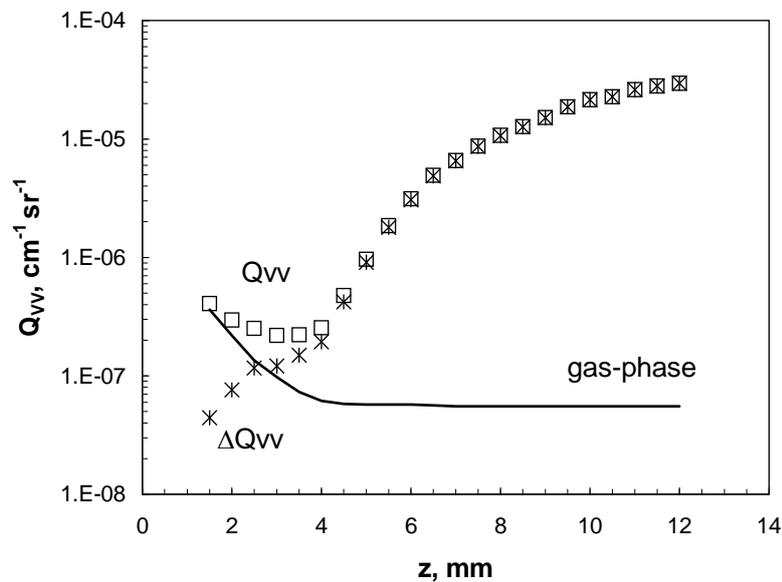
Fig. 3.19 Elastic scattering coefficients QVV at 266nm (□), gas-phase contribution to the scattering (heavy line) and excess scattering ΔQVV (*) along the axis of the C/O=0.72 benzene-air flame.

AFM shows a broad size distribution with a maximum at about 3.5 nm which extends from 1.5 to 6 nm (Fig.3.20).
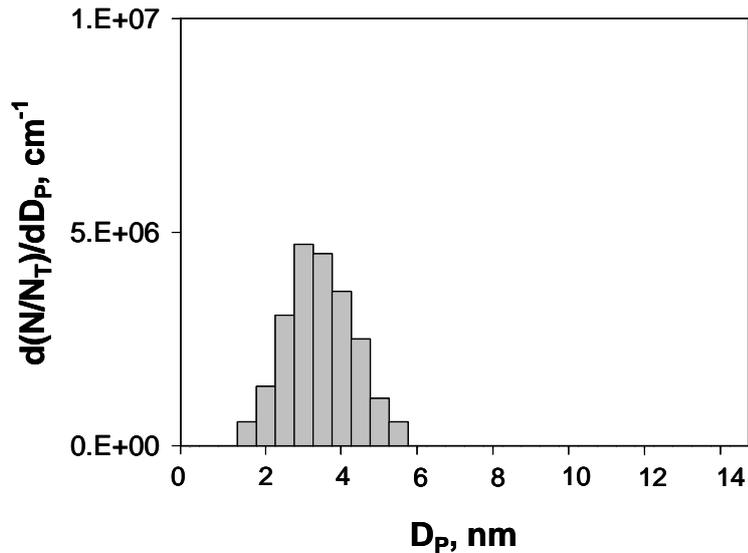
Fig. 3.20 AFM normalized size distribution curve of particles sampled at z=5mm.

The mean size calculated from AFM size distribution function is in close agreement with that obtained from scattering/extinction measurements.

Concluding, the main results of this study of benzene combustion are:

- high molecular mass structures with typical sizes of 3-4 nm are formed in the main oxidation region of the flame.

- the higher concentration of nanoparticles in the C/O=0.72 flame and the radical-rich flame environment in which they are formed promote the dehydrogenation of nanoparticles increasing the level of their aromaticity. As a result, nanoparticles with typical sizes of about 5 nm, absorbing and fluorescing in the visible are formed in the slightly sooting flame.

- visible absorbing nanoparticles reach a maximum concentration just before the appearance of mature soot particles and they can be considered responsible for soot formation.

According to the experimental results, inception of soot particles in benzene flames consists in the progressive aromatization of initially "transparent" structures, followed by coagulation of visible absorbing nanoparticles to form soot. This picture is different to that found in aliphatic fuel flames where the aromatization process which precedes coagulation has never been observed.

CHAPTER 4

LAMINAR DIFFUSION FLAMES

4.1 LAMINAR DIFFUSION ETHYLENE FLAMES

After preliminary investigation of laminar premixed flames, that allowed us to validate the use of the diagnostic based on the fifth harmonic as laser source for laser induced emission spectroscopy in order to simultaneously characterize soot and NOC in combustion systems.

The second step has been focused on the study of laminar diffusion flame, firstly burning ethylene and subsequently burning methane. The importance of diffusion flames is due to the fact that they are more representative of real combustion environments. Moreover the potential of LIF and LII, high spatial resolution, respect to extinction measurements, that need a "light of sight", are much more evident in diffusion flames as previously reported in the paragraph 2.3.3.

4.1.1 LASER INDUCED EMISSION AND EXINCTION DATA

Based on the experience relative to the study of laminar premixed flames, temporally and spatially resolved LIF and LII measurements have been performed in a ethylene laminar diffusion flame previously investigated by Rolando et al. [42] using UV and visible extinction measurements to obtain information on nanoparticles and soot particles concentration. Typical LIF and LII was identical to those collected in premixed conditions and therefore very similar to those reported in Fig. 3.1.

4.1.2 SOOT AND NOC VOLUME FRACTIONS AND MEAN DIAMETERS

LIF and LII data measured at several heights within the flame have been then compared respectively with the NOC and the soot volume fraction estimated by extinction measurements [42]. (Fig. 3.21 – 3.27)
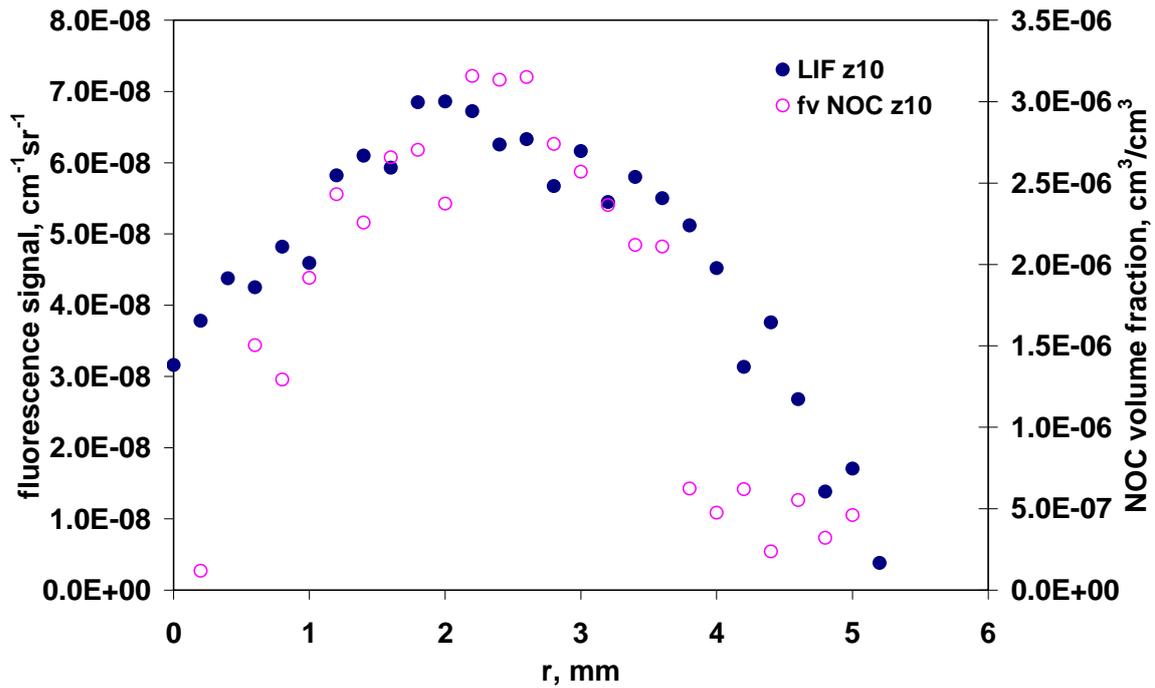
Fig. 3.21 LIF signals and NOC volume fraction at 10 mm as function of the radial position.
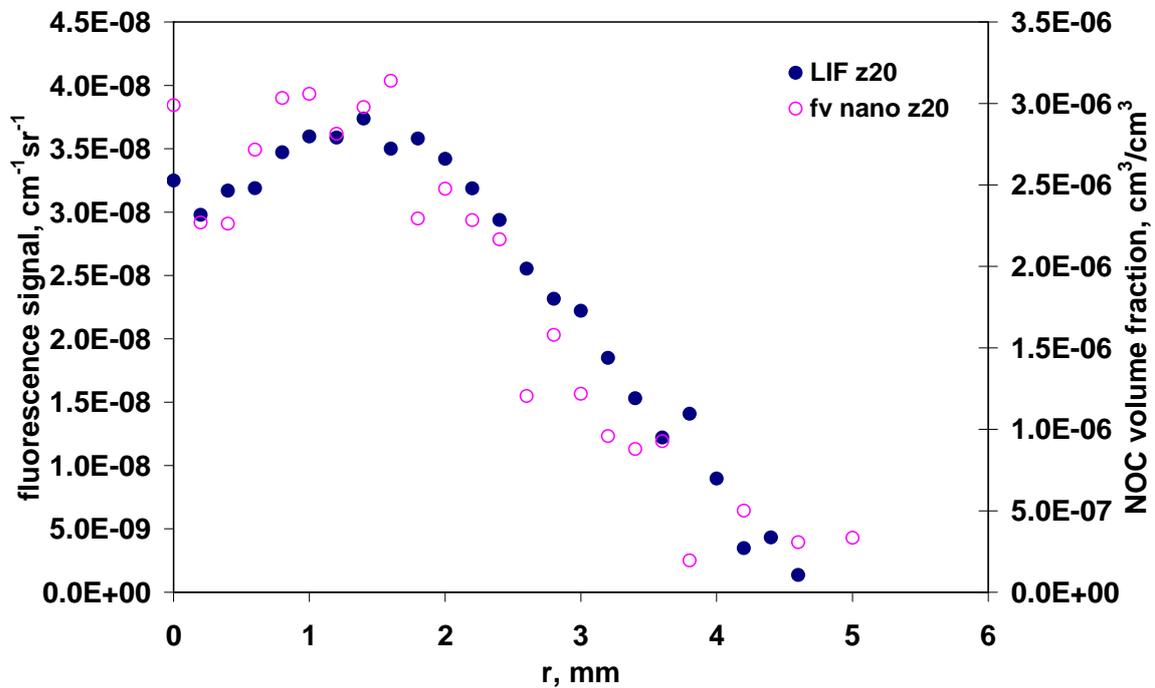
Fig. 3.22 LIF signals and NOC volume fraction at 20 mm as function of the radial position.
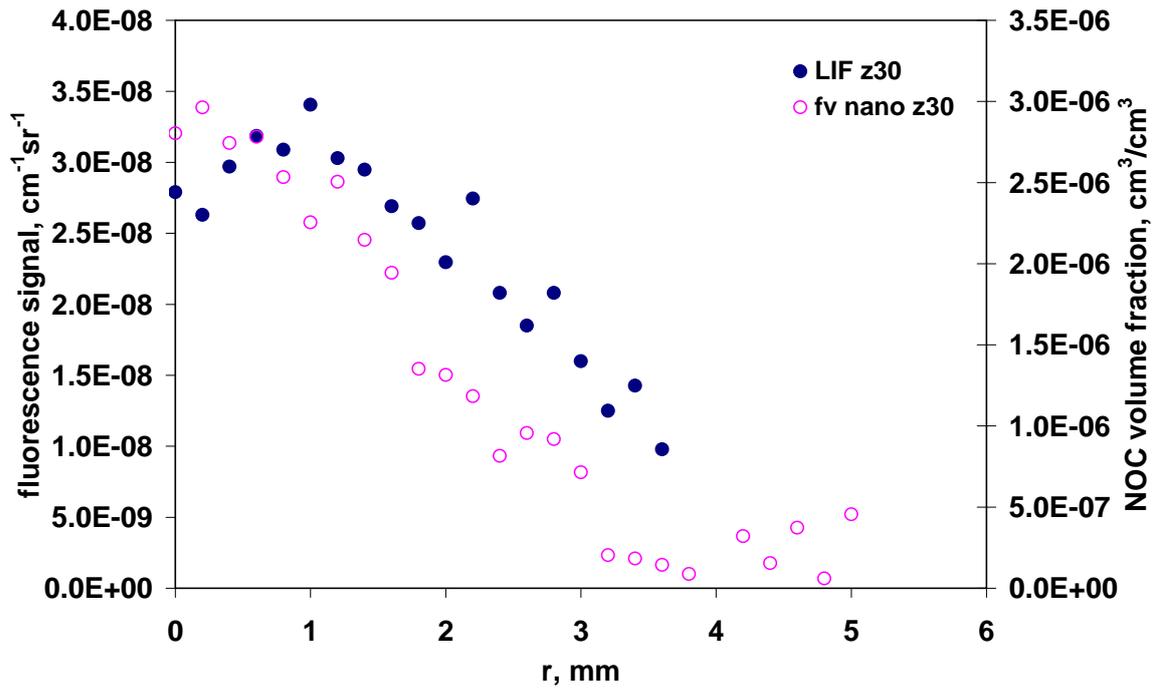
Fig. 3.22 LIF signals and NOC volume fraction at 30 mm as function of the radial position.
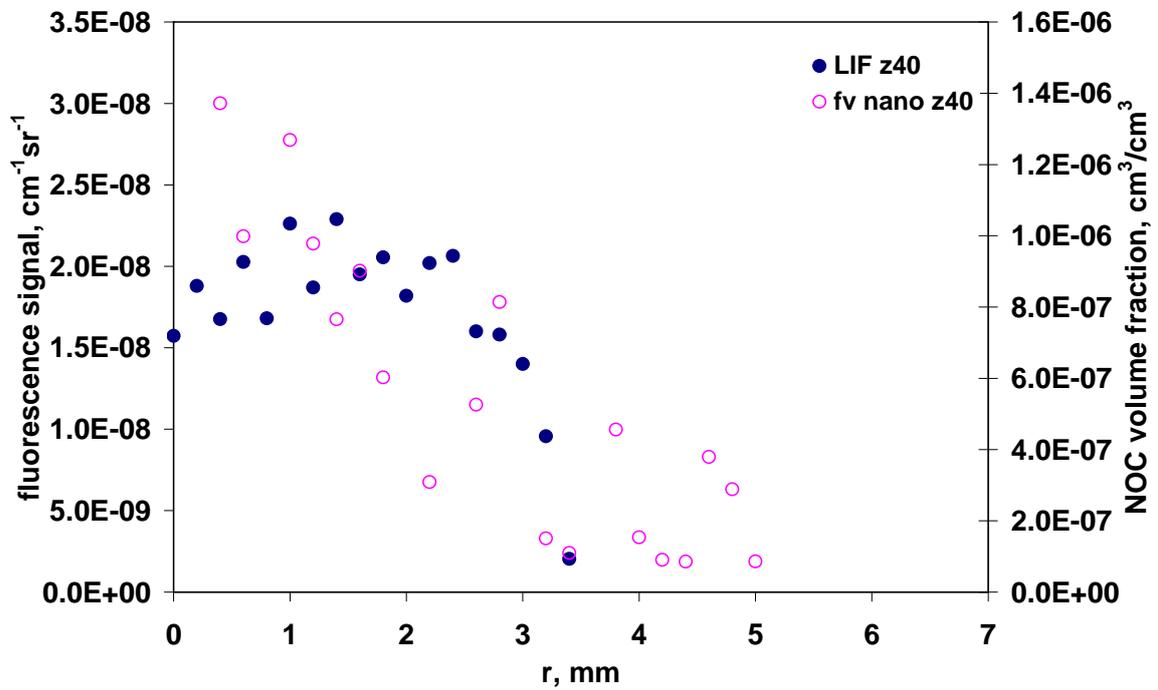
Fig. 3.23 LIF signals and NOC volume fraction at 40 mm as function of the radial position.
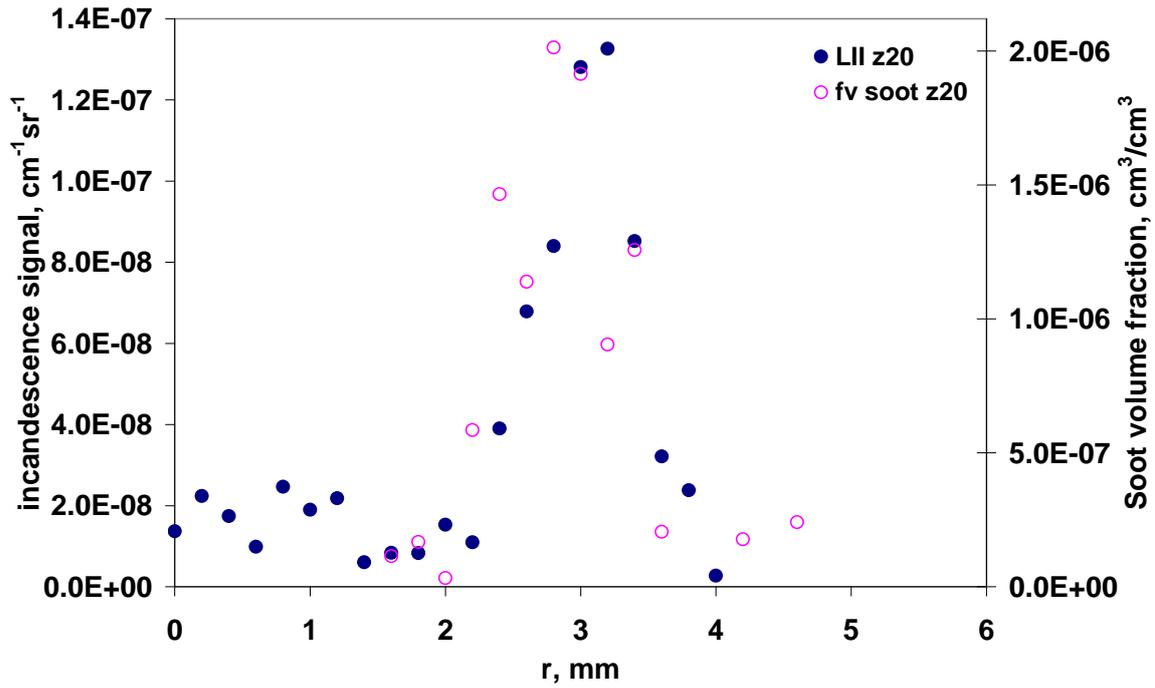
Fig. 3.24 LII signals and NOC volume fraction at 20 mm as function of the radial position.
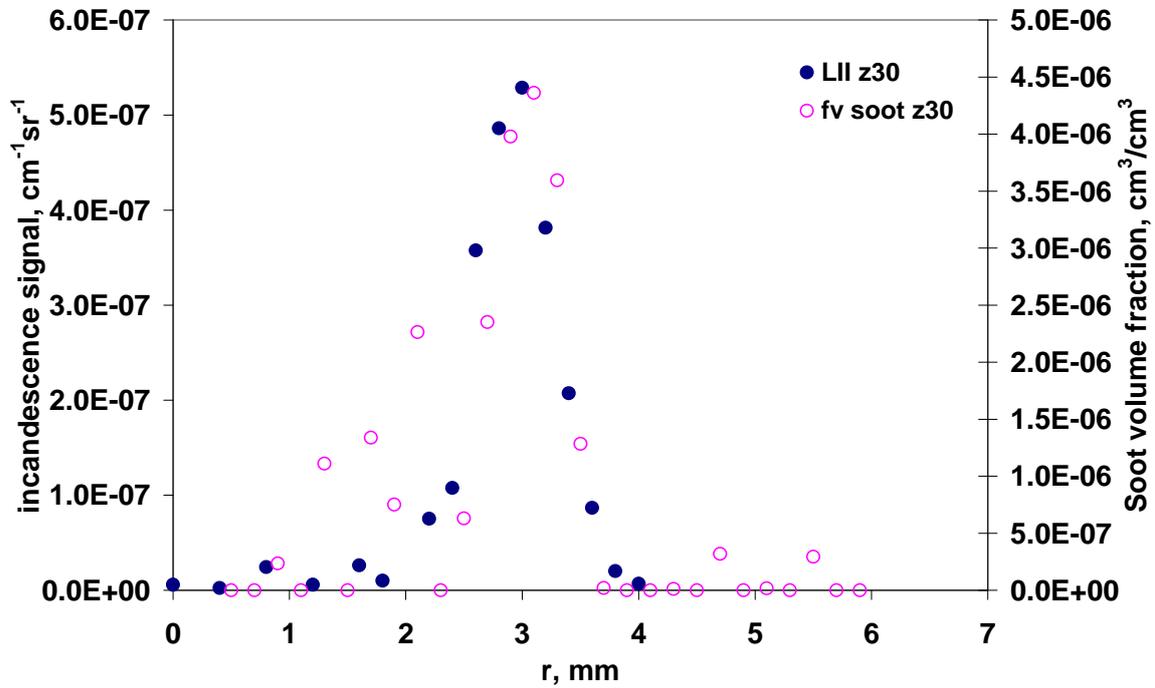
Fig. 3.25 LII signals and NOC volume fraction at 30 mm as function of the radial position.
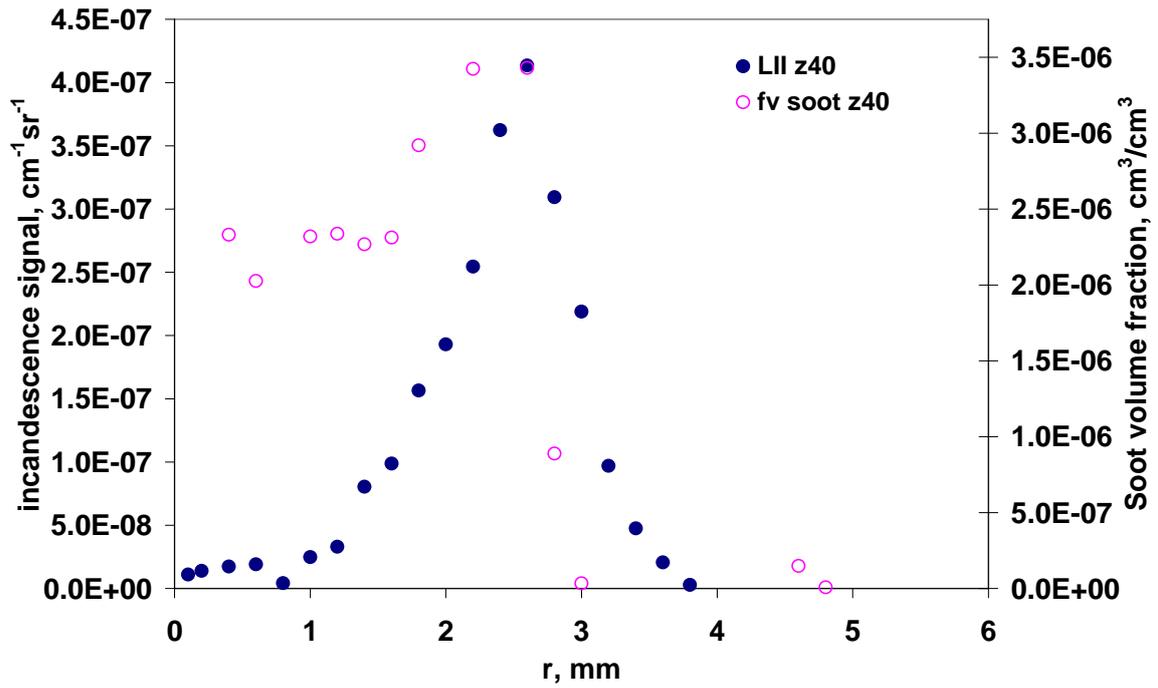
Fig. 3.26 LII signals and NOC volume fraction at 40 mm as function of the radial position.
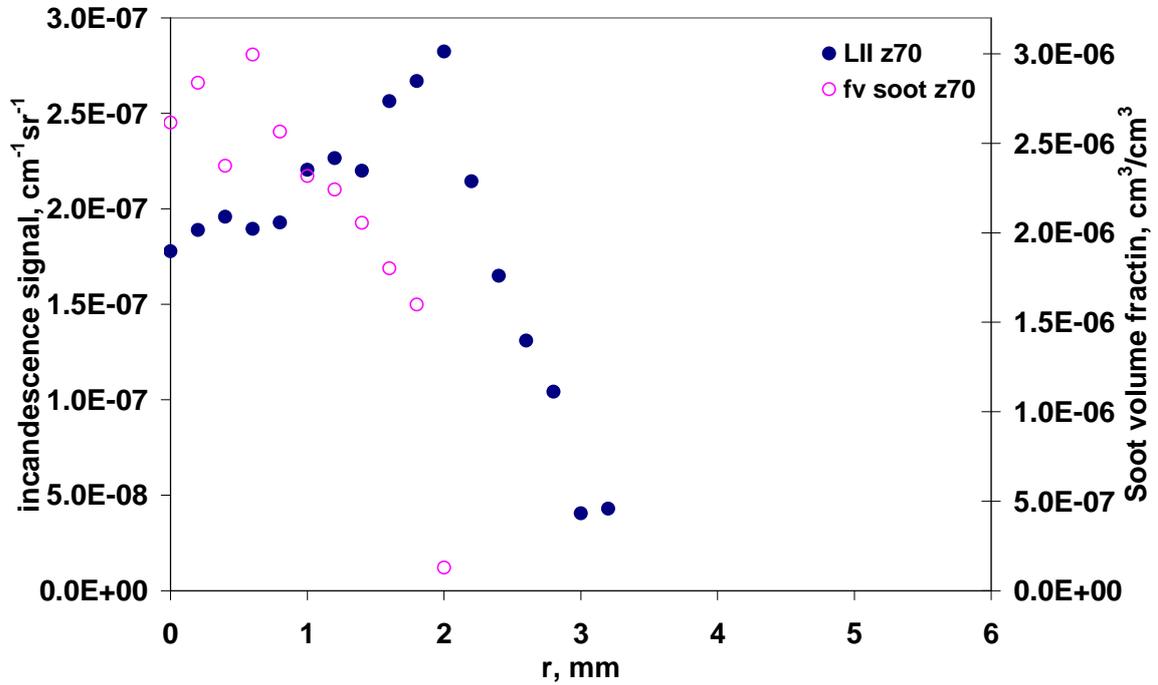
Fig. 3.27 LII signals and NOC volume fraction at 40 mm as function of the radial position.

Therefore, as obtained in premixed condition, ultraviolet fluorescence and visible incandescence correlate very well with the two particles classis, being as characteristic emission signals of the two particle classes.

However some uncertainties on the relative proportionality coefficient respect to the different flame locations and particularly respect to those obtained in premixed flames, raises some doubts about the calibration procedure, i.e. more accurate extinction correction, or on the effective nature of the signals in relationship to the different combustion systems.

To allow particles size evaluation scattering measurements have been performed in the flame, Fig. 3.28. Furthermore, after subtraction of the estimated by flame modelling gas contribution, and by using the Rayleigh formulation of the light scattering the mean particle size have been evaluated and reported in Fig. 3.29
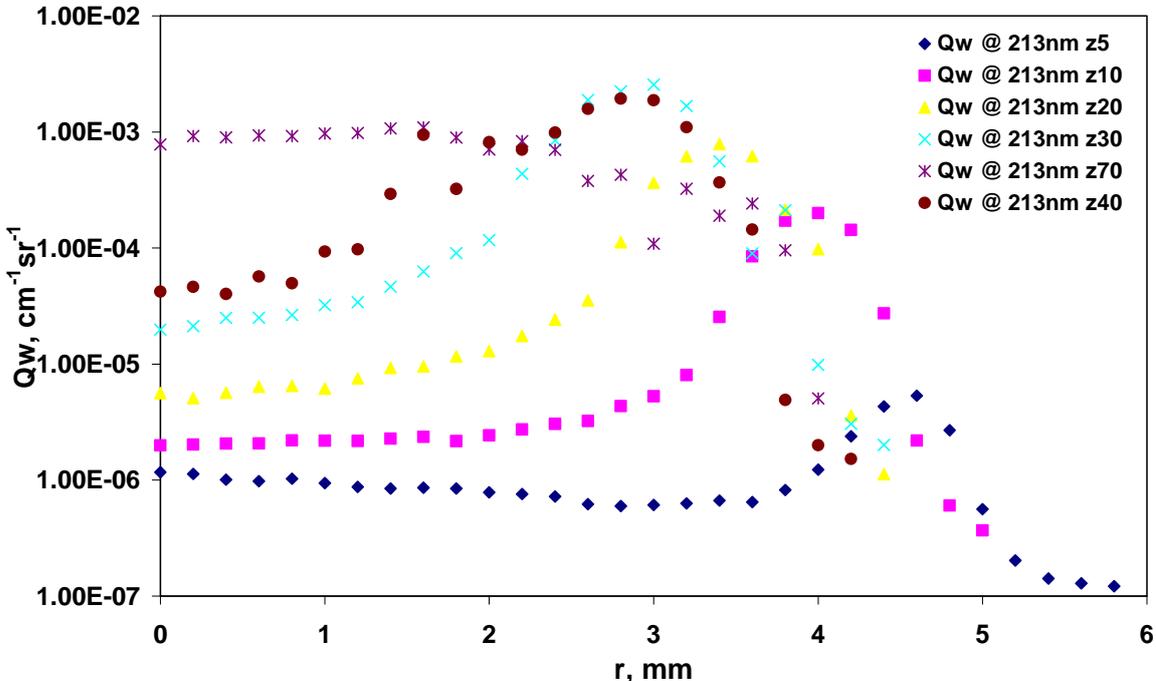
Fig. 3.28 Qvv by 213 nm vs. radial position.
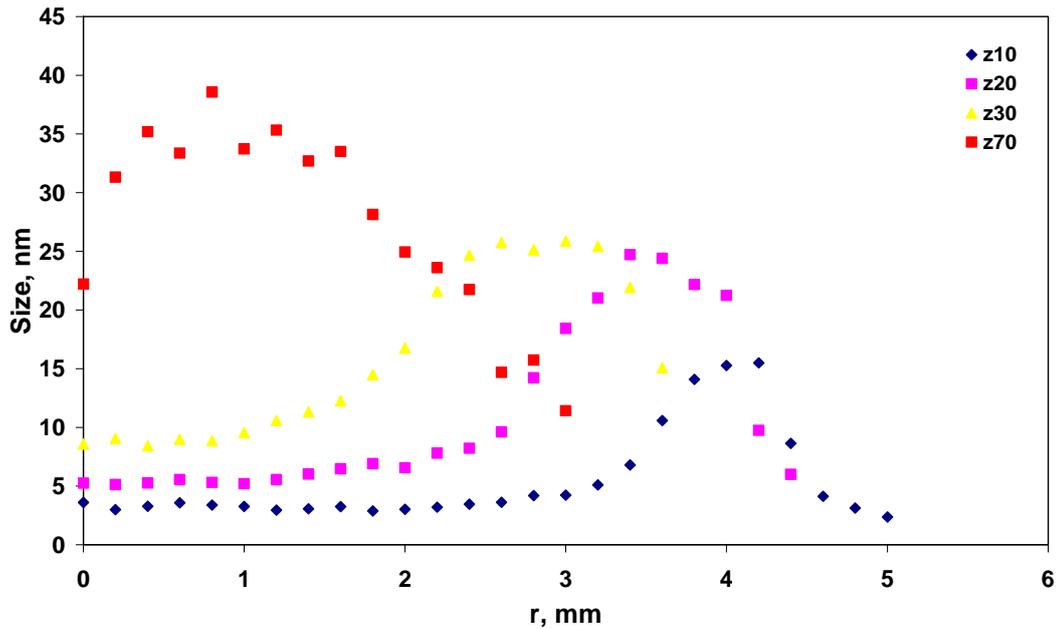
Fig. 3.29 Mean particle diameters by scattering measurements vs. radial position.

4.2 LAMINAR DIFFUSION METHANE FLAMES

A realistic comparison between ethylene and methane combustion, in terms of particulate formation, can not be attempted basing only on premixed combustion results. Therefore, in order to improve the actual knowledge on the effective particulate emissions by methane combustion, and to better understand the relative impact on NOC and soot of the two fuels, several measures of LIF and LII have been also performed in a methane laminar diffusion flame. The flame was the same previously investigated by Smooke et a. [79] by TPD measurements.

By previously calibrated LIF and LII measurements, NOC and soot concentrations have been evaluated in the methane flame, Fig. 3.30 – 3.31. As in the case of the ethylene flame, in methane flame soot formation is located in a narrow annular region closer to the maximum temperature zone, and its maximum volume fraction is measured just after the decrease of organic carbon particle volume fraction. The radial position of the maximum soot volume fraction shifts, at increasing heights, towards the centreline NOC are preferentially formed in the lower part of the flame and closer to the flame axis. The maximum volume fraction of organic

carbon particles decreases at increasing heights in the flame shifting toward the centreline. It becomes negligible at the flame tip.
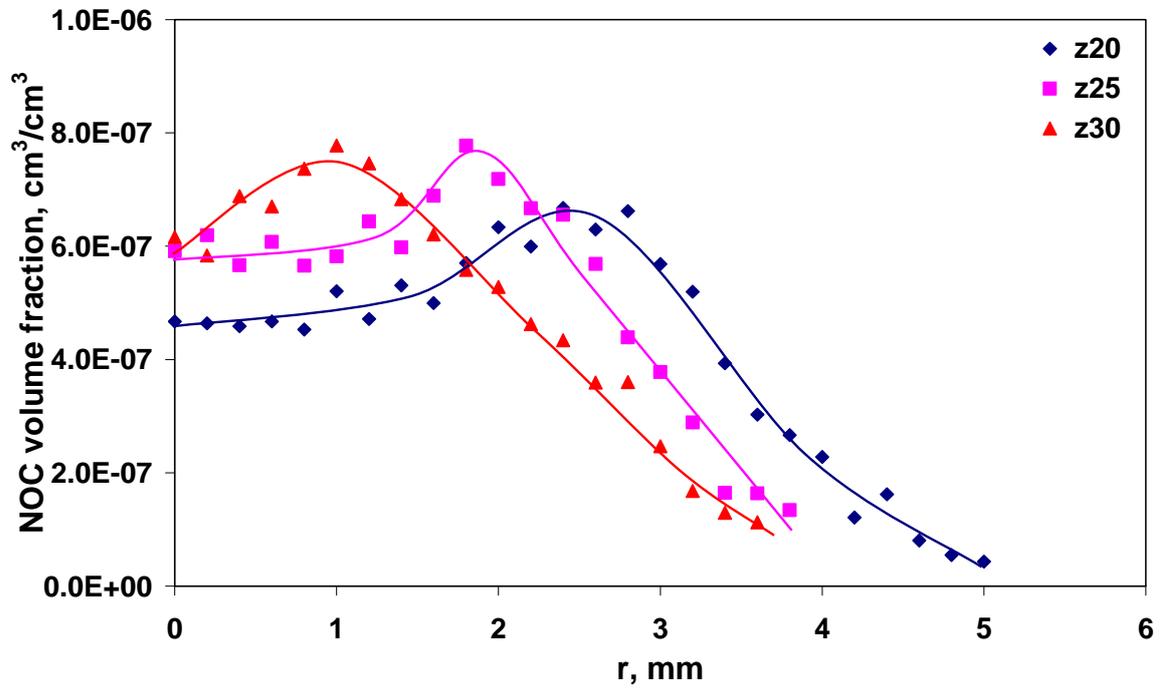
Fig. 3.30 NOC volume fraction in the methane laminar diffusion flame by calibrated LIF signals.
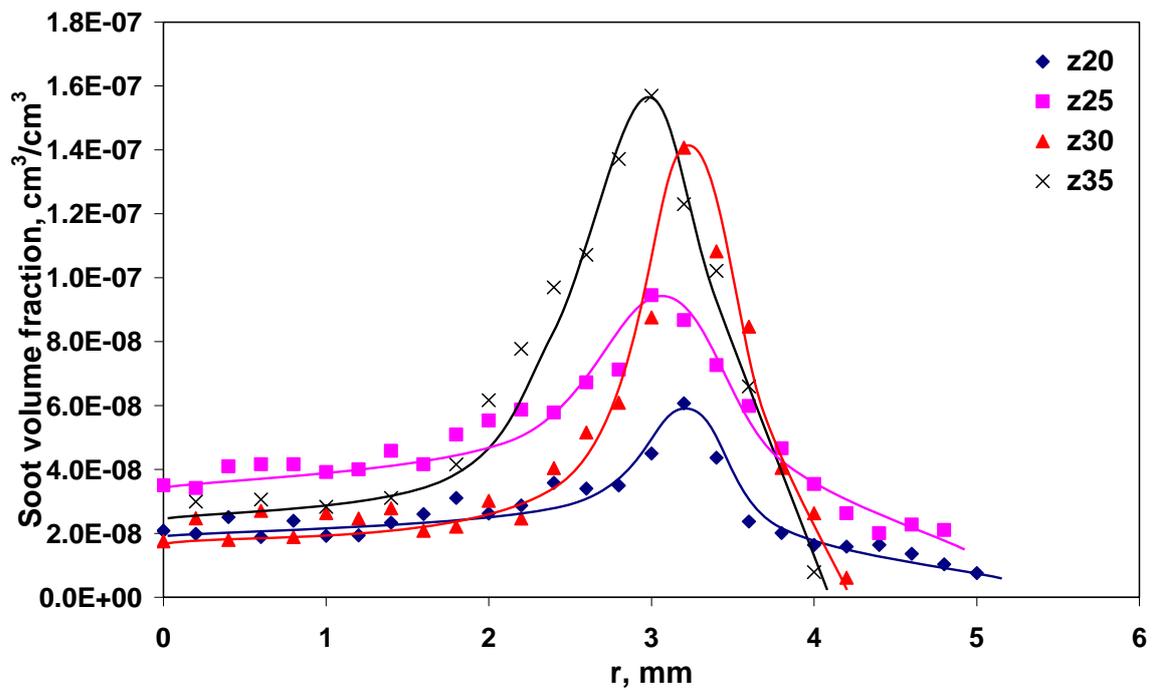
Fig. 3.31 Soot volume fraction in the methane laminar diffusion flame by calibrated LIF signals.

4.2.1 SOOT AND NOC VOLUME FRACTIONS AND MEAN DIAMETERS

These results are confirmed by the profiles of light scattering reported in Fig. 3.32, in which a strong signal is measured in correspondence to the presence of soot particles, but a relevant signal is also measured in the centreline where only NOC particles are present. From the scattering data, after evaluation of gas contribution, and the total volume fraction of the particles we obtained a rough estimate of the D_{63} of the total particles distribution function which is reported in Fig. 3.33. The particles mean size has been evaluated using the Rayleigh equation for light scattering using the optical properties for NOC and soot reported in [75].

Close to the flame centreline where the concentration of soot is very low, the mean size of the particle is of the order of 2-3 nm whereas in the annular flame region where soot is formed the mean particle size is of the order of 10 nm. These results are in agreement with the previous findings in the ethylene flame and confirm the formation of NOC particles also in methane diffusion flames.
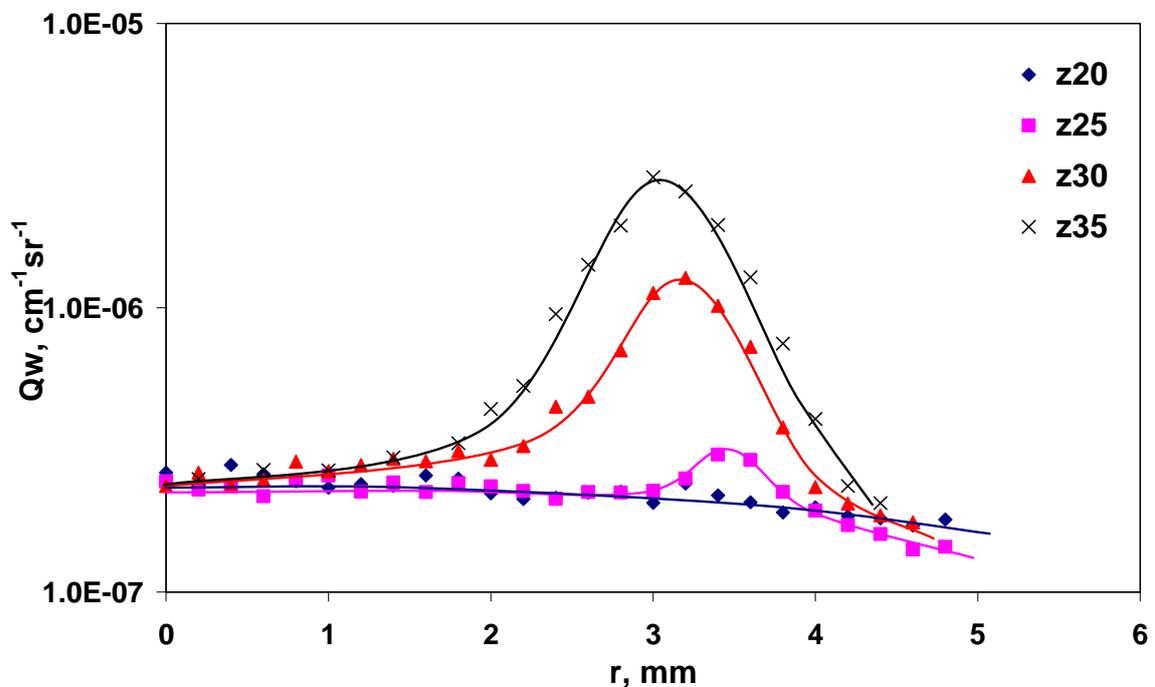
Fig. 3.32 Qvv by 213 nm vs. radial position.
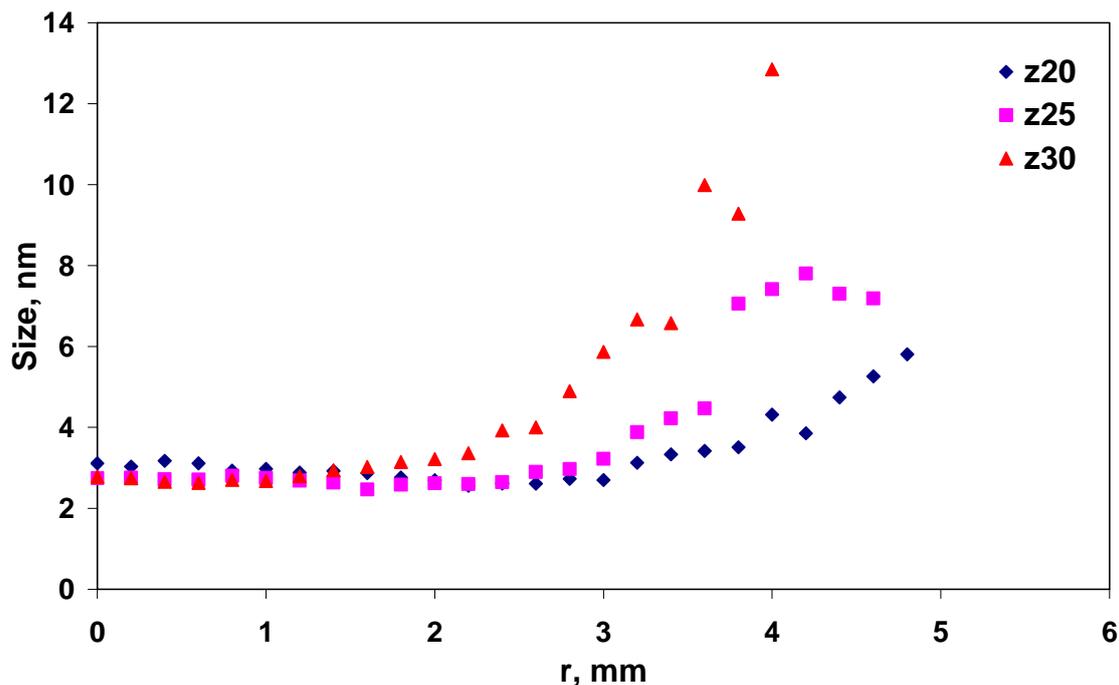
Fig. 3.33 Mean particle diameters by scattering measurements vs. radial position.

4.3 COMPARISON ETHYLENE AND METHANE

By comparing the volume fractions of NOC and soot for the two flames, ethylene and methane laminar diffusion flames, it is possible to observe that methane flame produces a lower amount of both NOC and soot but the reduction of soot was stronger than that of NOC. In particular, it is possible to observe that the ratio between the maximum value of soot to NOC concentration in the ethylene flame is about 1.0 while in the methane flame it is 0.2.

Therefore, concluding this section on laminar diffusion flames, we can say that the proposed spectroscopic measurements, coupled with scattering and extinction measurements, have allowed the evaluation of the concentrations of soot and NOC and their average sizes in two laminar diffusion flames of ethylene and methane. NOC are immediately formed at the beginning of both flames whereas soot is preferentially formed in the ethylene flame being practically negligible in

the methane flame. Scattering measurements have shown that, as in the ethylene flame, NOC produced in the methane flame have mean sizes of 2-3 nm and are formed in the region of the flame close to the centreline. While in the ethylene flame NOC are transformed to soot particles, in the methane flame, although formed in lower amounts, their concentration value remains unchanged along the flame axis and hence they might be emitted from the flame.

CHAPTER 5

TURBULENT DIFFUSION FLAMES

Following the same procedures bases on laser induced emission spectroscopy, turbulent diffusion flames of ethylene and methane have been characterized in term of particulate formation.

5.1 TURBULENT DIFFUSION ETHYLENE FLAMES

The vertical turbulent non-premixed ethylene flames conditions are the same as Kent and Honnery [80] flames A and B. The fuel issues from a 3 mm internal diameter nozzle into ambient air; flame A at 52 m/s and flame B at 22.4 m/s with roughly twice the residence time of flame A. The stoichiometric height for flame A is about 46 cm (X/D = 153) and for flame B about 39 cm (X/D = 130), the latter flame being more affected by buoyancy. Measurements are performed at different heights above the nozzle from 3 – 70 cm with a spatial resolution in the radial direction of 0.5 mm.

5.1.1   SOOT AND NOC VOLUME FRACTION AND MEAN DIAMETERS

Radial fluorescence and incandescence emission signals detected at various locations in Flame A and B are reported in Fig. 3.34 and Fig. 3.35, respectively. In both flames, LIF signals appear immediately after the nozzle (Figs.3.34 a, 3.35 a) in a region of the flames where LII signals are practically negligible (Figs. 3.34 b, 3.35 b). In Flame A the fluorescence signal increases with distance from the nozzle up to X/D=23 (Fig. 3.34 a) and then decreases with increasing flame height. At a fixed flame height, LIF increases from the flame centerline and reaches a peak in the radial position which firstly moves towards the outer flame zones up to X/D=23. Then it merges with the central region at increasing heights; it becomes negligible at the visible flame tip (X/D=161).

The first measurable LII signal is detected at about X/D=46 showing a peak value at r/R=6 (Fig.3.34 b). Increasing the flame height up to X/D=81, LII the signal increases and moves towards the outer flame region where the LIF signal decreases sharply to negligible values.

The maximum LII signal in the radial direction shifts, with increasing height, towards the flame centerline and merges with the central region at X/D=115. At higher axial locations, the LII signal is observed to decrease. The radial and axial distributions of the LII signals are in excellent agreement with the soot volume fractions reported by Kent and Honnery [80].
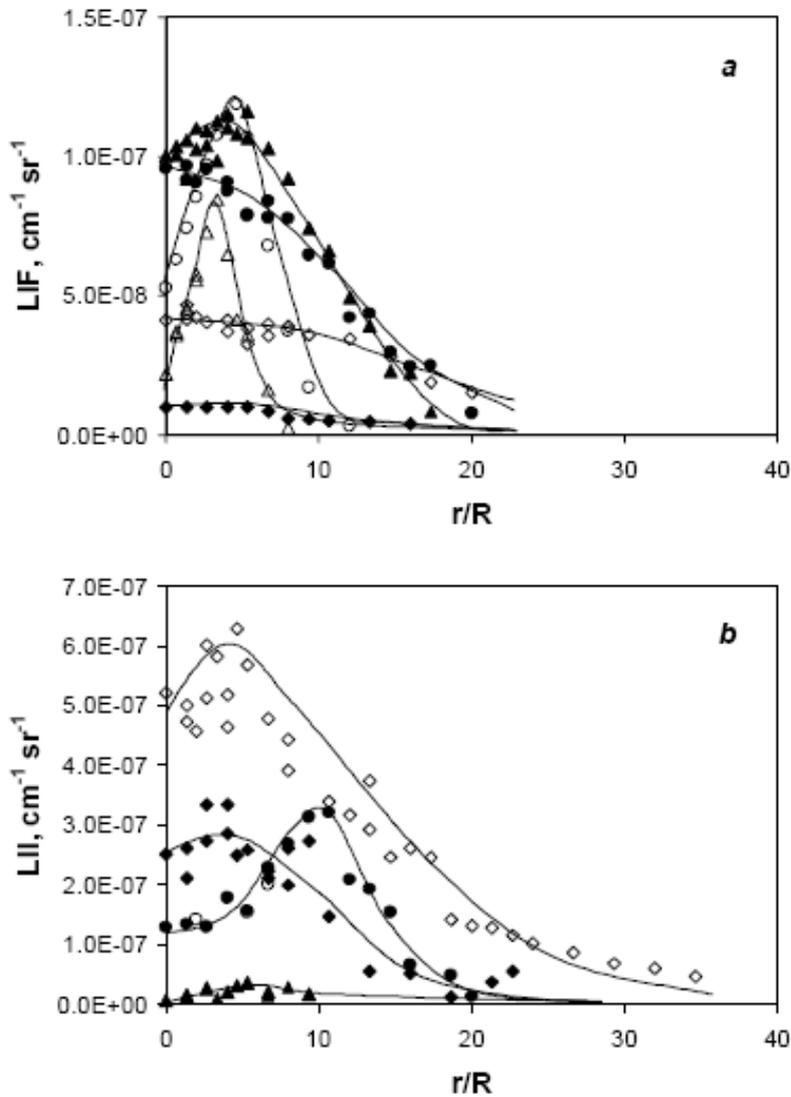
Fig. 3.34 Fluorescence (a) and incandescence (b) signals in Flame A. X/D=17; ○ X/D =23; ▲ X/D =46; ● X/D =81; ◊ X/D =115; ♦ X/D =161.

Quite the same behavior is shown by Flame B (Fig.3.35). Fluorescence emission is the dominant signal at the beginning of the flame and it is located essentially in a narrow region close to the flame axis. Incandescence appears at greater heights and it extends to the outer flame region. The intensity of the LIF signal is higher in Flame B than Flame A and it is detected in a narrower region close to the centerline.
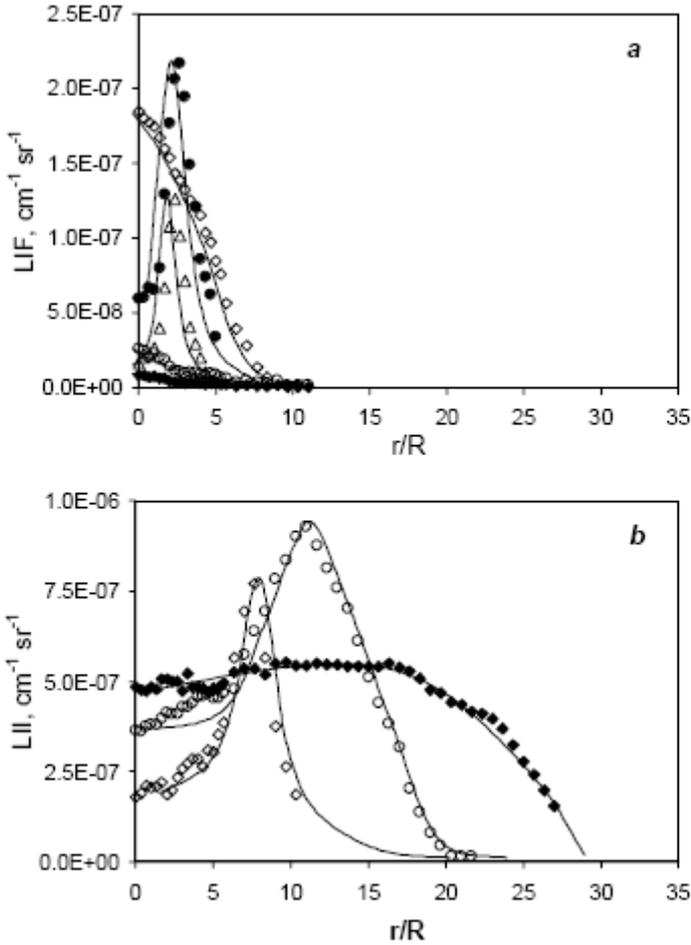
Fig.3.35 Fluorescence (top) and incandescence (bottom) signals in Flame B.
. X/D=10;● X/D =25; ◊ X/D =40; ○ X/D =70; ♦ X/D =100.

Scattering measurements at 213 nm are made at selected flame heights. Figure 3.36 reports the scattering cross section (Q_{VV}) measured at X/D=23 (Fig.3.36a) and X/D=115 (Fig.3.36b) in Flame A. In the same figure, the estimated scattering values due to gas-phase products (line in the figures) are also reported. The gas species scattering is evaluated from the scattering cross

sections of gaseous compounds at 213 nm at their concentrations and temperatures in the flames as estimated by numerical modeling.
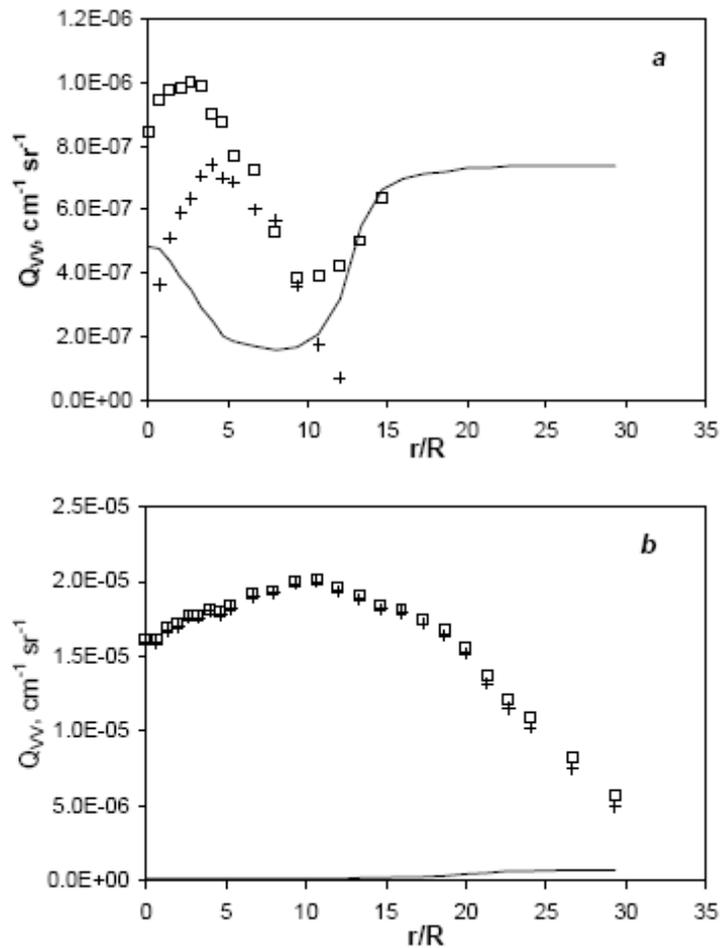
Fig. 3.36 Scattering in Flame A at X/D=23 (a) and X/D=115 (b). $\square$ QVV ; + QVV; __ gas-phase scattering.

At X/D=23, the scattering signal reaches a peak value at about r/R=4 (Fig.3.34 a). The scattering signal is of the same order of magnitude of the gas species scattering but it clearly exceeds this value; excess scattering (ΔQ_{VV}), also reported in the figure, peaks roughly in correspondence with the maximum fluorescence signal (Fig.3.34 a).

Scattering cross section increases by more than one order of magnitude from X/D=23 to X/D=115 (Fig.3.36 b) and in this case it is much higher than the gas-species scattering. At this flame location, both LII and LIF signals are detected with a prevalence of incandescence of

particles over the fluorescence of molecular compounds. The same behavior is shown by Flame B (Fig.3.37). The first flame location (X/D=10) is characterized by the complete absence of incandescence signal and the presence of a LIF signal which maximizes at r/R=2.7 (Fig.3.35 a). The measured scattering signal is quite low; it has a maximum value at the flame centerline and decreases moving towards the outer flame zones.
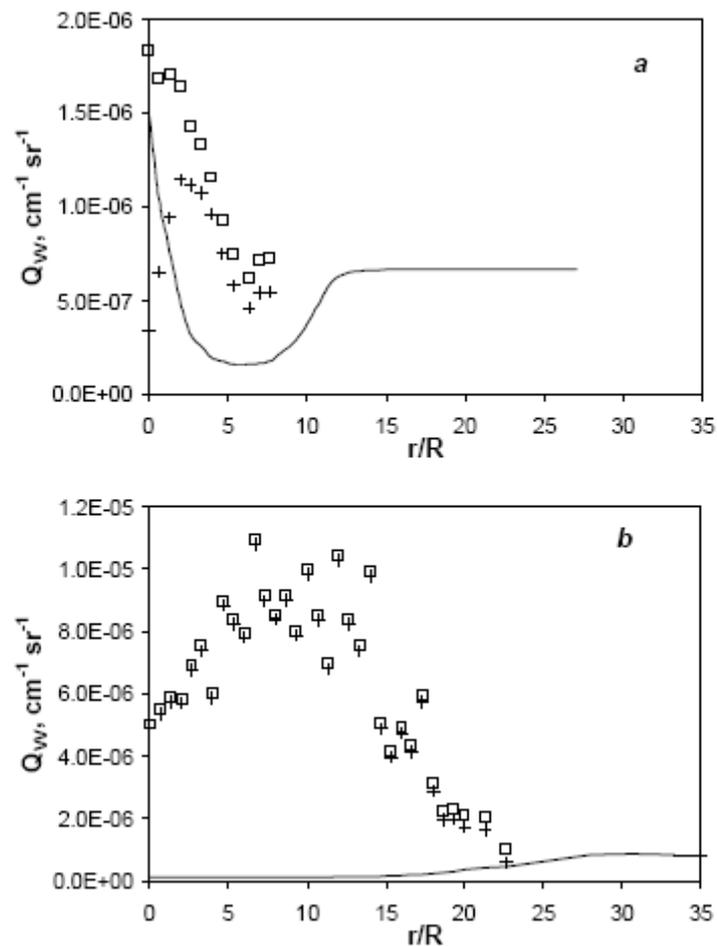
Fig. 3.37 Scattering in Flame B at X/D=10 (a) and X/D=100 (b). $\cdot$ QVV ; + QVV; __ gasphase scattering.

The estimated contribution of gaseous compounds to the scattering is of the same order of magnitude of the measured scattering signal at the flame centerline but decreases by one order of magnitude at increasing radial locations. As a result, the excess scattering profile maximizes in correspondence with the maximum intensity of the LIF signal (Fig.3.37 a).

Radial scattering signals measured at the second location dominated by the LII signal are more than one order of magnitude higher than those measured closer to the nozzle and are much higher than the value of the estimated scattering of gaseous products reported in the figure as a line (Fig.3.37 b).

5.2   TURBULENT DIFFUSION METHANE FLAMES

A vertical turbulent non-premixed flame of methane has been obtained by flowing methane from a 2.5 mm internal diameter nozzle into ambient air with a fresh gas velocity of 24.4 m/s, corresponding to a Reynolds number of 3.5E6.

5.2.1   SOOT AND NOC VOLUME FRACTION AND MEAN DIAMETERS

Figure 3.38 reports NOC volume fractions, measured through ultraviolet LIF, at three heights from the nozzle: 7 cm, 10 cm and 20 cm, as a function of the radius.

At 7 cm, NOC maximum concentration is located at 2.5 mm from the flame axis with a value of 0.25 ppm. At 10 cm NOC shows also a maximum between 2.5 and 3 mm with quite the same value measured at 7cm (0.26 ppm). At 20 cm NOC volume fractions increase up to 0.36 ppm, in this case at the flame axis.

In the same flames we have also measured soot particle concentration by LII technique. Figure 3.39 reports soot concentrations at two heights above the nozzle, namely 10 and 20 cm vs. the radial positions. At 10 cm soot particles shows a maximum of about 0.015 ppm at 2 mm from the flame axis. At 20 cm, which approximately corresponds to the location of the maximum soot concentration, the profile shows a maximum at the center of the flame with a value of about 0.035 ppm.
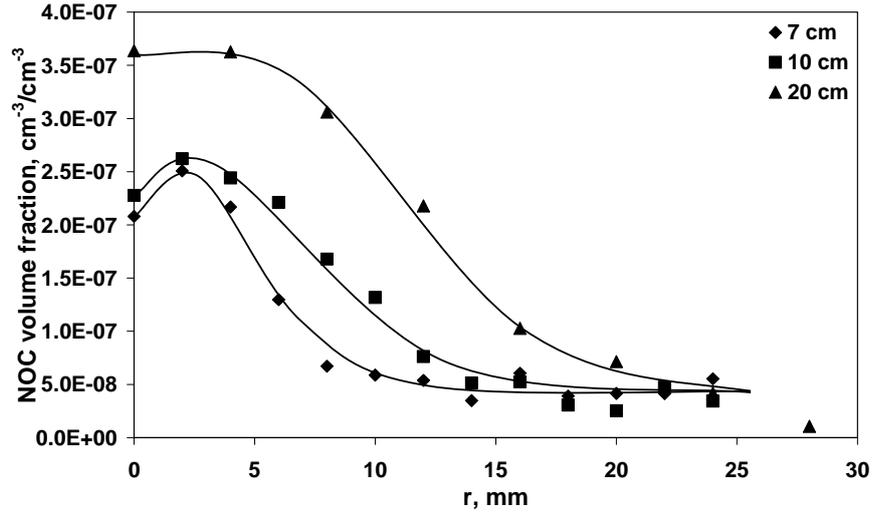
Fig. 3.38 Radial concentration profiles of NOC at three different flame heights
in the turbulent jet flame.
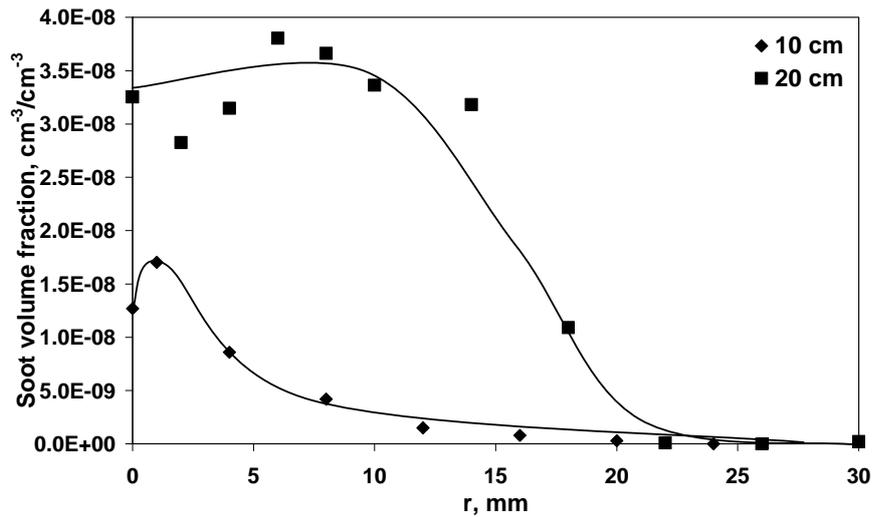
Fig. 3.39 Radial concentration profiles of soot at two different flame heights in
the turbulent jet flame.

From the laser induced emission measurements we can conclude that mainly particle with size

below the 10 nm are presents in methane flames. This is perhaps confirmed by the scattering

measurements performed on the same flames and reported in Fig.3.40 for the turbulent flame.
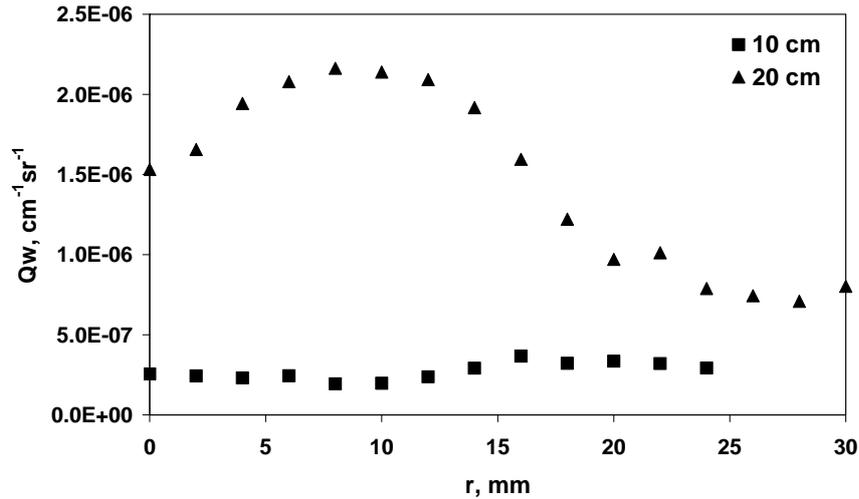
Fig. 3.40 Radial scattering profiles at two different flame heights in the turbulent jet flame.

Scattering coefficients increase by only one order of magnitude. In the ethylene flame the scattering increased generally of two or three orders of magnitude with the flame height. Therefore, also the scattering measurements show the presence of particles with very low sizes as shown in Fig.3.41 where the estimated mean sizes of the particles are shown.

In the early region of the flame, the scattering signal is of the same order of magnitude of that of gas-phase compounds exceeding this value of non more that 30%. It means that the aerosol formed in this region, as shows in Fig.3.41, is constituted of particles with sizes of the order of 3 nm. At higher heights along the flame axis, the scattering signal increases above the value of the gas-phase compounds indicating the presence particles with mean sizes in the range of 6 – 10 nm.
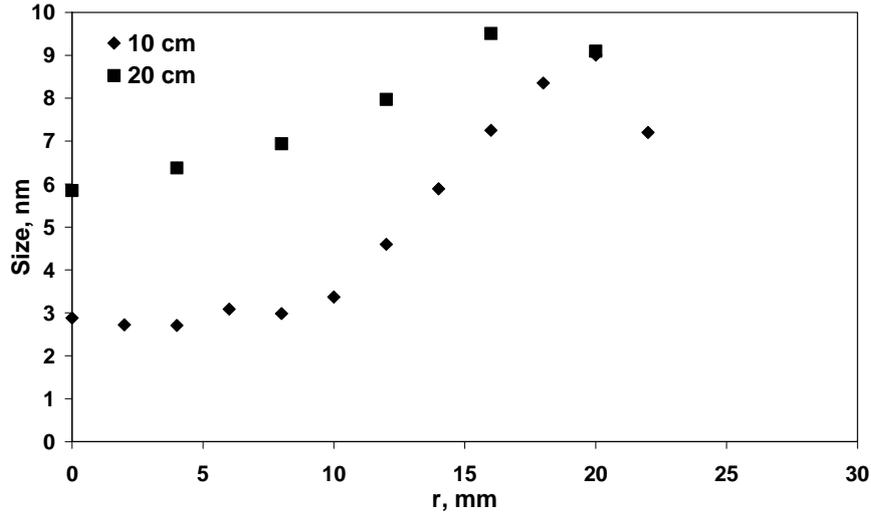
Fig. 3.41 Radial mean particle size at two different flame heights.

5.2.2   SIZE DISTRIBUITION FUNCTIONS MEASURED BY ON-LINE SMPS

Differential Mobility Analysis (DMA) measurements have been performed in the turbulent

methane flame at the same locations of the optical measurements, using a TSI 3936, that allows

us to obtain particle size distributions in a range 3 – 65 nm. Figure 3.42 shows the experimental

configuration used for the DMA measurements. We used a 0.8 mm ID and 1.5 mm OD probe

vertically positioned into the flame. Gases are sampled for effect the low pressure generated by

the air flow through a calibrated throat. Therefore, by changing the air flow we were able to

obtain different dilution ratios (air flow/sampling flow). In this work the measurements have

been carried out using two value of dilution ratio: 1000 and 3500 in order to avoid coagulation

effects.

Optical results are confirmed by the size distribution functions measured by SMPS analysis in

the turbulent flame. Figure 3.43 reports the size distribution functions measured on the flame

axis at 10 cm.

At 10 cm above the burner on the flame axis, particle diameters range from 3 nm, the limit of the

detection system, up to 40 nm. The number concentration of particles with sizes below 10 nm is

more than one order of magnitude larger than that of particles with sizes larger than 20 nm confirming the very low concentration of soot in the analyzed flame.
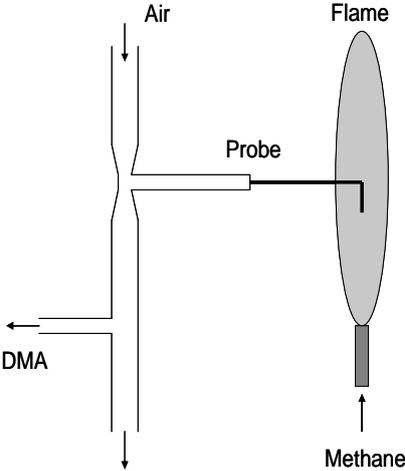
Fig. 3.42 Experimental set-up for DMA measurements.
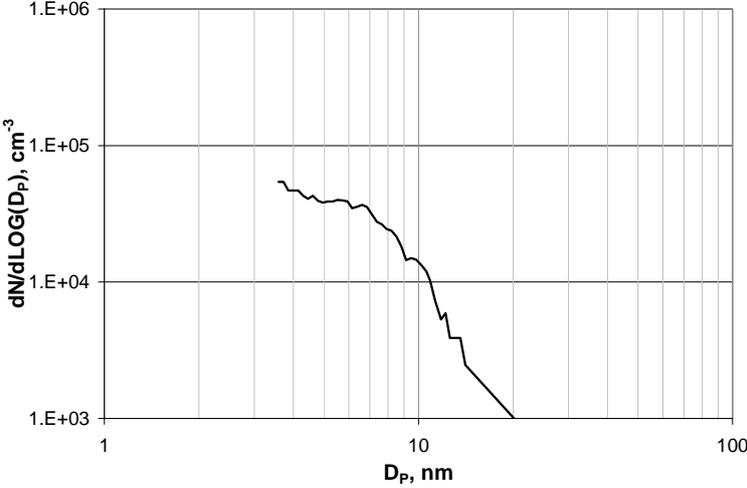
Fig. 3.43 Size distribution function of the particles detected at 10 cm along the flame axis of the turbulent methane flame.

CHAPTER 6

BURNERS FOR HOME APPLIACES

As consequence of the numerous experimental data obtained in laboratory burners configurations burning methane, an experimental study of the combustion characteristics of new natural gas burners used for home and water heating appliances has been performed during the thesis with the aim of evaluating the effect of burner configurations and operating conditions on the emissions of gaseous pollutants and organic carbon nanoparticles. The previously described in-situ optical diagnostics, based on laser induced emission spectroscopy (LIE), and ex-situ measurements, based on scanning mobility particle sizer (SMPS), and particles collection by water-based sampling technique, are used in order to evaluate the total particulate concentration and size distribution functions. Three different burners configurations: two premixed and one diffusive are studied under various operative conditions. Measurements have shown that particulate matter with size in the 1 nm to 10 nm size range is formed in all the examined conditions. The emitted mass concentration of these compounds is very low, of the order of 0.001 ppm. They are formed in large number concentrations in the flame region but are also strongly oxidized in the post-oxidation region of the devices. Soot particles with size larger than 10 nm are not formed in all the examined conditions.

6.1 BURNERS CONFIGURATION

The home heating burners consist in two premixed differentiated by the knitted metal fibre and the drilled cylindrical heads and one diffusive constituted by a five-tube injector of gaseous hydrocarbons (Toniato et al. [81]).

The burners have been operated in free atmosphere and in commercial devices.

6.2 EXPERIMENTAL PROCEDURE AND RESULT

Laser induced emission spectra and temperature have been measured vertically for different heights above the burner surface to follow the flame evolution, point A of the experimental lay out reported in figure 6.1. The flame emission signals of OH at 305 nm has been detected to measure the OH concentration along the flame axis.
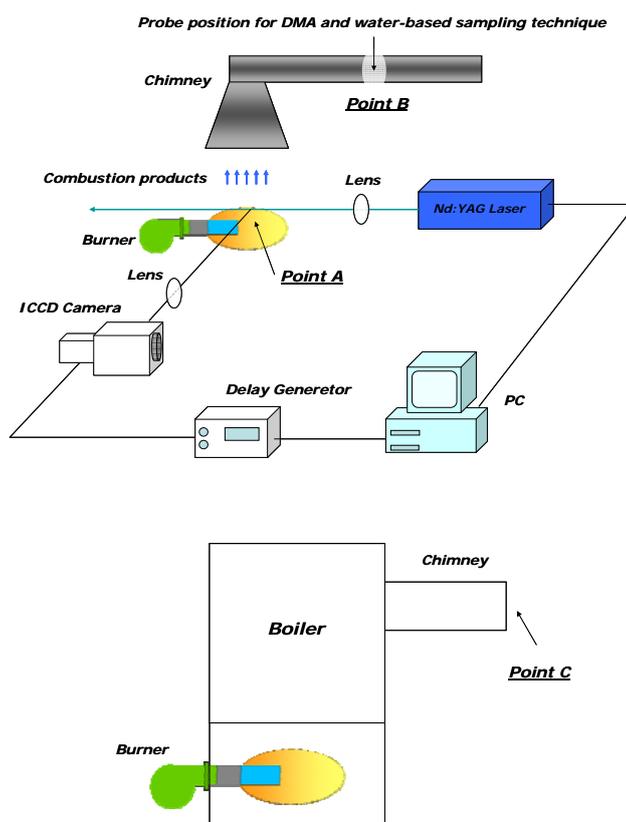
Fig. 6.1   Experimental configurations.

A water-based sampling technique has been used to collect fine organic aerosol emitted at the exhaust of the home heating burners operated in free atmosphere, point B in figure 6.1, and in commercial boilers, point C in figure 6.1.

Combustion products, sampled by a probe in the exhaust pipe, are cooled in order to condense combustion water and drawn through a reservoir containing deionised water, placed in an ice bath. This type of sampling procedure allows the collection of very small organic carbon aerosol

which have more affinity with water respect to soot (Sgrò et al. 2001). Water samples, put in a standard 1 cm path-length quartz cell, have been analyzed by light absorption and UV-induced fluorescence measurements. The light absorption spectra were recorded using a deuterium lamp in the 200-500 nm wavelength region. The fluorescence spectra were preformed in this case by using the forth harmonic (λ=266 nm) of a Nd:YAG pulsed laser with a pulse duration of 7 ns.

The size distribution functions of the particles in the exhaust pipe have been determined by SMPS technique.

On-line standard measurements have been also performed on the exhaust gases for the determination of the concentrations of, unburned hydrocarbons and NOx. CO_2 measurements have been used for the determination of exhaust gas dilution in the exhaust pipe.

6.3.1 IN-SITU MEASUREMENTS

Temperature, OH emission and Laser Induced Emission measurements have been performed along the axis of the two premixed flame burners at two loads, namely 8 kW and 16 kW, changing the excess air fed to the burner from the stoichiometric conditions (0 % excess air) to 31 % excess air. Figure 6.2 reports the OH and OC nanoparticles concentration profiles measured along the axis of the knitted metal fibre burner fuelled with methane at 16 kW and 0% excess air. OH emission (in arbitrary units in the graph) reaches a maximum close to the burner exit and decreases to the equilibrium value in 10 mm from the burner surface. Maximum OH concentration is well correlated with the maximum temperature measured in the flame and is representative of the main oxidation region of the flame.

Close to the burner exit, a 8 fluorescence signal (LIF) has also been measured and reported in fig.6.2 in terms of volume fraction of OC by the use of the previously described calibration procedure. It is initially very low and sharply increases reaching a maximum value at 20 mm, i.e. just downstream of the flame front.

After the maximum value of the order of 0.1 ppm reached downstream of the flame front, the volume fraction of the OC decreases to lower values of the order of 0.07 ppm. The laser induced incandescence (LII) signal in this flame condition is below the detection limit denoting the absence of soot particles.
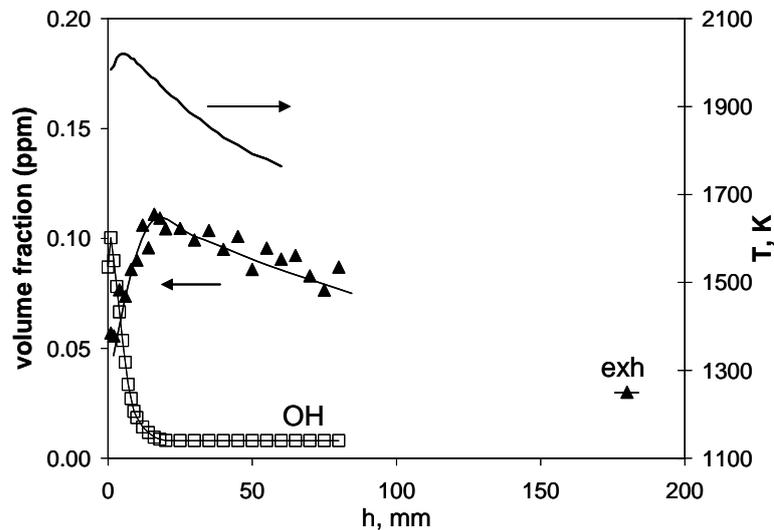
Fig. 6.2 Temperature, OH emission (□) and NOC volume fraction (▲) measured at different height from the burner surface (metal burner in premixed conditions at 16kW and 0% excess air). Also reported is the concentration of particulate in the exhaust pipe (ext).

6.3.2   EX-SITU MEASUREMENTS: WATER TRAP AND SMPS

Measurements of NOC have been performed in the exhaust pipe, point B in the fig. 6.1, by collecting the NOC in the condensed combustion water. The light absorption spectrum of the sample in water suspensions presents a strong absorption bands centred at about 210 nm superimposed to a continuous background. The first absorption band is typical of nitrogen-containing compounds, such as nitric acid, deriving from NOx interaction with water. The continuous background of absorption is very similar to the light absorption spectrum of NOC measured in rich flames (Sgro et al. [30]). A concentration of these species in water sample has been estimated; values of the order of 0.03 ppm have been found for the flame conditions reported in Fig. 6.2 taking into account the collection efficiency of the water-based sampling

104

techniques (estimated to be about 10%), (Sgro et al. [82]), and the dilution of the combustion gases in the exhaust pipe. The measured value is about one order of magnitude lower than that measured in situ at 80 mm above the burner by optical technique indicating a continuous oxidation of these species in the post flame region.

6.3.3 EMISSION INDEX FOR CONFIGURATION IN COMMERCIAL BOILER

Measurements have been performed also at the exhausts of commercial condensing boilers equipped with the two premixed combustion burners which have been tested on the laboratory rig. In the condensing applications, characterized from a high thermal efficiency, the combustion water is directly condensed into the boiler. Measurements have been performed, in this case, sampling and analysing the water condensed into the boiler, point C1 in the Fig. 6.3, and bubbling in a reservoir containing water the exhaust of the commercial condensing boiler, point C2 in the Fig. 6.3.

Hot combustion products → Condensing Boiler → Cold exhaust *Point C2*

↓ Combustion water *Point C1*
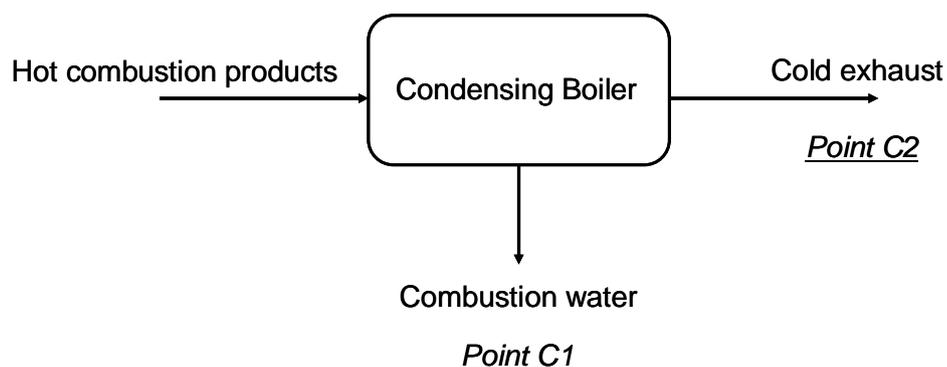
Fig. 6.3   Condensing boiler measurements lay out.

Figure 6.4 shows the emission indexes (mg/Nm3) for NOx, CO at 9 kW, 16 kW and 33 kW. The measurements have been performed with a fixed excess air of 31%. The emission data of NOx and CO from the two burners are quite similar. NOx emission remains also practically unchanged for the three loads. As expected, CO emission increases for increasing load.
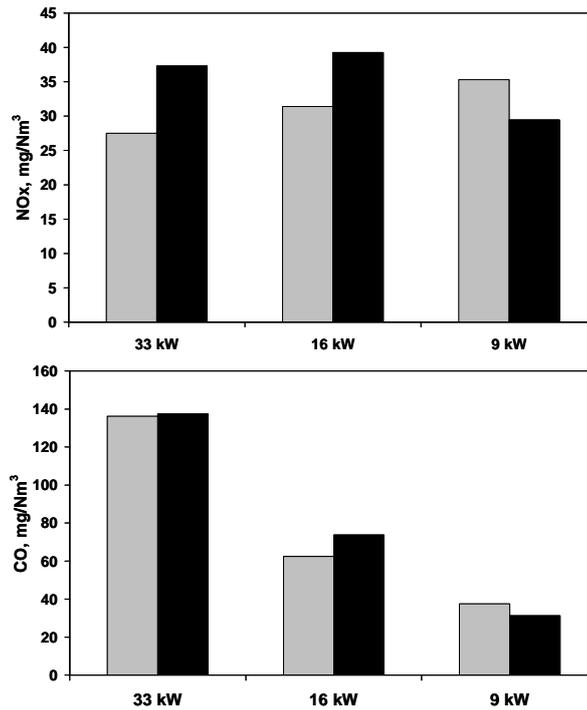
Fig. 6.4 Emission indexes (mg/Nm^3) for NOx and CO at 9 kW, 16 kW and 33 kW at the exhausts of commercial boilers, all measurements performed with a fixed excess air of 31% (light grey drilled premix, heavy grey metal premix).

The emission of organic carbon, reported in Fig. 6.5, is also quite constant for the three loads and burner types and very low, of the order of 0.1 mg/Nm3 that is in good agreement with other investigation (Cass et al. [83, 84, 85]). In the fig. 6.5 is also reported the organic carbon captured from the condensed combustion water of the boiler that, therefore, act as a organic carbon trap.

The comparison of commercial boilers exhausts with the measurements performed at the exhaust of the burners in the laboratory rig shows that organic carbon is continuously oxidized in the post-oxidation region of the boiler and is therefore reduced of one order of magnitude. Moreover a part of the organic carbon is also captured from the combustion water if condensed into the boiler. The effect of condensed combustion water on the reduction of the emission of OC is more evident comparing the emission indexes of the condensing boilers with those of standards commercial boilers using the same burners.
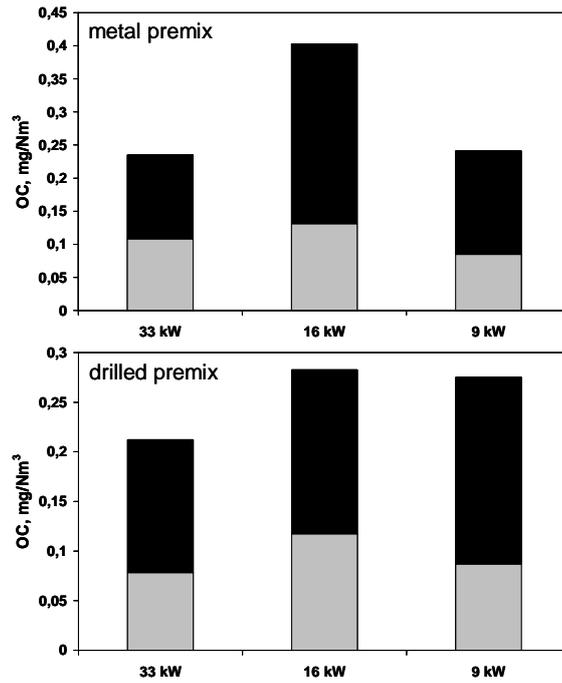
Fig. 6.5 Emission indexes (mg/Nm^3) of organic carbon at 9 kW, 16 kW and 33 kW at the exhausts of commercial boilers, all measurements performed with a fixed excess air of 31% (light grey emission in atmosphere, heavy grey captured in combustion water).

Figure 6.6 shows that in condensing boilers OC emissions are of the order of 0.1 mg/NM3, while, in standard boilers they are of the order of 0.2 mg/NM3.
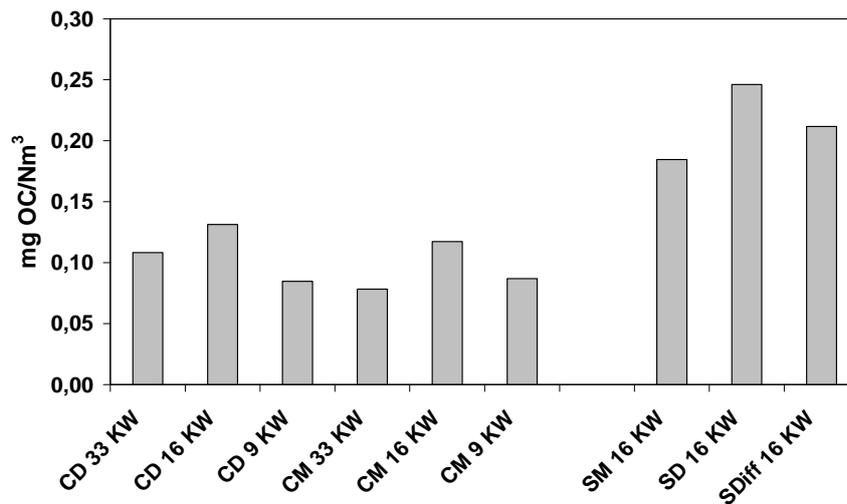
Fig. 6.6 Emission indexes (mg/Nm^3) of organic carbon for several burners configuration: CD and CM are drilled and metal premix burners in condensing boilers; SM, SD and SDiff are metal premix, drilled premix and diffusive burners in standard boilers.

107

CONCLUSIONS

A new optical diagnostic technique based on the use of an ultraviolet lasers source, the fifth harmonic of a Nd:YAG laser, has been developed. The selected high energy enhances fluorescence from aromatic species within the flame and also allows soot particles to heat up and emit incandescent radiation. Coupled scattering measurements allow the evaluation of the mean size of the particles.

Laser-induced fluorescence and laser-induced incandescence have been characterized in terms of laser power, acquisition time and wavelengths range of the spectral emission optimization.

Preliminary results on laminar premixed ethylene flames showed the possibility to use this technique for qualitative and quantitative simultaneous characterization of Nanoparticle of Organic Carbon (NOC) and soot particles as well as using extinction/scattering measurements.

Measurements showed that both LIF and LII signals linearly correlate with NOC and soot extinctions, respectively. These correlations allow us to calibrate both signals in order to obtain absolute quantitative information of the two particles classis.

The potentiality of laser induced emission spectroscopy respect to extinction/scattering measurements is more evident in real combustion systems because they normally operate in diffusion conditions. Therefore, LIF and LII measurements have been performed, with high spatial resolution, in laboratory laminar and turbulent diffusion flames burning methane and ethylene.

The experimental evidences allow us to conclude that two classes of nanoparticles are formed in flame: Nanoparticles of Organic Carbon (NOC) with sizes smaller than three nanometers and "primary" soot particles with sizes larger than ten nanometers that lead to the formation of soot aggregates.

NOC are formed in laminar premixed conditions as well as in laminar and turbulent diffusion flames.

In diffusion flames soot formation is located in a narrow annular region closer to the maximum temperature zone, and its maximum volume fraction is measured just after the decrease of organic carbon particle volume fraction. The radial position of the maximum soot volume fraction shifts, at increasing heights, towards the centreline. NOC are preferentially formed in the lower part of the flame and closer to the flame axis. The maximum volume fraction of organic carbon particles decreases at increasing heights in the flame shifting toward the centreline. It becomes negligible at the flame tip.

By comparison of methane and ethylene combustion in all examined conditions was possible to conclude that:

- As expected methane combustion produce a lower amount of particulate, NOC and soot particles, respect to ethylene.

- However, the reduction of soot was stronger than that of NOC particles. The ratio of NOC on soot in terms of volume fractions has been observed always to be higher in the methane combustion than that in the ethylene.

- Moreover, measurements indicate that while in the ethylene flame NOC are transformed to soot particles, in the methane flame, although formed in lower amounts, their concentration

value remains unchanged along the flame axis and hence they might be emitted from the flame.

The main results of this study of benzene combustion can be so resumed:

- high molecular mass structures with typical sizes of 3-4 nm are formed in the main oxidation region of the flame.

- the higher concentration of nanoparticles in the slightly-sooting flame and the radical-rich flame environment in which they are formed promote the dehydrogenation of nanoparticles increasing the level of their aromaticity. As a result, nanoparticles with typical sizes of about 5 nm, absorbing and fluorescing in the visible are formed in the slightly sooting flame.

- visible absorbing nanoparticles reach a maximum concentration just before the appearance of mature soot particles and they can be considered responsible for soot formation.

- inception of soot particles in benzene flames consists in the progressive aromatization of initially "transparent" structures, followed by coagulation of visible absorbing nanoparticles to form soot. This picture is different to that found in aliphatic fuel flames where the aromatization process which precedes coagulation has never been observed.

REFERENCES

1. H. Richter, J.B. Howard. *Formation of polycyclic aromatic hydrocarbons and their growth to soot-a review of chemical reaction pathways*. Prog Energy and Comb. Sci., 26:565-608, (2000).

2. Homann KH, Wagner HG. *Some new aspects of the mechanism of carbon formation in premixed flames*. Eleventh Symposium (International) on Combustion, The Combustion Institute, Pittsburgh. p. 371–9, (1967).

3. Crittenden BD, Long R. *Formation of polycyclic aromatics in rich premixed acetylene and ethylene flames*. Combust Flame;20:359–68, (1973).

4. H. Bockhorn, F. Fetting, HW. Wenz. *Investigation of the formation of high molecular hydrocarbons and soot in premixed hydrocarbon–oxygen flames*. Phys Chem, 87:1067–73, (1983).

5. Frenklach M, Warnatz J. *Detailed modeling of PAH profiles in a sooting low-pressure acetylene flame*. Combust Sci Technol;51:265–83, (1987).

6. Colket MB. *The pyrolysis of acetylene and vinylacetylene in a single-pulse shock tube*. Twenty-first Symposium (International) on Combustion, The Combustion Institute, Pittsburgh. p. 851–64, (1986).

7. Westmoreland PR, Dean AM, Howard JB, Longwell JP. *Forming benzene in flames by chemically activated isomerization*. J Phys Chem;93:8171–80, (1989).

8. Bastin E, Delfau J-L, Reuillon M, Vovelle C, Warnatz J. *Experimental and computational investigation of the structure of a sooting C2H2–O2–Ar flame*. Twenty-second Symposium (International) on Combustion, The Combustion Institute, Pittsburgh. p. 313–22, (1988).

9. Miller JA, Melius CF. *Kinetic and thermodynamic issues in the formation of aromatic compounds in flames of aliphatic fuels*. Combust Flame;91:21–39, (1992).

10. Stein SE, Walker JA, Suryan MM, Fahr A. *A new pathway to benzene in flames*. Twenty-third Symposium (International) on Combustion, The Combustion Institute, Pittsburgh, p. 85–90, (1990).

11. Dean AM. *Detailed kinetic modeling of autocatalysis in methane pyrolysis*. J Phys Chem; 94:1432–9, (1990).

12. Marinov NM, Pitz WJ, Westbrook CK, Castaldi MJ, Senkan SM. *Modeling of aromatic and polycyclic aromatic hydrocarbon formation in premixed methane and ethane flames*. Combust Sci Technol;116/117:211, (1996).

13. Castaldi MJ, Marinov NM, Melius CF, Huang J, Senkan SM, Pitz WJ, Westbrook CK. *Experimental and modeling investigation of aromatic and polycyclic aromatic hydrocarbon formation in a premixed ethylene flame*. Twenty-sixth Symposium (International) on Combustion, The Combustion Institute, Pittsburgh. p. 693–702, (1996).

14. Jensen DE. *Prediction of soot formation rates: a new approach*. Proc Roy Soc London A;338:375–396, (1974).

15. Frenklach, M., Clary, D.W., Gardiner, W.C., Stein, S.E., *Detailed kinetic modeling of soot formation in shock-tube pyrolysis of acetylene*. Twentieth Symposium (International) on Combustion, The Combustion Institute, Pittsburgh,. p. 887–901 (1984).

16. Wang H, Frenklach M. *Calculations of rate coefficients for the chemically activated reactions of acetylene with vinylic and aromatic radicals*. J Phys Chem;98:11465–89, (1994).

17. D'Anna A, Violi A. *A kinetic model for the formation of aromatic hydrocarbons in premixed laminar flames*. Twenty Seventh Symposium (International) on Combustion, The Combustion Institute, Pittsburgh, p. 425–33, (1998).

18. B.L. Wersborg, J.B. Howard, G.C. Williams, *Physical Mechanism in Carbon Formation in Flames*. Fourteenth Symposium (International) on Combustion, The Combustion Institute, Pittsburgh, p. 929, (1972).

19. Bittner JD, Howard JB. *Composition profiles and reaction mechanisms in a near-sooting premixed benzene/oxygen/argon flame*. Eighteenth Symposium (International) on Combustion, The Combustion Institute, Pittsburgh, p.1105–16, (1981).

20. D'Alessio A, D'Anna A, D'Orsi A, Minutolo P, Barbella R, Ciajolo A. *Precursor formation and soot inception in premixed ethylene flames*. Twenty Fourth Symposium (International) on Combustion, The Combustion Institute, Pittsburgh, p.973-80, (1992).

21. Minutolo P, Gambi G, D'Alessio A, D'Anna A, *Optical and spectroscopic characterization of rich premixed flames across the soot formation threshold*. Combustion Science and Technology 101(1-6), p.311-25, (1994).

22. D'Alessio A, Gambi G, Minutolo P, Russo S, D'Anna A, *Optical characterization of rich premixed CH4/O2 flames across the soot formation threshold*. Twenty Fifth Symposium (International) on Combustion, The Combustion Institute, Pittsburgh, p.645-651, (1994).

23. Thierley M, Grotheer H-H, Aigner M, Yang Z, Abid A, Zhao B, Wang H, *On existence of nanoparticles below the sooting threshold*. Thirty First Symposium (International) on Combustion, The Combustion Institute, Pittsburgh, p.639-647, (2007).

24. D'Alessio A, Barone A, Cau R, D'Anna A, Minutolo P, *Surface deposition and coagulation efficiency of combustion generated nanoparticles in the size range from 1 to 10 nm*. Thirty Symposium (International) on Combustion, The Combustion Institute, Pittsburgh, (Pt. 2), p.2595-2603, (2005).

25. D'Anna A, D'Alessio A, Minutolo P, *Spectroscopic and Chemical Characterization of Soot Inception Processes in Premixed Laminar Flames at Atmospheric Pressure*, in: H. Bockhorn (Ed.), Springer Series in Chemical Physics, vol. 59, p. 83–101 (1994).

26. D'Alessio A, D'Anna A, Gambi G, Minutolo P, *The spectroscopic characterization of UV absorbing nanoparticles in fuel rich soot forming flames*. Journal of Aerosol Science, 29(4), p.397-409, (1998).

27. Minutolo P, Gambi G, D'Alessio A, *Properties of carbonaceous nanoparticles in flat premixed C2H4/air flames with C/O ranging from 0.4 to soot appearance limit*. Twenty Seventh Symposium (International) on Combustion, The Combustion Institute, Pittsburgh, p. 1461–1469, (1998).

28. Dobbins RA and Subramaniasivam H, *Soot Precursor Particles in Flames*, in: H. Bockhorn (Ed.), Springer Series in Chemical Physics, vol. 59, p. 291–299, (1994).

29. Vander Wal RL, *Soot Precursor Material: Visualization via Simultaneous LIF-LII and Characterization via TEM*. Twenty-sixth Symposium (International) on Combustion, The Combustion Institute, Pittsburgh. p. 2269–2275, (1996).

30. Sgro LA, Basile G, Barone AC, D'Anna A, Minutolo P, Borghese A, D'Alessio A, *Detection of combustion formed nanoparticles*, Chemosphere 51 (10), p.1079-1090, (2003).

31. Zhao B, Yang Z, Johnston MV, Wang H, Wexler AS, Balthasar M, Craft M, *Measurement and numerical simulation of soot particle size distribution functions in a laminar premixed ethylene-oxygen-argon flame*. Combustion and Flame 133, 173-188, (2003).

32. Sgro LA, De Filippo A, Lanzuolo G, D'Alessio A, *Characterization of nanoparticles of organic carbon (NOC) produced in rich premixed flames by differential mobility analysis*, Thirty First Symposium (International) on Combustion, The Combustion Institute, Pittsburgh, p. 631-638, (2007).

33. Barone AC, D'Alessio A, D'Anna A, *Morphological characterization of the early process of soot formation by atomic force microscopy*. Combustion and Flame, 132(1/2), p.181-187 (2003).

34. Frenklach M, Wang H. *Detailed modeling of soot particle nucleation and growth*. Twenty-third Symposium (International) on Combustion, The Combustion Institute, Pittsburgh, (1990).

35. D'Anna A, Kent JH, *Modelling of particulate carbon and species formations in co-flow diffusion flames of ethylene*. Combust. Flame 144, 249-260, (2006).

36. Sardar SB, Fine PM, Sioutas C, *Seasonal and spatial variability of the size-resolved chemical composition of particulate matter (PM10) in the Los Angeles Basin*. Journal of Geophysical Research, 10, D07S08 (2005).

37. Kennedy IM, *The health effects of combustion-generated aerosols*. Thirty-one Symposium (International) on Combustion, The Combustion Institute, Pittsburgh, p.2757-2770, (2007).

38. Donaldson K, Tran L, Jimenez LA, Duffin R, Newby RE, Mills N, MacNee W, Stone V, *Combustion-derived nanoparticles: A review of their toxicology following inhalation exposure*. Particle and Fibre Toxicology, 2:10, (2005).

39. Oberdoster G, Oberdoster E, Oberdoster J, *Nanotoxicology: an emerging discipline evolving from studies of ultrafine particles*. Environmental. Health Perspectives, 113, p. 823-839, (2005).

40. Jacobson MZ, *Strong radiative heating due to the mixing state of black carbon in atmospheric aerosols*. Nature, 409, p. 695–697 (2001).

41. Novakov T, Penner JE, *Large contribution of organic aerosols to cloud-condensation-nuclei concentrations*. Nature, 365, p. 823-826 (1993).

42. D'Anna A, Rolando A, Allouis C, Minutolo P, D'Alessio A, *Nano-organic carbon and soot particle measurements in a laminar ethylene diffusion flame*. Thirty Symposium (International) on Combustion, The Combustion Institute, Pittsburgh, (Pt. 1), p.1449-1456, (2005).

43. Charalampopoulos TT, *Morphology and Dynamics of Agglomerated Particulates in Combustion Systems Using Light Scattering Techniques*, Prog. Energy Combust. Sci., 18, p. 13 – 45, (1992).

44. Mahallawy FEL, El-Din Habik S, *Fundamentals and technology of Combustion*, Elsevier ed. (2002).

45. Kent JH, Wagner HG, *A reversed coflowing laminar diffusion flame*. Zeitschrift fuer Physikalische Chemie (Muenchen, Germany) 139, p.59-68 (1984).

46. Santoro RJ, Santoro HG, Semerjian RA, Dobbins RA, *Soot particle measurements in diffusion flames*. Combustion and Flame 51: 203–218 (1983).

47. Shaddix CR, Smyth KC, *LII measurements of soot production in steady and flickering Methane, Propane and Ethylene Diffusion Flames*. Combustion and Flame 107: 418–452 (1996).

48. McEnally CS, Koylu UO, Pfefferle LD, Rosner DE, *Soot Volume fraction and Temperature Measurements in Laminar Nonpremixed Flames Using Thermocouples*. Combustion and Flame 109: 701-720, (1997).

49. Hilbert R, Tap F, El-Rabii H, The´venin D, *Impact of detailed chemistry and transport models on turbulent combustion simulations*. Progress in Energy and Combustion Science 30, p.61–117, (2004).

50. Schulz C, Kock BF, Hofmann M, Michelsen, Will S, Bougie B, Suntz R, Smallwood G, *Laser-induced incandescence: Recent trend and current questions*. Appl. Phys. B 83 (3), p. 333-354 (2006).

51. Santoro RJ, Shaddix CR, *Laser-Induced Incandescence*, in Applied Combustion Diagnostics, Taylor & Francis, p. 252 – 286, (2002).

52. Eckbreth ACJ, *Effects of laser-modulated particulate incandescence on Raman scattering diagnostics*, Journal of Applied Physics 48, p. 4473-9, (1977).

53. Melton LA, *Soot diagnostics based on laser heating*, Chemical and Physical Processes in Combustion Paper 23, 4 pp.(1983).

54. Zizak G, *Laser Induced Incandescence (LII) of soot*, Lecture given at the ICS Training Course on Laser Diagnostics of Combustion Processes, NILES, University of Cairo, Egypt, 18-22 Nov. (2000).

55. Dalzell WH, Sarofim AF, *Optical constants of soot and their application to heat flux calculations*, J. Heat Transfer, 91, p. 100-104, (1969).

56. Bengtsson PE, Alden M, *Soot-visualization strategies using laser techniques*, Appl. Phys. B 60, p. 51- 59, (1995).

57. Vander Wal RL, Jensen KA, Choi MY, *Simultaneous Laser-Induced Emission of Soot and Polycyclic Aromatic Hydrocarbons Within a Gas-Jet Diffusion Flame*, Combustion and Flame 109: p. 399 – 414, (1997).

58. Vander Wal RL, *Laser-induced incandescence: detection issues*, Appl. Opt. 35, 6548, (1996).

59. Dasch CJ, *Continuos-Wave Probe Laser Investigation of Laser Vaporization of Small Soot Particles in a Flame*, Appl. Optics, 23, p. 2209 – 2215, (1984).

60. Michelsen HA, Witze PO, Kayes D, Hochgrb S, *Time-resolved laser-induced incandescence of soot: the influence of experimental factors ans microphysical mechanisms*, Applied Optics, 42, p. 5577 – 5590, (2003).

61. Ni T, Pinson JA, Gupta S, Santoro RJ, *Two-Dimensional Imaging of Soot Volume fraction by the Use of Laser-Induced Incandescence*, Applied Optics, 34, p. 7083 – 7091, (1995).

62. Brockhinke A, Linne MA, *Short-Pulse Techniques: Picosecond Fluorescence, Energy Transfer, and "Quench-Free" Measurements,* in Applied Combustion Diagnostics, Taylor & Francis, p. 128 – 154, (2002).

63. Smyth KC, Crosley D, *Detection of Minor Species with Laser Techniques, in Applied Combustion Diagnostics*, Taylor & Francis, p. 9 – 32, (2002).

64. Ciajolo A, Tregrossi A, Barbella R, Ragucci R, Apicella B, De Joannon M, *The Relation Between Ultraviolet-Excited Fluorescence Spectroscopy and Aromatic Species Formed in Rich Laminar Ethylene Flames*. COMBUSTION AND FLAME 125: p. 1225–1229 (2001).

65. Ciajolo A, Ragucci R, Apicella B, Barbella R, De Joannon M, Tregrossi A, *Fluorescence spectroscopy of aromatic species produced in rich premixed ethylene Flames*. Chemosphere 42, p. 835-841, (2001).

66. Bruno A, de Lisio C, Minutolo P, D'Alessio A. *Evidence of fluorescent carbon nanoparticles produced in premixed flames by time-resolved fluorescence polarization anisotropy.* Combustion and Flame 151(3), 472-481 (2007).

67. Dasch, CJ, *One-Dimensional Tomography: A Comparison of Abel, Onion-Peeling, and Filtered Backprojection Methods*, Appl. Optics, 31, p. 1146 – 1152, (1992).

68. Walsh KT, Fielding J, Long MB, *Effect of light-collection geometry on reconstruction errors in Abel inversions*, Optics Letters, 25, 457 – 459, (2000).

69. D'Alessio A, *Laser light scattering and fluorescence diagnostics of rich flames produced by gaseous and liquid fuels, in Particulate carbon: formation during combustion*, Siegla DC and Smith GW (Ed.), Plenum Press, New York, p. 207 – 259, (1981).

70. Operation and Service Manual, Model 3936 Scanning Mobility Particle Sizer™ (SMPSTM) Spectrometer, TSI Incorporated 500 Cardigan Road, Shoreview, MN 55126 U.S.A., http://www.tsi.com.

71. Rolando A, D'Alessio A, D'Anna A, Allouis C, Beretta F, Minutolo P, *Measurement of particulate volume fraction in a coflow diffusion flame using transient thermocouple technique*. Combustion Science and Technology, 176(5-6), p. 945 – 958, (2004).

72. Kent JH, Wagner HG, *Why do diffusion flames emit smoke?*, Combustion Science and Technology, 41(5-6), p. 245-69, (1984).

73. Eisner AD, Rosner DE, *Experimental studies of soot particle thermophoresis in nonisothermal combustion gases using thermocouple response technique*. Combust. Flame 61, p. 153 – 166, (1985).

74. Borghese A, Merola SS, *Time-resolved spectral and spatial description of laser-induced breakdown in air as a pulsed, bright, and broadband ultraviolet-visible light source*. Applied Optics, 37(18), p. 3977-3983, (1998).

75. Cecere D, Sgro LA, Basile G, D'Alessio A, D'Anna A, Minutolo P, *Evidence and characterization of nanoparticles produced in nonsooting premixed flames*. Combustion Science and Technology, 174 (11-12), p. 377-398, (2002).

76. D'Anna A, Sirignano M, Commodo M, Pagliara R, Minutolo P, *An experimental and modelling study of particulate formation in premixed flames burning methane*. Proceeding of the Fifth Mediterranean Combustion Symposium, Monastir, Tunisia, September 9-13, (2007).

77. Basile G, Rolando A, D'Alessio A, D'Anna A, Minutolo P, *Coagulation and carbonization processes in slightly sooting premixed flames*. Proceedings of the Combustion Institute, 29(Pt. 2), p. 2391-2397, (2002).

78. Minutolo P, Gambi G, D'Alessio A, *The optical band gap model in the interpretation of the UV-visible absorption spectra of rich premixed flames*. Symposium (International) on Combustion, [Proceedings] (1996), 26th(Vol. 1), 951-957.

79. Smooke MD, McEnally CS, Pfefferle LD, Colket RJH, *Computational and Experimental Study of Soot Formation in a Coflow, Laminar Diffusion Flame*, Combustion and Flame 117: p. 117–139 (1999).

80. Kent JH, Honnery D, *Soot and mixture fraction in turbulent diffusion flames*. Combust. Sci. Technol. 54, p. 383-397, (1987).

81. Toniato G, Zambon A, Lovato A, Tomasetto M, Mazzacavallo G, *Metallic mat gas*. In: Proceedings of the 29th Meeting of the Italian Section of the Combustion Institute, 14-17 June 2006, Pisa, Italy, paper I-3.

82. Sgro LA, Minutolo P, Basile G, D'Alessio A, *UV-visible spectroscopy of organic carbon particulate sampled from ethylene/air flames*. Chemosphere, 42 (5-7), 671-680, (2001).

83. Hildemann LM, Markowski GR, Cass GR. *Chemical Composition of Emissions from Urban Sources of Fine Organic Aerosol*. Environ Sci Technol 25: p. 744-759, (1991).

84. Hildemann LM, Mazurek MA, Cass GR. *Quantitative Characterization of Urban Souces of Organic Aerosol by High-Resolution Gas Chromatography*. Environ Sci Technol 25: p. 1311-1325 (1991).

85. Rogge WF, Hildemann LM, Mazurek MA, Cass GR. *Sources of Fine Organic Aerosol. 5. Natural Gas Home Appliances*. Environ Sci Technol 27: p. 2736-2744, (1993).

APPENDICIES

PUBBLICATIONS

1) M. Commodo, S. Violi, A. D'Anna, A. D'Alessio, C. Allouis, F. Beretta, P. Minutolo, "*Soot and nanoparticle formation in laminar and turbulent flames*". Combustion Science and Technology, 179(1-2): 387-400 (2007).

2) A. D'Anna, M. Commodo, S. Violi, C. Allouis, J. Kent, "*Nano organic carbon and soot in turbulent non-premixed ethylene flames*". Proceedings of the Combustion Institute 31, 621-629 (2007).

3) P. Minutolo, A. D'Anna, M. Commodo, R. Pagliara, G. Toniato, C. Accordini, "*Emission of Fine Particles from Natural Gas Domestic Burners*", Accepted for publicationon on Environmental Engineering Science.

4) A. D'Anna, M. Sirignano, M. Commodo, R. Pagliara, P. Minutolo, "*An Experimental and Modelling Study of Particulate Formation in Flames burning Methane*", Accepted for publicationon on Combustion Science and Technology.

5) A. D'Anna, M. Commodo, P. Minutolo, "*Particle Inception in Laminar Premixed Benzene Flames*", Accepted for publication on Combustion Science and Technology.

CONFERENCE PRESENTATION

6) M. Commodo, S. Violi, A. D'Alessio, A. D'Anna, C. Allouis, F. Beretta, P. Minutolo, "*Soot and nanoparticle concentrations in a turbulent non-premixed ethylene/air flame from laser induced emission measurements at 213nm*", 28th Meeting of Italian section of the Combustion Institute, Naples, July (2005).

7) M. Commodo, S. Violi, A. D'Anna, A. D'Alessio, C. Allouis, F. Beretta and P. Minutolo, "*Soot and Nanoparticle formation in Laminar and Turbulent Flames*", 4th Mediterranean Combustion Symposium, Lisbon, October 6-10 (2005).

8) M. Commodo, C. Allouis, P. Minutolo, A. D'Anna, A. D'Alessio, "*U.V. Laser Induced Fluorescence for the detection of nanosized organic carbon (NOC) and soot particles in laminar premixed flames*", 2nd European Combustion Meeting, Louvain Belgium, (2005).

9) A. D'Alessio, A. D'Anna, P. Minutolo, L.A. Sgro, A. Barone, A. Bruno, M. Commodo, A. De Filippo, S. Violi, "*Experimental Techniques for the Detection of Nanoparticles and Soot in Flames, Engines exhausts and Urban Atmosphere*", AAA Symposium, November 12-15, Milan, Italy (2006).

10) P. Minutolo, M. Commodo, S. Violi, A. D'Anna, "*Particle Inception in Laminar Premixed Benzene Flames*", 29th Combustion Meeting, Italian Section of the Combustion Institute, Pisa (2006).

11) M. Commodo, S. Violi, A. D'Anna, P. Minutolo, "*Particulate Measurement in a Turbulent Jet Flame of Methane*", 29th Combustion Meeting, Italian Section of the Combustion Institute, Pisa (2006).

12) M. Commodo, S. Violi, A. D'Anna, C. Allouis, P. Minutolo, "*Experimental Study of Nanometric Organic Carbon and Soot in a Methane Coflow Laminar Diffusion Flame*", 29th Combustion Meeting, Italian Section of the Combustion Institute, Pisa (2006).

13) M. Commodo, E. Bichi, A. D'Anna, P. Minutolo, R. Pagliara, C. Allouis, "*Nanometric Organic Carbon and Soot in Methane Non-Premixed Flames*", Proceedings of third European Combustion Meeting ECM, Crete, Greece 11-13 April (2007).

14) A. De Filippo, M. Commodo, P. Minutolo, L.A. Sgro, "*The Evolution of Nanoparticle Size Distributions and UV-visible Extinction and Fluorescence in Premixed Ethylene Air Flames*", Proceedings of third European Combustion Meeting ECM, Crete, Greece 11-13 April (2007).

15) G. Toniato, C. Accordini, A. D'Anna, M. Commodo, P. Minutolo, R. Pagliara, "*Combustion characteristics of commercial burner for home appliance*", Proceedings of third European Combustion Meeting ECM, Crete, Greece 11-13 April (2007).

16) M. Commodo, E. Bichi, A. D'Anna, P. Minutolo, R. Pagliara, C. Allouis, "*Experimental study on nano-sized particles produced in flames burning methane*". 30th Combustion Meeting, Italian Section of the Combustion Institute, Ischia (2007).

17) A. D'Anna, M. Sirignano, M. Commodo, R. Pagliara, P. Minutolo, "*An Experimental and Modelling Study of Particulate Formation in Flames burning Methane*", Fifth International Mediterranean Combustion Symposium, Monastir, Tunisia, September 9-13 (2007).

18) A. D'Anna, M. Commodo, P. Minutolo, "*Particle Inception in Laminar Premixed Benzene Flames*", Fifth International Mediterranean Combustion Symposium, Monastir, Tunisia, September 9-13 (2007).